Thermodynamics of Carbon Dioxide-Hydrocarbon Systems

Yolanda Sanchez-Vicente[1], Weparn J Tay[1], Saif Z Al Ghafri[1,2], J P Martin Trusler[1*]

[1]Qatar Carbonates and Carbon Storage Research Centre, Department of Chemical Engineering, Imperial College London, South Kensington Campus, London SW7 2AZ, United Kingdom

[2]Centre for Energy, School of Mechanical & Chemical Engineering, The University of Western Australia, Crawley, WA 6009, Australia

* Corresponding Author. Email: m.trusler@imperial.ac.uk

ABSTRACT

Understanding the thermophysical properties for mixtures of CO_2 and hydrocarbons at reservoir conditions is very important for the correct design and optimization of CO_2-enhanced oil recovery and carbon storage in depleted oil or gas fields. In this paper, we present a comprehensive thermodynamic study of the prototype system (CO_2 + n-heptane) comprising highly-accurate measurements of the saturated-phase densities, compressed-fluid densities, and bubble and dew points at temperatures from 283 K to 473 K and pressures up to 68 MPa over the full range of composition. We use these results to examine the predictive capability of two leading thermodynamic models: the Predictive Peng-Robinson (PPR-78) equation of state and a version of the Statistical Associating Fluid Theory for potentials of the Mie form, known as SAFT-γ Mie. Both of these models use group contribution approaches to estimate interaction parameters and can be applied to complex multi-component systems. The comparison shows that both approaches are reliable for the phase behavior. Neither model is entirely satisfactory for density, with each exhibiting absolute average relative deviations (AARD) from the experimental data of about 4 % for the saturated-phase densities and 2 % for the compressed-fluid densities; however, SAFT-γ Mie is found to be much more accurate than PPR-78 for the compressibility, with an overall AARD of 6 % compared with 18 % for PPR-78.

Keywords: carbon dioxide; density; heptane; hydrocarbon; miscibility; phase behavior

1. Introduction

Largely as a consequence of the combustion of fossil fuels, carbon dioxide concentrations in the atmosphere have been rising steadily and have recently surpassed 400 ppm [1]. This rising trend is the major driver of a continuing process of climate change that has so far seen the global mean surface temperature increase by about 1°C since pre-industrial times [2, 3]. Clearly, there is now an urgent need to stabilise CO_2 levels in the atmosphere to mitigate further dangerous climate change. In December 2015, an action plan was agreed in Paris with the aim of limiting the global average temperature increase by 2100 to < 2 °C above pre-industrial levels [4]. To achieve this, a massive reduction in CO_2 emissions is required. The pathway to decarbonization will probably include a mix of technologies. As it is generally accepted that fossil fuels will continue to be part of the global energy mix during the 21st century, carbon capture and storage (CCS) will be a crucial technology in the drive to reduce anthropogenic CO_2 emissions from the power and industry sectors over the short and medium term, thereby protecting the security and stability of the energy system. According to an IEA report in 2015 [5], in all sectors, the amount of CO_2 captured and stored needs to be about 6 Gt per year by 2050 as a part of the overall strategy needed to achieve the 2 °C target. An advantage of CCS technologies is that they can be retrofitted to many industrial processes such as natural gas processing, hydrogen production, steel and cement making, as well as to power generation. Furthermore, if biomass firing is adopted power generation with net-negative CO_2 emissions is possible [6].

The CCS process comprises three main steps: capture (typically separation of CO_2 from other gaseous substances), transport (*e.g.* by pipeline), and finally storage in a geological formation (CO_2 injection and long-term monitoring to ensure permanence) [7]. Potential geological storage sites for CO_2 include active and depleted hydrocarbon reservoirs, un-minable coal seams and deep saline aquifers [8]. Potentially, the cheapest storage solution would be injection into partially-depleted oil reservoirs to enhance oil recovery (CO_2-EOR) while also storing large amounts of CO_2 [9]. CO_2-EOR could be beneficial economically as a means of

reducing the high cost of CCS. Moreover, the geological properties of the oil and gas reservoirs are usually better known, as a result of their previous exploitation history, than is the case for other storage sinks. The largest commercial CCS projects have been achieved by combining CCS with EOR technology [10]. The recently published white paper, “Can technology unlock unburnable carbon?” [11] estimates that, worldwide, 1,000 Gt of CO_2 can be stored in hydrocarbon reservoirs alone. The analysis in the white paper suggests that, in the period 2010 to 2050, between 100 Gt and 500 Gt of CO_2 storage would be required to meet the 2 ºC objective; therefore, the available oil and gas fields potentially have the capacity to store all of the targeted CO_2, possibly at a lower cost than other options.

In the CO_2-EOR process, some of the residual oil trapped in the reservoir after secondary recovery is extracted with a tertiary CO_2 flood. The performance of the CO_2 flood relies strongly on the physical properties of the mixture of CO_2 with crude oil. Depending upon the oil composition and the temperature and pressure in the reservoir, CO_2 flooding can be either miscible, where complete miscibility of oil and CO_2 is possible, or partially miscible. The miscibility of CO_2 with the crude oil is characterized by the minimum miscibility pressure (MMP) at the reservoir temperature. This MMP is often determined in the laboratory using bottom-hole oil samples with CO_2 in the slim-tube experiment [12]. However, in the field, 100 % sweep efficiency is not achieved, even above the MMP, as the CO_2 can pass along high-permeability paths between the injection and production wells, bypassing some of the residual oil. Therefore, under typical reservoir conditions, two non-aqueous phases will be present during CO_2 injection: one phase rich in CO_2, containing light hydrocarbons extracted from the oil, and the other rich in heavier hydrocarbons. The CO_2-rich phase will have a low viscosity and flow more freely towards the production well, contacting fresh oil from which it may extract further hydrocarbons. In addition, dissolution of CO_2 in the oil-rich phase results in swelling and a reduction in viscosity; this expanded oil can then also flow more easily towards the production wells [13]. At the surface, CO_2 dissolved in the produced oil is separated and re-circulated back into the process, while CO_2 not transported to the production wells is permanently stored

during the process. In some fields, 40% to 50% of the injected CO_2 remains in the reservoir permanently [14], and a significant portion of the residual oil is extracted [15]. For example, since 2008, the Wasson Field's Denver Unit CO_2 EOR project has recovered 15 % of the residual oil saturation after waterflooding [16]. Enhanced gas recovery with CO_2 injection and sequestration has also been proposed and , like CO_2-EOR, may offer an economically advantageous way of achieving carbon storage [17, 18].

Understanding of the phase behaviour and thermophysical properties for CO_2 + hydrocarbon systems at reservoir conditions is very important for the correct design and optimization of both CO_2-EOR and carbon storage processes. In addition to phase behaviour, the thermophysical properties of interest include (but are not limited to) the saturated-phase and compressed-fluid densities. These properties are essential to determine the amount of CO_2 that can be stored in a depleted oil reservoir as well as to model convective transport through the reservoir [19]. The saturated-phase and compressed-fluid densities are also necessary for calculating the oil swelling during CO_2 reservoir flooding. Moreover, such data are important in downstream processing and in a wide range of industrial applications such as supercritical extraction and separation processes [20, 21]. Since these processes cover large ranges of operating conditions and involve multicomponent systems, reservoir/process simulations are employed in design. The design of robust and safe processes can only be achieved if the equation-of-state (EOS) models used in these simulations are optimized and/or validated with accurate experimental data [22]. In oilfield applications, the parameters of the EoS models may be optimised against measured properties of bottom-hole reservoir-fluid samples taken from the production zones of interest. However, both the generic understanding of phase behaviour and properties, and the interpretation of field data, rely greatly upon a thorough understanding of simpler systems that present the essential features of the actual reservoir fluids. For CO_2-EOR and carbon storage applications, such systems comprise mixtures of CO_2 with one or more hydrocarbon components. In order to construct reliable EOS models, it is necessary to have a substantial database of experimental information pertaining to phase

behaviour and properties at reservoir conditions. Unfortunately, the available phase-behavior, saturated-phase and compressed-fluid density data for the mixtures of interest are extremely limited at reservoir conditions [23, 24].

In both petroleum and chemical engineering applications involving carbon dioxide and hydrocarbons, cubic equations of state (CEOS) are very widely deployed [25, 26]. These are modifications of the van der Waals EOS and include such well-known models as the Peng-Robinson (PR) [27] and Soave-Redlich-Kwong (SRK) [28] CEOS. In connection with these, experimental data (especially vapor-liquid equilibrium data) for binary mixtures are used in the optimization of binary interaction parameters. Therefore, the performance of traditional CEOS models is limited in part by the accuracy and extent of the experimental data used in these optimizations. Several previous studies have explored the application of CEOS to mixtures of CO_2 with hydrocarbons. For example, Kariznovi have measured the bubble-curves and saturated liquid densities of ternary mixtures containing CO_2, decane and either tetradecane of octadecane [29-32]. CEOS models investigated provided a good description of the bubble-curve data when the binary interaction parameters were regressed against the binary VLE data. However, they obtained a generally poor description of the saturated-liquid densities unless volume translation terms fitted to experimental mixture data were incorporated. Other studies show similar results [33, 34] and it can be concluded that, while conventional CEOS models can offer a good representation of phase behavior, they perform relatively poorly in the prediction of density and fail in the critical region. Volume translation can be used to improve the representation of liquid density in the sub-critical region somewhat, typically by making a temperature-dependent adjustment to the molar volume chosen to fit the saturated liquid density [35]. Additionally, the crossover approach may be applied to improve the representation of the critical region for both pure fluids and binary mixtures [36-38]. In the context of hydrocarbon-CO_2 mixtures, Shen et al. [39] have studied the performance of the SRK equation with both a temperature-independent volume translation and a crossover model. This approach was found to represent the saturation properties of both CO_2 and light

hydrocarbons very well. When compared with experimental data for mixtures of CO_2 with C_2 to C_5 alkanes, absolute average relative deviations (AARD) in bubble pressure of between 0.4 % and 1.7 % were found, while the AARDs for pressure in single-phase compressed-fluid regions were between 0.4 % and 16 %. Unfortunately, crossover models are not easily extended to multi-component systems and volume translation does not correct the CEOS at conditions far from saturation.

Multi-Fluid Helmholtz Equation of State (MFHEOS) [40], notably the GERG-2008 EOS [41], exploit highly-accurate Helmholtz models for pure substances together with specially developed mixing rules and binary-specific departure functions for mixtures [42]. These models contain many parameters but can perform well when fully optimized by comparison with extensive experimental data. The component slate of GERG-2008 includes CO_2 and the normal alkanes up to C_{10}. Although originally developed to represent natural gas properties, this model can be applied to dense fluid mixtures and has been tested against some high-pressure phase-equilibrium and phase-property data. For example, the binary system (CO_2 + decane) has been investigated by Kandil et al. [33], who measured both compressed-fluid density and bubble pressures at temperatures from (313 to 410) K with pressures up to 76 MPa. They found that densities were predicted to within about 1% by the GERG equation but that bubble pressures were better represented by a CEOS.

In both CEOS and MFHEOS, significant amounts of experimental data are required to determine the binary interaction parameters for all the possible binary pairs in a multi-component mixture. In an effort to limit this reliance on experimental data, more predictive approaches have been developed. The predictive Peng-Robinson equation (PPR-78) and the predictive Soave-Redlich-Kwong equation (PSRK) have been developed by Jaubert and co-workers [43-45]. In this approach, the binary interaction parameters are estimated as functions of temperature using a group contribution method based on the number and type of chemical functional groups present in the interacting molecules. The predictive capability of these CEOS models was demonstrated recently in the description of the fluid phase behaviour and

densities of a multicomponent hydrocarbon system containing dissolved CO_2 [46]. Moreover, in recent years, molecular-based approaches such as the Statistical Associating Fluid Theory (SAFT) have been reformulated as group contribution EOS. One such approach, SAFT-γ Mie, shows great promises as a generic tool for the prediction of thermodynamic properties of a wide variety of systems based on a functional group analysis [47-50]. Nevertheless, rigorous testing of PPR-78, PSRK and SAFT-γ Mie for CO_2-hydrocarbon systems has so far been restricted by a lack of wide-ranging experimental data. In this context, the experimental work presented here is part of a programme of accurate measurements of phase behaviour, saturated-phase and compressed-fluid densities for the binary (CO_2 + hydrocarbon) systems over extremely wide ranges of temperature and pressure, with the objective of permitting these thermodynamic models to be tested in a more rigorous way.

In this paper, we present new density and phase-behaviour measurements of the (CO_2 + heptane) system at temperatures from (283 to 473) K and pressures up to 68 MPa. To the best of our knowledge, this is the first time that such an extensive study has been reported for a CO_2 + hydrocarbon mixture. High-pressure phase equilibria for CO_2 + heptane have been reported in the literature [51-56]. However, most of the measurements are restricted to temperatures below 400 K. Furthermore, there are only a few compressed-fluid density data available for the CO_2 + n-heptane system [51, 57] or, indeed, for other mixtures of CO_2 with hydrocarbons. The saturated phase densities for this particular mixture have not been reported previously at temperatures above 300 K [58]. The new measurements have been carried out in specially-developed apparatus which has been described previously [46, 59, 60]. New empirical models have been developed to represent the densities for the system investigated. Finally, the densities and vapor-liquid-equilibrium data are compared with the predictions of the SAFT-γ Mie [47] and PPR-78 models [44]. Although our main objective is to provide new experimental data suitable for rigorous testing of predictive thermodynamic models, the new data can also be used to optimize binary interaction parameters between CO_2 and n-heptane, for example in a conventional CEOS.

2. Materials and Methods

2.1. Materials

Pure deionized and degassed water (electrical resistivity > 18 MΩ·cm at T = 298.15 K) was used during the calibration process. Carbon dioxide and helium were supplied by BOC with mole fraction purities higher than 0.99995 and 0.99999, respectively, and were used as supplied. Heptane was supplied by Sigma-Aldrich with a mass-fraction purity > 0.99; it was degassed under vacuum before use but no analysis or further purification was carried out.

2.2. Compressed-fluid density apparatus

The measurements reported in this work have been carried out with a vibrating tube densimeter apparatus described in detail in an earlier paper [60]. The equipment consisted of a vibrating tube densimeter (Anton-Paar, DMA HP), a high-pressure syringe pump (DH Budenburg) with a maximum working pressure of 70 MPa, a custom-made variable-volume vessel, and temperature and pressure sensors. The DMA HP module, which housed the high-pressure vibrating-tube sensor, had a built-in thermostat and temperature sensors, capable of controlling and measuring the temperature with an uncertainty of 0.01 K. The DMA HP was connected to a master instrument (Anton Paar DMA 5000) which displayed the measured parameters, including the period of oscillation with a resolution of 0.01 μs. The syringe pump was used for the injection of fluids and to raise pressure during measurements. The pressure was measured using a pressure transducer installed in the connecting tubing. In this work, a variable-volume cell was used for the preparation of the mixtures with CO_2. This vessel [61] was manufactured in type-316 stainless steel with an approximate total volume of 200 mL and a pressure rating of 20 MPa at 373 K. The vessel was fitted with a movable piston which divided the volume into sample- and pneumatic-fluid compartments. A valve atop the vessel permitted flow of the mixture under study into and out of the sample compartment. A second valve in the bottom of the cell permitted injection of nitrogen to drive the piston upwards, thereby compressing the sample. A PTFE-coated magnetic bar was placed inside the cell to permit agitation of the sample by shaking and/or magnetic stirring.

2.2.1. Experimental procedure

CO_2 + n-heptane mixtures were prepared gravimetrically in the variable volume cell by the following procedures. The cell was first cleaned with solvent and dried under vacuum. Then, the degassed heptane was injected into the cell using an HPLC pump in dispensing mode. Next, CO_2 was transferred into the cell from a high-pressure dip-tube liquid CO_2 cylinder. The mass of each component in the cell was determined by weighing the vessel on a high-precision analytical balance (Mettler Toledo, model PR5003) with 0.001 g resolution before and after each addition. The standard uncertainty of the mole fraction was estimated to be less than 10^{-4}.

Once the two fluids were injected into the cell, the mixture was compressed to a pressure above its estimated bubble point, by driving the piston with compressed nitrogen, and the sample was stirred at ambient temperature for approximately two hours. Meanwhile, the entire densimeter set-up was cleaned with solvents, flushed with N_2 and finally evacuated. After that, the binary mixture was slowly transferred directly from the variable volume cell to the densimeter. In order to maintain the homogeneity of the mixture during this procedure, the pressure inside the variable-volume cell was kept constant by moving the piston. Once the pressure in the densimeter was higher than the bubble pressure of mixture, sample was allowed to pass through the densimeter tube into the variable-volume device, so as to displace any material that had phase separated during the initial introduction. The densimeter was then isolated from the sample cell and the measurements started.

Densities of the system $(1 - x)C_7H_{16} + xCO_2$, where x is the mole fraction of CO_2, were measured at temperatures of 283.15 K and from 298.15 K to 473.15 K in steps of 25 K. The measurements proceeded along isotherms starting from an initial pressure (10 MPa in the case of the mixtures) with pressure increments up to a pressure of 65 MPa or 68 MPa; a final check measurement was then made at the initial pressure. No hysteresis was observed going up and down in either temperature or in pressure.

2.3. Two-phase density apparatus

The saturated phase densities were measured using a recently-developed apparatus that has been described in an earlier paper [59]. In brief, the apparatus comprised an equilibrium cell connected through a pair of vibrating tube densimeters (VTDs) to a pair of high-pressure syringe pumps. The equilibrium cell had an internal volume of 50 mL and was placed in an oven with an operating range from 293 K to 473 K and temperature uniformity of better than ± 0.2 K. The top and bottom ports of the equilibrium cell were connected to the VTDs (Anton Paar, DMA-1400) through short sections of tube with minimal hold-up volume. The second port of each densimeter was connected through a coiled buffer tube, with a volume of about 6 mL, to one of the syringe pumps (Quizix model C-5000-10K) located outside the oven. The system pressure was measured using calibrated strain-gauge transducers (Sensata Technology, model 101HP2), one connected to each pump cylinder. Three Pt100 thermometers were used to measure the temperature of the top and bottom VTDs and the equilibrium cell.

2.3.1 Experimental procedure

A two-phase mixture of CO_2 + n-heptane was first prepared in the equilibrium cell using the following procedures. The apparatus was flushed with CO_2 and evacuated several times. Then n-heptane was pumped through the bottom VTD into the equilibrium cell. The injected volume of heptane was usually about 20 mL but, for measurements close to the critical point, only about 10 mL or less was necessary because of the volume expansion of the liquid phase upon dissolution of CO_2. Next, CO_2 was introduced into the cell to achieve the desired pressure. Once both components were inside the cell, the two-phase mixture was stirred until equilibrium, as determined by monitoring the temperature and pressure readings, was reached. The stirrer was then switched off. To measure the density of the saturated liquid phase with the lower VTD, the bottom syringe pump was programmed to withdraw fluid at a rate of (0.1 to 0.5) mL min^{-1}. Meanwhile, the system pressure was maintained constant by

operating the top syringe pump in pressure-control mode. After about 4 mL of sample had been withdrawn, the period of oscillation measured for the bottom VTD stabilised, the bottom syringe pump was stopped and temperature, pressure and the period of oscillation were recorded over a period of 200 s. The standard deviation of the recorded period was required to be less than 0.01 μs for the measurements to be accepted. Following this, the procedure was reversed to enable the measurement of the vapour phase density. The contents of the equilibrium cell were re-mixed for 10 min, the stirrer was switched off and about 4 mL of the saturated-vapor phase was displaced into the top VTD under isothermal and isobaric conditions. After measuring the density of both phases, the pressure was increased by injecting more CO_2 and the next measurement was started. Close to the critical point, very small pressure increments were required. After the maximum pressure had been reached, the sample was slowly vented and the system was configured for measurements at the next temperature. A program written in Keysight VEE was developed to automate all experimental procedures and record the data, permitting enhanced repeatability. Figure S1 in the supplementary material illustrates the repeatability of the data at a temperature of 323 K. On the basis of these experiments, we estimated that the repeatability of our measurement was about 1 $kg \cdot m^{-3}$.

2.4. Vapour-liquid equilibrium apparatus

The synthetic phase equilibrium apparatus used in this work was detailed previously by Al Ghafri et al. [46] and is summarized here. The variable volume equilibrium cell was fitted with a movable piston and a sapphire window, allowing visual observation of the interior of the cell while adjusting the volume and pressure of a sample of fixed composition. A DC servomotor was used to drive the piston under automatic control. Two syringe pumps were used to inject known amounts of the components of interest into the equilibrium cell. A calibrated low-dead volume pressure transducer (DJ Instruments, model DF2) was used for pressure measurements while the cell temperature was measured using a calibrated 4-wire Pt100

sensor inserted into an axial hole in the cell body. The equilibrium cell was encased in a thick aluminium electrically-heated jacket which was used to control the cell temperature.

2.4.1 Experimental procedure

Measured amount of heptane and CO_2 were injected sequentially into the cell. The overall composition of the system was calculated at every stage of the experiment from the cumulative amounts of heptane and CO_2 introduced from the pumps, and calculations of the amount and composition of the fluid remaining in the connecting tubing. Following the injection of components, the pressure inside the cell was adjusted by moving the piston until one homogeneous phase was obtained. The system was then left to equilibrate at a fixed temperature under stirring. The pressure was then decreased in small decrements, each followed by a further equilibration period, while simultaneously recording temperature, pressure and volume, and observing the state of the system. This process continued until the appearance of a second phase. Usually, after observing a bubble- or dew-point, additional CO_2 was injected and a new measurement initiated. This procedure was repeated for different isotherms. The critical pressure at each temperature was estimated from the measured phase envelope as detailed in the Supplementary Material. A more detailed description of the experimental procedure was published previously [46].

2.5 Calibration and uncertainty

All the apparatus was carefully calibrated, and rigorous uncertainty calculations were carried out; both are of the utmost importance in accurate measurements of thermophysical properties. More detailed uncertainty analyses and calibration procedures have been reported previously [46, 60, 62, 63]

The density ρ is related to the period of oscillation τ measured in a vibrating tube densimeter by the relation:

$$\rho(p,T) = A(p,T)\tau^2 - B(p,T)\,. \qquad (1)$$

Here, *A* and *B* are the parameters of the VTD that generally depend upon both pressure and temperature and are determined by calibrations with fluids of known densities. The densimeter in the compressed-fluid density apparatus was calibrated using vacuum and with helium and water at every experimental temperature over the full pressure range. The resulting values of *A* and *B* at each temperature were represented as linear functions of pressure. In the two-phase density apparatus, the calibration of the two densimeters was performed under vacuum at every temperature and in toluene overall the full ranges of temperature and pressure studied. In this case, *A* and *B* were represented by a physical model of the vibrating tube densimeter, together with a constraint on the ratio of the pressure coefficients of tube volume and stiffness, both as detailed by May et al. [62, 63]. In both cases, the densities of the calibration fluids were obtained from the equations of state in the NIST standard reference database REFPROP version 9.1 [64]. The periods of oscillations at vacuum were also checked periodically at the different temperatures to check the continued validity of the calibration.

The pressure transducers were each calibrated over their working ranges against a reference quartz-crystal pressure standard (Fluke, model PPCH-G 70 M) having an expanded uncertainty of 14 kPa at 95% confidence. The Pt100 thermometers were calibrated on the International Temperature Scale of 1990 (ITS-90) at the temperature of the triple point of water and by comparison with a standard platinum resistance thermometer in a calibration bath up to the maximum experimental temperatures [46, 59, 60].

The overall standard uncertainties of the measured data were evaluated following the Guide to the Expression of Uncertainty in Measurement (GUM) [65]. The overall combined expanded uncertainty for the compressed-fluid densities was determined to be $\leq 1\ \mathrm{kg \cdot m^{-3}}$ at 95 % probability over the entire ranges of temperature and pressure investigated. The overall combined expanded uncertainty of the saturated phase densities was estimated to be $\leq 3\ \mathrm{kg \cdot m^{-3}}$, except close to the critical locus where pressure uncertainty becomes dominant. The uncertainty of the bubble- and dew-pressures depended mainly on the subjective uncertainty in observing the bubble- or dew-point condition and the estimated expanded

uncertainty for bubble and dew pressures varied between (0.2 and 0.6) MPa at 95% confidence. Examples of the various contributions to the uncertainties at T = 373.15 K are given in Table 1. All the experimental results, including the associated uncertainties, are given in Tables S1, S5, S6 in the Supplementary Material.

Table 1. Contributions to the standard uncertainty $u(f)$ of compressed-fluid density, saturated-phase density, and bubble- and dew-pressures for (0.2 C_7H_{16} + 0.8 CO_2) at T = 373.15 K.

Apparatus	p/MPa	$u(p)$/MPa	$u(T)$/K	$u(\tau)$/μs	$u(x)$	$u(\rho)$/(kg·m^{-3})
Compressed-fluid density apparatus	20	0.02	0.02	0.01	< 10^{-4}	0.4
Two-phase density apparatus	10	0.5	0.2	0.01		1[a] or 0.4[b]
Vapor-liquid equilibrium apparatus	10	0.2	0.2		10^{-3}	

[a] Vapor phase. [b] Liquid phase.

3. Experimental results and discussion

Compressed-fluid densities of binary mixtures of CO_2 + n-heptane were investigated over the temperature range of (283 to 473) K and pressures up to 68 MPa. The saturated phase densities were measured at temperatures between (293 and 448) K at pressures up to the critical or, at the lowest temperature, the three-phase line. Phase equilibrium measurements are reported at temperatures between (298 and 423) K and at pressures up to 14 MPa.

3.1 Compressed-Fluid Densities

The compressed-fluid densities are given in Table S1 in the Supplementary Material. The results for the two pure components are compared in figures S2 (heptane) and S3 (CO_2) in the supplementary material with the most-accurate multi-parameter reference equations of state available. For CO_2, 90% of the measured data fall within the combined uncertainty of the experiment and the equation of state, while in the case of heptane, all of the measured data agree to within the combined uncertainty. These comparisons provide additional validation of the experimental method and the estimated uncertainties.

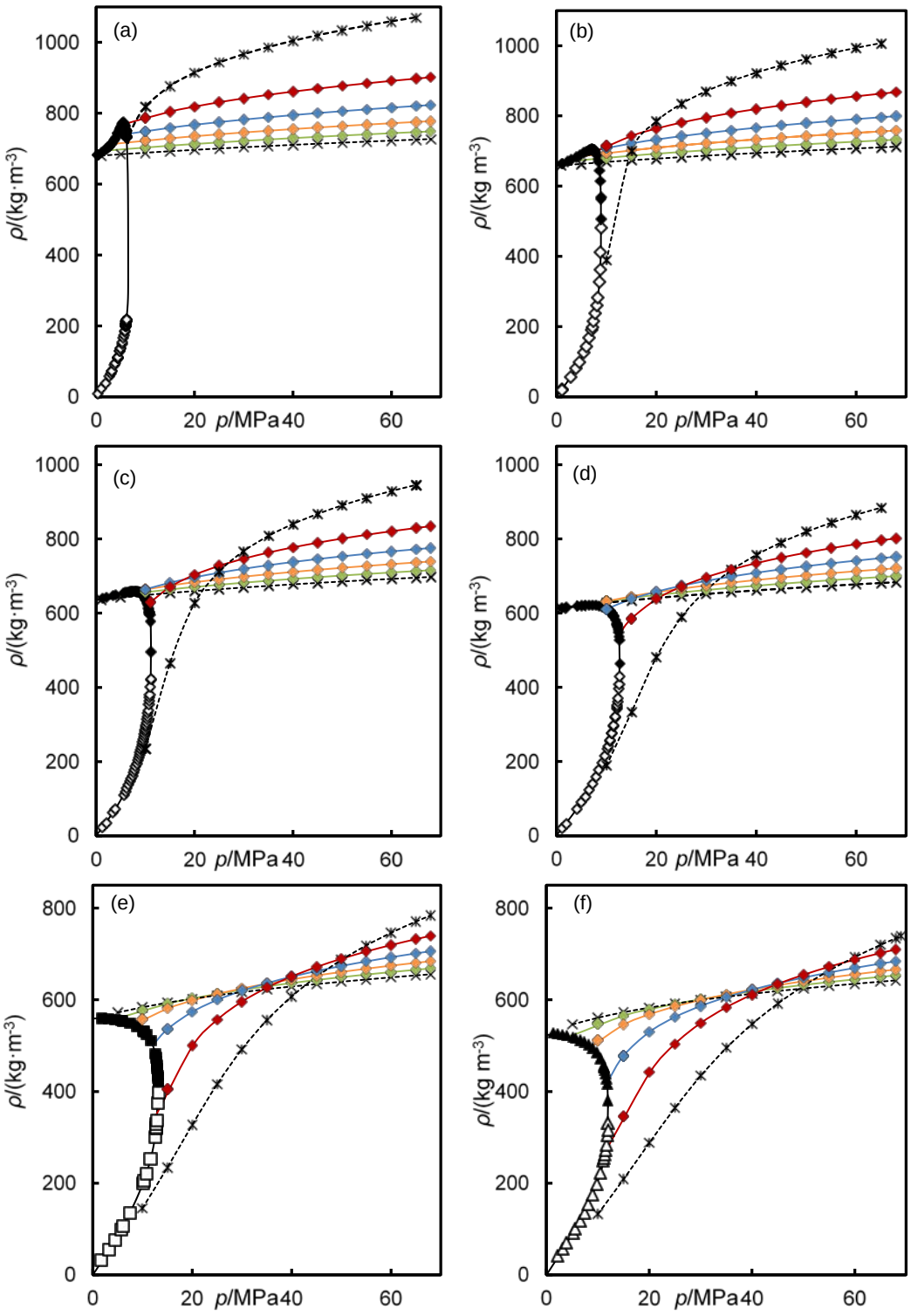

Figure 1. Experimental saturated-phase densities ρ of CO_2 + n-heptane as functions of pressure p: ◆, saturated liquid; ◇, saturated vapor; solid black line calculated from Eq. (5) with parameters from Table S9. Also shown are densities of pure heptane (×), pure CO_2 (∗) and mixtures (colored diamonds) at x = 0.2 (green), x = 0.4 (orange), x = 0.6 (blue) and x = 0.8 (red) and temperatures of: (a) 298.15 K, (b) 323.15 K, (c) 348.15 K, (d) 373.15 K, (e) 423.15 K and (f) 448.15 K. Colored continuous curves and black dashed curves are calculated with Eq.(4) with parameters from Table S8.

In Figure 1, the experimental compressed-fluid densities are plotted as functions of pressure for different temperatures. As expected, at constant composition, the density increased with decreasing temperature and/or increasing pressure. At constant temperature and sufficiently-high pressure, the density increases with increasing mole fraction of CO_2. However, a crossover effect develops with increasing temperature such that, at sufficiently low pressure, the density decreases with increasing mole fraction of CO_2. This effect could be anticipated from the isothermal density-pressure curves of the pure substances. The density crossover behaviour in mixtures of hydrocarbons with CO_2 has also been reported by Medina-Bermudez et al. [66] who measured the compressed-fluid densities of the same binary mixture at temperatures between (313 and 363) K and at pressures up to 25 MPa using a vibrating tube densimeter. We compared experimental data at 323 K and 348 K with the data reported by Medina-Bermudez et al. A linear interpolation in composition was performed with our data for the comparison. Figure S4 in the Supplementary Material shows the comparison with the literature data, and they agreed well with an average absolute relative deviation, Δ_{AARD}, of 0.7 % and average absolute deviation, Δ_{AAD}, of 4 kg·m^{-3}. The compressed-fluid densities of the same mixture were also reported by Fenghour et al. at a temperature range of (302 to 459) K and at pressures up to 55 MPa at 4 predetermined compositions [30]. However, a direct comparison with Fenghour et al. has not been carried out because these data were reported at different compositions, temperatures and pressures.

3.2 Excess Molar Volumes

The excess molar volume V_m^E was calculated from the compressed-fluid densities according to the relation:

$$V_m^E = \frac{M_{mix}}{\rho_{mix}} - \left(\frac{xM_1}{\rho_1} + \frac{(1-x)M_2}{\rho_2} \right), \quad (2)$$

where x is the CO_2 mole fraction, M is the molar mass and subscripts 1 and 2 denote properties of CO_2 and heptane, respectively. Figure 2 shows plots of V_m^E as functions of x across six

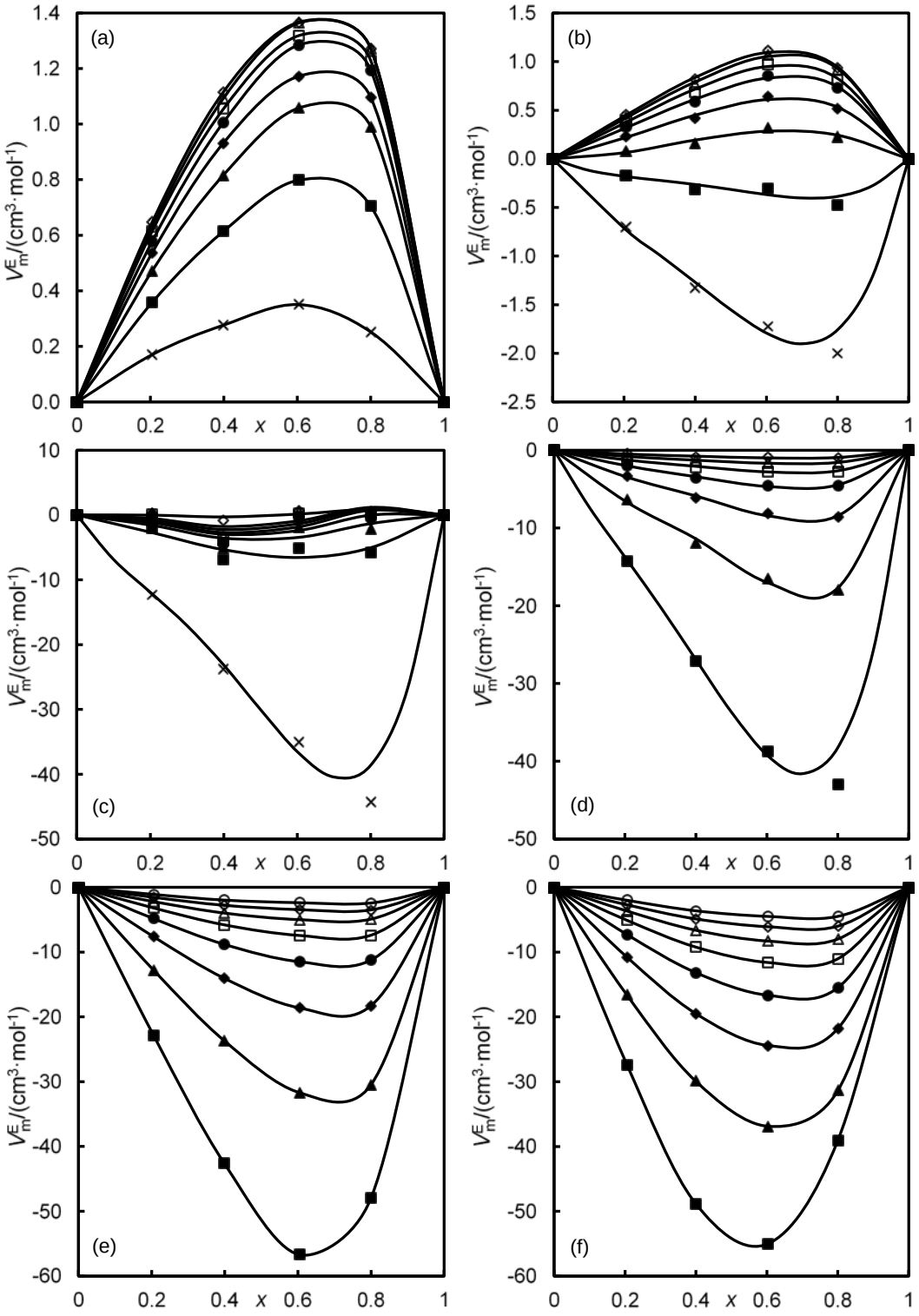

Figure 2: Excess molar volume V_m^E of CO_2 + n-heptane as functions the mole fraction x of CO_2 at pressures of: ×,10 MPa; ■, 15 MPa; ▲, 20 MPa; ◆, 25 MPa; ●, 30 MPa; □, 35 MPa; △, 40 MPa; ◇, 45 MPa; ○, 50 MPa. (a) T = 283.15 K; (b) T = 298.15 K; (c) T = 323.15 K; (d) T = 373.15 K; (e) T = 423.15 K; (f) T = 473.15 K. Solid lines represent values calculated from Eq (3) with parameters from Table S4.

isotherms. In the composition range investigated, V_m^E becomes more negative with increasing temperature, but less negative with increasing pressure. The excess molar volume was slightly positive at 283 K for all pressures considered and at 298 K for pressures above 15 MPa, regions in which pure CO_2 is a liquid. At T = 323 K and pressures higher than 10 MPa, V_m^E displayed a sigmoidal pattern. At all higher temperatures, the excess molar volume was negative over the entire range of composition and increased in magnitude with increasing temperature and decreasing pressure. These large negative excess volumes are typical of a gas or super-critical fluid dissolving in a normal liquid and reflect partly the insertion of CO_2 molecules into the free volume of the liquid. The extrema always occurred for CO_2 mole fractions of between 0.6 and 0.7.

The excess molar volume has been correlated with the Redlich-Kister equation which is given in the following form:

$$V_m^E = x(1-x)\sum_{i=1}^{3} A_i(2x-1)^{i-1} \quad (3)$$

Here, A_i are parameter fitted to the experimental data at every temperature and pressure. The results of the correlation are plotted in Figure 2 and generally follow the experimental data quite precisiely. The goodness of the fit, as measured by the average absolute deviation Δ_{AAD}, was 0.03 $cm^3 \cdot mol^{-1}$ averaged across all isotherms and isobars. The parameters determined are listed in Table S4 in the Supplementary Material. These Redlich-Kister parameters may be helpful for interpolation of the experimental data to intermediate compositions.

3.3 Saturated-Phase Densities

The saturated-phase densities for both vapour and liquid phases are also plotted in Figure 1 and are tabulated in Table S5 in the Supplementary Material. On most of the isotherms investigated, the bubble-point densities decreased, and the dew-point densities increased, monotonically with increasing pressure. However, at temperatures between 298 K and 348 K, the bubble-point densities initially increased with increasing pressure until a maximum was

reached after which they decreased monotonically to the critical point. Figure 1 also shows the densities for pure n-heptane measured in this work. Comparing the liquid-phase densities for CO_2 + n-heptane mixtures and the densities of pure heptane at the same pressure and temperature, it can be observed that the mixture density was greater than pure heptane at temperatures between 298 K and 348 K below a certain pressure. In the rest of the states investigated, the mixture density was always lower than that of pure heptane. The experimental data at 298 K were compared with the only data reported in the literature, those of Rabe [58]. Figure S5 in the supplementary material shows the comparison and it can be seen that the data of Rabe [58] are in very good agreement with our results.

3.4 Bubble- and Dew-Points

Bubble- and dew-pressures were measured at temperatures of 298 K, 323 K, 373 K and 423 K and at pressures up to 14 MPa. The experimental data are plotted in Figure 3 and tabulated in Table S6 in the Supplementary Material. Figure 3 also shows the available literature data reported by Mutelet et al. [53], Lay et al.[67] , and He et al. [52] and it can be seen that there is good agreement. In this work, the mixture critical points were also determined; the values are given in Table S7 in the Supplementary Material and are plotted in Figure 4, together with data reported in the literature [68-71]. Again, the agreement is generally good except for one datum of Choi at al. [69]. The CO_2 + heptane system shows Type-II phase behaviour in the classification of Scott and Konynenburg [72], so there is a continuous critical locus connecting the critical points of CO_2 and heptane and a three-phase vapor-liquid-liquid equilibrium line at temperatures below the critical temperature of CO_2. Figure 4 also shows the *p, T* projection of the critical locus calculated using the procedure of Heidemann and Khalil [73] from the Peng-Robinson equation of state [19], as well as the critical curve predicted with SAFT-γ Mie [48]. In general, the Peng-Robinson and SAFT-γ Mie models describe the critical curve relatively well across the calculated temperature range.

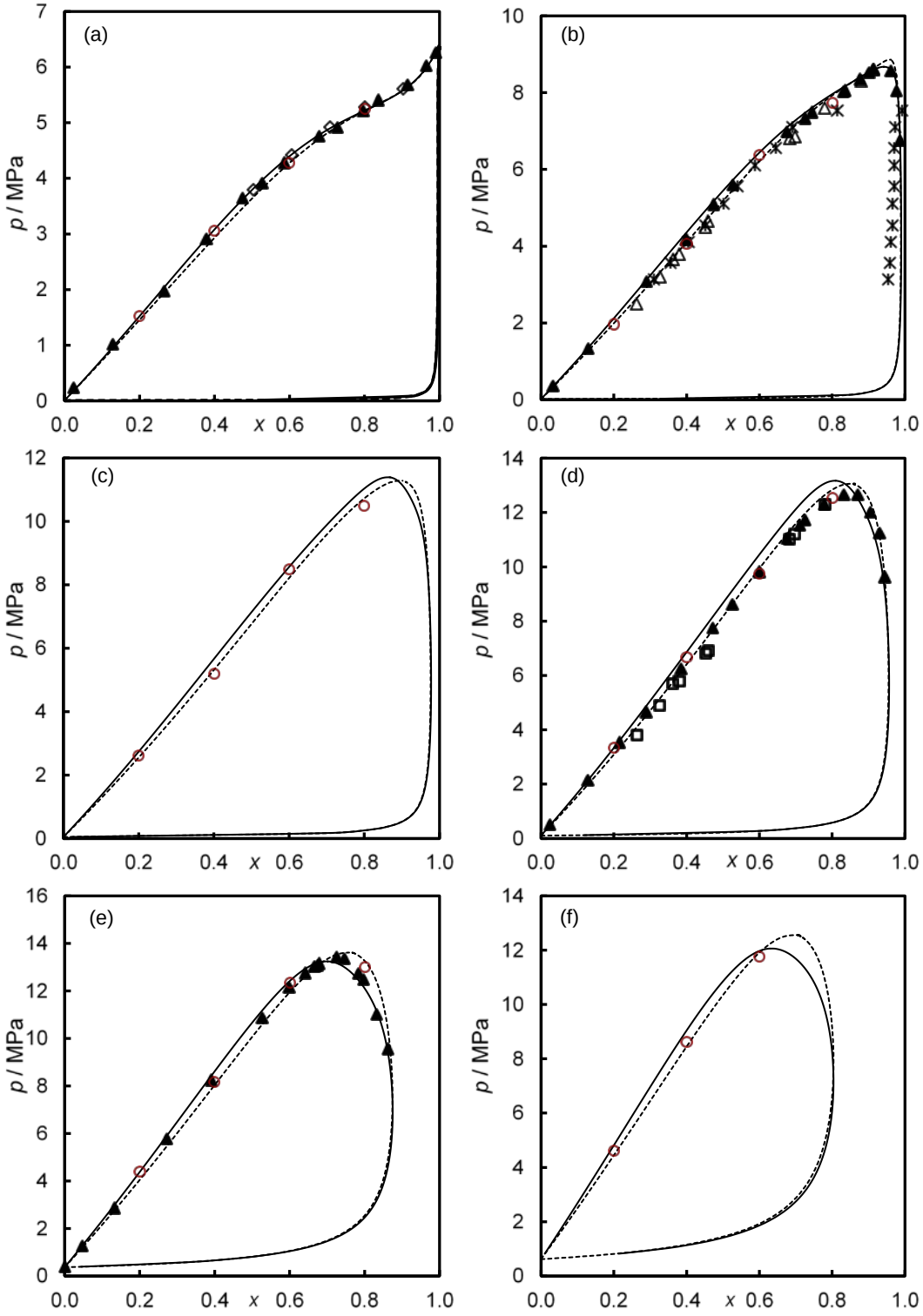

Figure 3. Bubble and dew-point pressures p for (CO_2 + n-heptane) as a function of the mole fraction x of CO_2 at temperatures: (a) 298.15 K, (b) 323.15 K, (c) 348.15 K, (d) 373.15 K, (e) 423.15.15 K and (f) 448.15 K. This work: ▲, VLE measurements; ○, values from the intersection of the compressed-fluid densities and the saturated phase densities. Literature data: ◇, Lay [67]; ∗, He et al. [52]; △, Mutelet et al. [53]; □, Mutelet et al. [53]. Solid line and dashed line represent the predictions from SAFT-γ Mie and PPR-78 EoS, respectively.

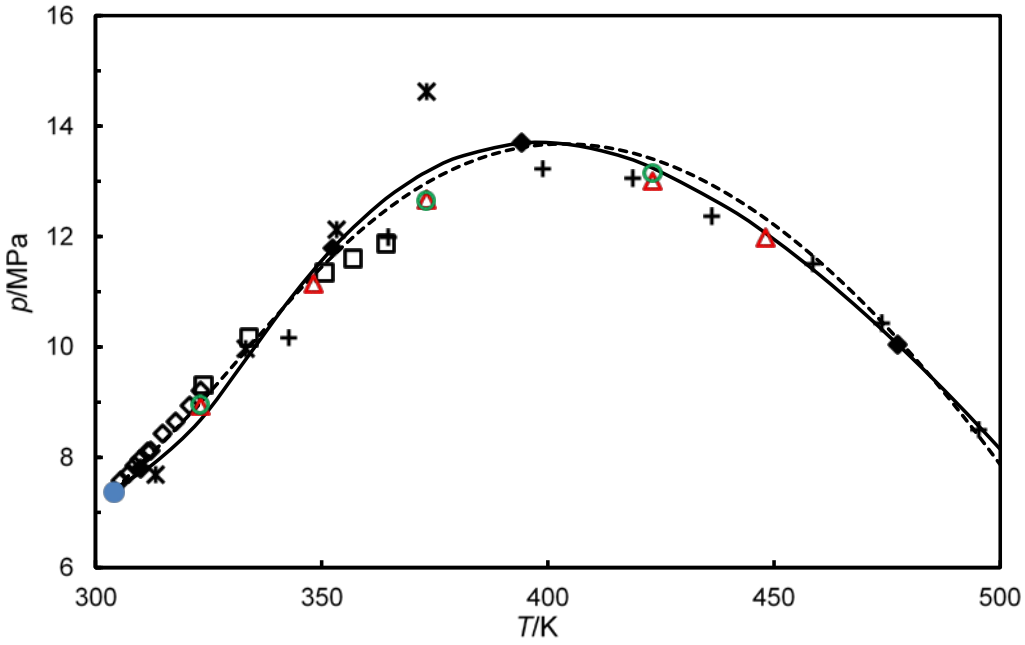

Figure 4. *p*, *T* projection of the critical locus for CO_2 + n-heptane system: ○, in this work (VLE measurements); △, this work (saturated phase densities); ◇, Gurdial et al. [68]; □, Choi et al. [69]; ∗, Sun et al.[70]; ◆, Kalra et al. [74]; +, Juntarachat et al. [71]; ●, critical point of pure CO_2. Dashed line calculated using the procedure of Heidemann and Khalil [73] and the Peng–Robinson equation of state. Solid curve calculated using the SAFT-γ Mie approach.

3.5 Further Analysis

To verify the consistency of the experimental data, we developed new empirical correlations for the compressed-fluid and saturated-phase densities and used these simultaneously to determine both pressure and density at the bubble- or dew-point conditions of mixtures of known composition at given temperature.

The empirical correlation developed to describe the compressed-fluid densities at each temperature and composition was of the following pressure-explicit form:

$$p = A\rho + B\frac{(\rho - \rho_r)^{\delta}}{\delta}. \qquad (4)$$

Here, ρ_r is a reference density which was a floating parameter along with *A* and *B*. The non-linear term was introduced to describe the non-analytic behavior of the densities in the critical region with critical exponent δ = 4.82 [75]. Parameters *A*, *B* and ρ_r, were determined by non-

linear regression using the Lenvenberg-Marquardt optimization method. Figure 1 shows curves calculated from equation (4). The parameters are summarised in Table S8 and the deviation plots between the calculated values and experimental compressed-fluid densities are shown in Figure S7 in the Supplementary Material. The Δ_{AAD} and Δ_{AARD} of the correlation were about 0.05 MPa and 0.25%, respectively. The accuracy of the correlation decreased with increasing CO_2 mole fraction in the mixtures due to the pronounced non-linear behaviour around the critical region. The fit might be improved be including additional polynomial terms.

The experimental saturated liquid-phase and vapor-phase densities, ρ_L and ρ_V, respectively, were fitted on each isotherm using a second empirical correlation also incorporating an appropriate non-analytic term to capture the near-critical behavior. The correlation is given in the following form:

$$\left.\begin{aligned} \rho_L - \rho_V &= \sum_{i=1}^{2\text{ or }3} A_i (p_c - p)^i + C(p_c - p)^\beta \\ \rho_L + \rho_V &= 2\rho_c + \sum_{i=1}^{2\text{ or }3} B_i (p_c - p)^i + D(p_c - p)^\beta \end{aligned}\right\}. \quad (5)$$

Here, β is a universal critical exponent with the value of 0.325, p_c is the critical pressure and ρ_c is the critical density. The parameters A_i, B_i, p_c and ρ_c were determined by non-linear regression, again using the Lenvenberg-Marquardt algorithm. To help constrain the correlation at $p = 0$, the liquid-phase density was set to the density of pure heptane and the vapour-phase density was set to zero. Densities calculated from equation (5) are also plotted in Figure 1. Table S9 in the Supplementary Material lists the values of the fitting parameters and the absolute average deviation at each temperature; deviations of the experimental densities are also plotted in Figure S8. The Δ_{AAD} and Δ_{AARD} were 1 kg·m^{-3} and 0.7 %, excluding the density data close to the critical point. This correlation permitted reliable estimations of the critical pressure (plotted in figure 4) and the critical density.

Solving equations (4) and (5) simultaneously, one can obtain pressure and density for saturated states of given composition and temperature. Bubble-pressures (and one dew-

pressure) so determined are compared with the direct VLE measurements in figure 3 and are tabulated in Table S10 in Supplementary Material. Our calculated bubble- and dew-pressures agree with the experimental bubble pressures to within about ± 0.1 MPa, which is well within the experimental uncertainty of the VLE measurements. Our procedure is a novel method for determining the bubble pressures of a binary systems from density measurements.

4. Modelling

In this work, the capabilities of the Predictive Peng Robinson (PPR-78) [45] and SAFT-γ Mie [48] models were tested against all the measured properties: saturated-phase densities, compressed-fluid densities and phase behaviour data. No parameters were adjusted for either model.

The Peng-Robison equation of state [27] was used with classical mixing rules for the attractive and repulsive parameters, a and b, respectively, given by:

$$\left.\begin{aligned} a &= \sum_{i=1}^{N}\sum_{j=1}^{N} x_i x_j \sqrt{a_i a_j}\left[1-k_{ij}(T)\right] \\ b &= \sum_{i=1}^{N} x_i b_i \end{aligned}\right\} \qquad (6)$$

The binary interaction parameters $k_{ij}(T) = k_{ji}(T)$ were obtained from the group-contribution approach of Jaubert and co-workers [44, 45] as follows:

$$k_{ij}(T) = \left[\left\{-\frac{1}{2}\sum_{k=1}^{N_g}\sum_{l=1}^{N_g}(\alpha_{ik}-\alpha_{jk})(\alpha_{il}-\alpha_{ji})A_{kl}(T_0/T)^{(B_{kl}/A_{kl}-1)}\right\}-\left\{\frac{\sqrt{a_i(T)}}{b_i}-\frac{\sqrt{a_j(T)}}{b_j}\right\}^2\right]\times\left[\frac{2\sqrt{a_i(T)a_j(T)}}{b_i b_j}\right]^{-1} \qquad (7)$$

Here, N_g is the number of distinct functional groups present in the molecule, α_{ik} is the number of occurrences of group k in component i divided by the total number of groups present in that component, A_{kl} and B_{kl} are group parameters, and T_0 = 298.15 K. Jaubert and co-workers [43-45] defined 21 functional groups and determined the group parameters A_{kl} and B_{kl} by fitting a very large database of binary VLE data. The resulting model is called the Predictive Peng-

Robinson (PPR-78) EoS. Predictions for density and phase equilibrium states using the PPR-78 model were calculated using the Aspen Plus Properties software package [76].

We have also explored the predictive capability of the SAFT-γ Mie equation of state to describe the phase equilibria and densities of the mixture. This model has been recently developed by Papaioannou and co-workers [47-50]. The SAFT-γ Mie equation of state is a SAFT-based group-contribution approach in which the molecules are treated as assemblies of distinct functional groups (segments), using a fused heteronuclear model, and the segment-segment interaction is represented by a Mie (generalized Lennard-Jonesium) potential. Each functional group is fully described by a number of parameters that were determined by regression against the experimental thermophysical properties of either pure components or binary mixtures that contains each group. Group parameters for the description of the CO_2 + n-heptane mixture have been recently reported by Papaioannou et al. [48, 49]. In this case, all parameters needed to characterize the CH_2 and CH_3 groups and their cross interactions were estimated from experimental vapour pressure, saturated liquid density and single-phase densities of pure n-alkanes from ethane to n-decane [48]. The parameters for the CO_2 molecular group were estimated from its vapour pressure and saturated liquid density. For the unlike interactions involving CO_2, the group dispersion energies parameters were estimated from experimental VLE data for CO_2 + n-decane and CO_2 + n-pentane at temperature between 344 K and 378 K, while the remaining parameters were obtained from combining rules. The computations with SAFT-γ Mie were carried out in the gPROMS© software developed by PSE Ltd [77].

The compressed-fluid densities predicted by the PPR-78 and SAFT-γ Mie models are compared with the experimental data in Figure 5. The predictions from both models are quite similar, with the models generally over-predicting the mixture densities at low temperatures and under-predicted them at high temperatures regardless of the composition. The densities calculated from the SAFT-γ Mie model generally have a more accurate gradient but are offset

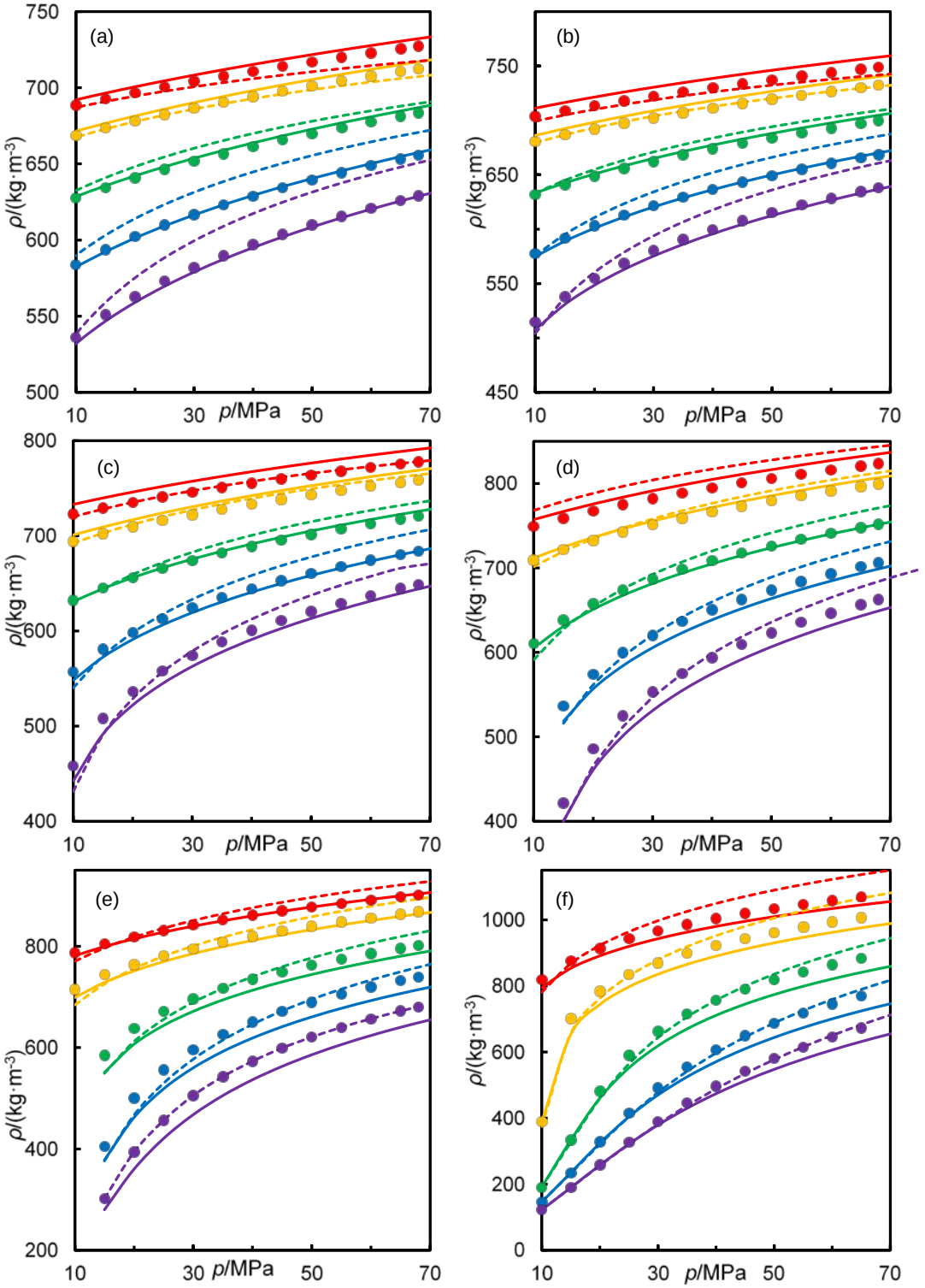

Figure 5. Comparisons between experimental densities ρ of (1 - x) C_7H_{16} + x CO_2 (●) and predictions from SAFT-γ Mie (solid lines) and PPR-78 EoS (dashed lines) as a function of pressure p at temperatures of 298.15 K (red), 323.15 K (yellow), 373.15 K (green), 423.15 K (blue) and 473.15 K (purple): (a) x = 0.0; (b) x = 0.2; (c) x = 0.4; (d) x = 0.6; (e) x = 0.8; (f) x = 1.0.

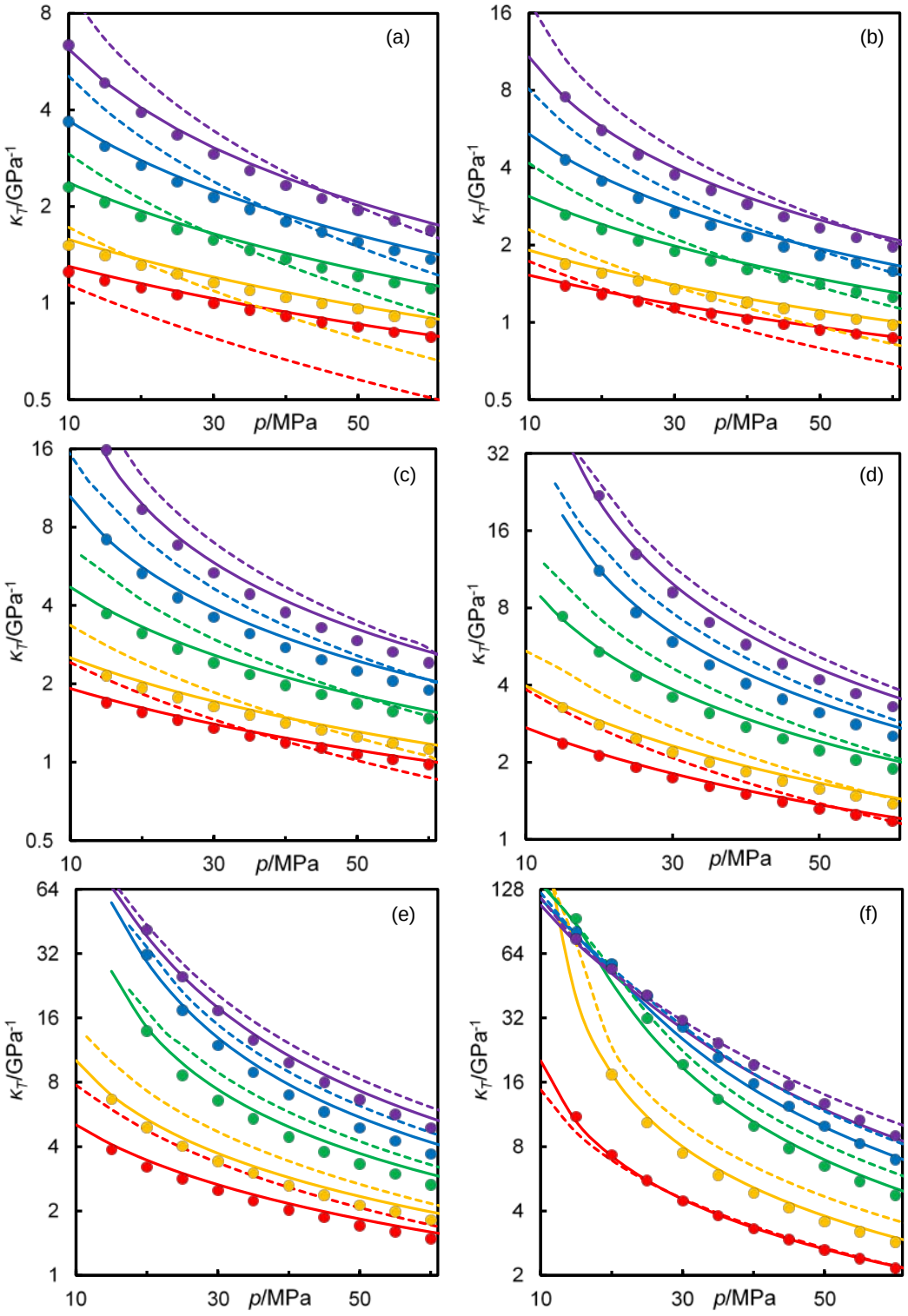

Figure 6. Comparisons between experimental isothermal compressibilities κ_T of (1 - x) C_7H_{16} + x CO_2 (●) and predictions from SAFT-γ Mie (solid lines) and PPR-78 EoS (dashed lines) as a function of pressure p at temperatures of 298.15 K (red), 323.15 K (yellow), 373.15 K (green), 423.15 K (blue) and 473.15 K (purple): (a) x = 0.0; (b) x = 0.2; (c) x = 0.4; (d) x = 0.6; (e) x = 0.8; (f) x = 1.0.

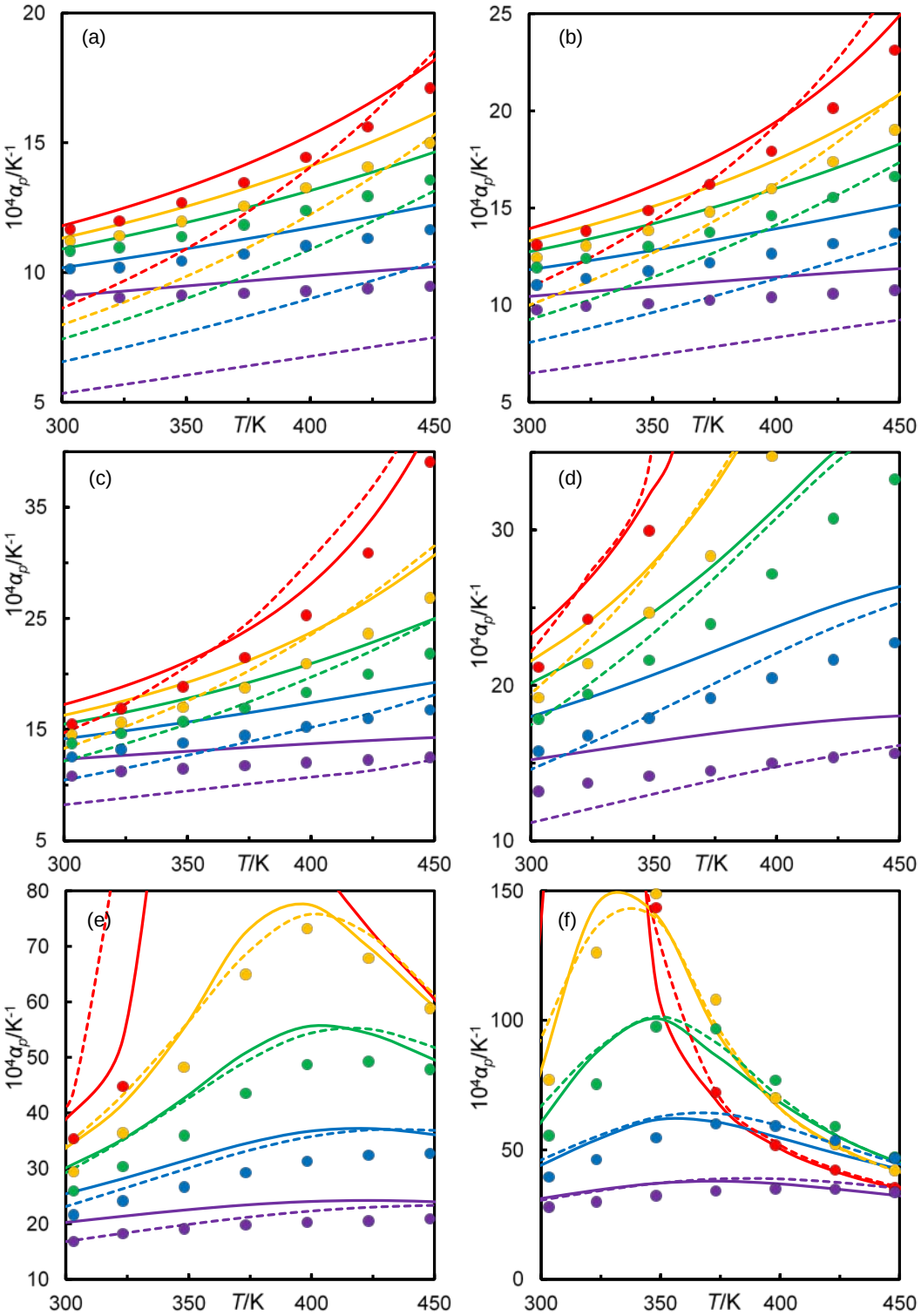

Figure 7. Comparisons between experimental isobaric expansivities α_p of (1 - x) C_7H_{16} + x CO_2 (●) and predictions from SAFT-γ Mie (solid lines) and PPR-78 EoS (dashed lines) as a function of temperature T at pressures of 10 MPa (red), 15 MPa (yellow), 20 MPa (green), 30 MPa (blue) and 50 MPa (purple): (a) x = 0.0; (b) x = 0.2; (c) x = 0.4; (d) x = 0.6; (e) x = 0.8; (f) x = 1.0.

from the experimental data, especially at high mole fractions of CO_2. Deviations of the data from the two models are plotted in Figure S9 in the Supplementary Material; these are characterized by Δ_{AAD} = 11 kg·m^{-3} and Δ_{AARD} = 2 % in both cases.

The isothermal compressibility κ_T and the isobaric expansivity α_p, obtained by numerical differentiation of ln(ρ), are plotted in Figures 6 and 7, respectively, and compared with the predictions of PPR-78 and SAFT-γ Mie. The numerical values of κ_T and α_p are also reported in Tables S2 and S3 in the Supplementary Material. Figure 6 demonstrates that SAFT-γ Mie is greatly superior to PPR-78 in the prediction of compressibility with Δ_{AARD} = 6 %, compared to a figure of 18 % for PPR-78. The PPR-78 model is especially inaccurate for the mixtures rich in heptane. Figure 7 shows large discrepancies between the experimentally-derived expansivities and the PPR-78 model, especially for heptane-rich mixtures. SAFT-γ Mie follows the experimental data more closely for heptane-rich mixtures but generally over predicts α_p, especially for intermediate compositions, leading to the under prediction of density at high temperatures seen in Figures 6(b) to 6(e).

The saturated-phase density predictions are shown Figure 8. It can be seen that the SAFT-γ Mie model generally provided superior predictions of the saturated-liquid densities for this mixture with Δ_{AARD} = 1.8 %, compared with 4.2 % for PPR-78. On the other hand, the experimental dew-point densities are better predicted by PPR-78 with Δ_{AARD} = 2.5 %, compared with 6.3 % for SAFT-γ Mie. The predictive capability of both models declines in the critical region. In this connection, it is worth noting that SAFT-γ Mie was parameterized mainly with sub-critical pure-component data and that experimental data close to the pure-component critical points were not considered [48].

Comparing the SAFT-γ Mie predictions for compressed-fluid densities and saturated-liquid densities, we see that the deviations are higher for the compressed-fluid. It seem likely that regression of the model parameters against a wider range of experimental data, including high-pressures and supercritical states, would result in a more robust and accurate model. In

the case of the PPR-78 model, the predictions of density are generally poor and there is little scope for improvment it in this regard.

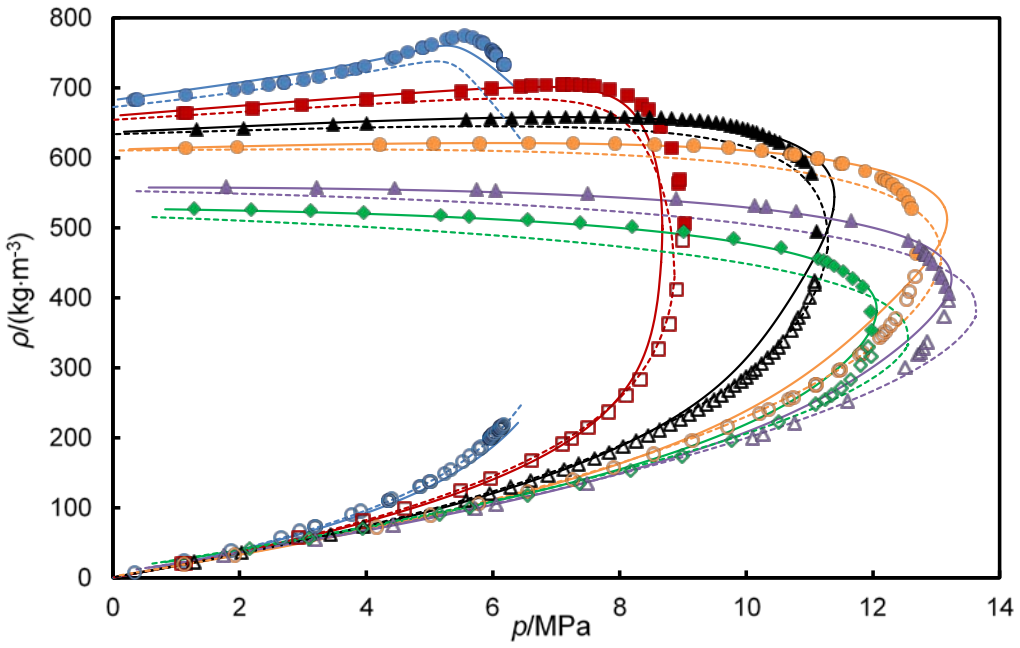

Figure 8. Comparisons between experimental saturated phase densities ρ of CO_2 + n-heptane and predictions from SAFT-γ Mie (solid lines) and PPR-78 EoS (dashed lines) as a function of pressure p at temperatures of 298 K (blue circles), 323 K (red squares), 348 K (black triangles), 373 K (orange circles), 423 K (purple triangles), and 448 K (green diamonds).

Additionally, both PPR-78 and SAFT-γ Mie were tested in their ability to predict the experimental bubble and dew pressures. This comparison is shown in Figure 3. The predictions of SAFT-γ Mie and PPR-78 are both in good agreement with the experimental data, but there are small differences between the models. The good description obtained by both models indicates the good capability to predict the VLE of CO_2 + hydrocarbons systems. Phase behaviour measurements were the best described among all experimental data reported herein.

An optimisation was carried out in the SAFT-γ Mie model to see whether predictions for the compressed-fluid density of CO_2 + n-heptane could be improved by changing the unlike group interaction parameters. This optimisation was performed using the SAFT Material Modeler

developed by PSE Ltd [77]. Unfortunately, little improvement was possible and it seems likely that a more wide-ranging re-appraisal of the parameter tables would be necessary to further optimize the performance of the model.

Finally, we have also compared the experimental data gathered in this work with the predictions of the GERG-2008 equation of state [41]. These comparisons are detailed in section 6.2 of the Supplementary Material which includes graphical comparisons in Figures S10, S11 and S12. It was found that the model predicts the VLE data with lower accuracy than either of the other two models, with large deviations in the critical region. While GERG-2008 provides an excellent representation of the densities of the two pure components, predictions of the saturated-phase and compressed-fluid densities of the mixtures are no better than for the other models investigated and notably poorer in the critical region. Overall we find for saturated-fluid densities Δ_{AARD} = 5.5 %, saturated-vapor densities Δ_{AARD} = 7.1 %, and for compressed-fluid densities Δ_{AARD} = 1.7 %. These results are perhaps not surprising as GERG-2008 contains no binary-specific departure function for the (CO_2 + heptane) binary.

5. Conclusions

This work provides a comprehensive and wide-ranging set of benchmark experimental data for the thermodynamic properties and phase behavior of a simple hydrocarbon-CO_2 mixture. Such a data set is bound to constitute a rigorous test for any thermodynamic model, especially those without adjustable parameters, and it is perhaps not surprising that both predictive models tested failed to describe the data to within the experimental uncertainties. The PPR-78 model offers a good description of the phase behavior. This most probably reflects the fact that the model parameters were regressed exclusively against VLE data. The PPR-78 is poor in the prediction of mixtures density, especially for the saturated liquid and for compressed-fluid states. There is little that can be done globally without destroying the good agreement with VLE data. We can conclude that the performance of this generalized group-contribution CEOS model is not worse than that of conventional CEOS models in which the binary parameters were regressed against the data [29, 30, 32, 34, 39]. The SAFT-γ Mie approach

is similarly good for the VLE data and significantly better for the saturated-phase densities. Although no more accurate than PPR-78 for the compressed-fluid densities, SAFT-γ Mie is much more accurate for the compressibility and expansivity of the system. This model contains a much larger number of parameters and these have thus far been determined largely from VLE and other relatively-low-pressure and data at sub-critical temperatures. There would seem to be scope for a re-parameterization of the model against more wide-ranging and richer data sets including, as in the present work, super-critical and high-pressure states. This may well lead to significant improvements.

Despite the short comings identified in the models considered in this work, the comparisons that we present in this paper provide an indication of the accuracy currently achievable with predictive thermodynamic models under reservoir-like conditions. This may already be sufficient for application in the design of CO_2-storage and CO_2-EOR processes.

The predictions of the GERG-2008 model deviate considerably from the experimental data but we note that the present study provides a rich data set against which to optimize the parameters of an improved model.

Acknowledgements

This work was carried out as part of the activities of the Qatar Carbonates and Carbon Storage Research Centre (QCCSRC). We gratefully acknowledge the funding of QCCSRC provided jointly by Qatar Petroleum, Shell, and the Qatar Science and Technology Park, and their permission to publish this research. W J Tay acknowledges financial support provided by an EPSRC Doctoral Training Award.

References

[1] Blasing T. Recent greenhouse gas concentrations. ESS-DIVE (Environmental System Science Data Infrastructure for a Virtual Ecosystem); Oak Ridge National Laboratory (ORNL), Oak Ridge, TN (United States); 2016.

[2] Rackley SA. Carbon capture and storage. Oxford: Butterworth-Heinemann; 2010.

[3] Gale J. IEAGHG Information Paper:2016-IP7, Update on CO_2 emissions and global temperatures. USA: The national Oceanographic and Atmospheric Administration (NOAA) USA; 2016.

[4] Report of the Conference of the Parties on its twenty-first session, held in Paris from 30 November to 13 December 2015. Part one: Proceedings. Geneva2016.

[5] IEA. Energy Technology Perspective. Paris, France: International Energy Agency; 2015.

[6] Bhave A, Taylor RHS, Fennell P, Livingston WR, Shah N, Mac Dowell N, et al. Screening and techno-economic assessment of biomass-based power generation with CCS technologies to meet 2050 CO_2 targets. Appl Energ. 2017;190:481-9.

[7] Working Group III of the Intergovernmental Panel on Climate Change. IPCC Special Report on Carbon Dioxide Capture and Storage. In: Metz B, Davidson O, de Coninck H, Loos M, Meyer L, editors. Cambridge: IPCC; 2005. p. 442.

[8] Bachu S. CO_2 storage in geological media: Role, means, status and barriers to deployment. Prog Energy Combust Sci. 2008;34:254-73.

[9] Leung DYC, Caramanna G, Maroto-Valer MM. An overview of current status of carbon dioxide capture and storage technologies. Renew Sustainable Energy Rev. 2014;39:426-43.

[10] Carey BS. The gradient theory of fluid interfaces [PhD]: University of Minneapolis; 1979.

[11] Budinis S, Krevor S, Mac Dowell N, Brandon N, Hawkesam A. Can technology unlock 'unburnable carbon'? : Sustainable Gas Institute, Imperial College London; May 2016.

[12] Schou Perdersen K, Christensen PL. Phase Behavior of Petroleum Reservoir Fluids. London: CRC Press Taylor and Francis Group; 2006.

[13] Orr FM, Taber JJ. Use of carbon dioxide in enhanced oil recovery. Science. 1984;224:563-9.

[14] Bachu S. Sequestration of CO_2 in geological media: criteria and approach for site selection in response to climate change. Energy Convers Manage. 2000;41:953-70.

[15] Blunt M, Fayers FJ, Orr Jr FM. Carbon dioxide in enhanced oil recovery. Energy Convers Manage. 1993;34:1197-204.

[16] National Energy Technology Laboratory UDoE. Carbon Dioxide Enhanced Oil Recovery. Untapped Domestic Energy Supply and Long Term Carbon Storage Solution. 2010.

[17] Oldenburg CM, Pruess K, Benson SM. Process Modeling of CO2 Injection into Natural Gas Reservoirs for Carbon Sequestration and Enhanced Gas Recovery. Energy Fuels. 2001;15:293-8.

[18] Patel MJ, May EF, Johns ML. High-fidelity reservoir simulations of enhanced gas recovery with supercritical CO2. Energy. 2016;111:548-59.

[19] Asghari K, Al-Dliwe A, Mahinpey N. Effect of operational parameters on carbon dioxide storage capacity in a heterogeneous oil reservoir: A case study. Ind Eng Chem Res. 2006;45:2452-6.

[20] McHugh MA, Krukonis VJ. Supercritical Fluid Extraction: Principles and Practice. 2nd Edition ed: Butterworth Heinemann; 1994.

[21] Brunner G. Applications of Supercritical Fluids. Annual Review of Chemical and Biomolecular Engineering. 2010;1:321-42.

[22] Munkejord ST, Hammer M, Lovseth SW. CO_2 transport: Data and models - A review. Appl Energ. 2016;169:499-523.

[23] Li H, Jakobsen JP, Wilhelmsen O, Yan J. PVTxy properties of CO_2 mixtures relevant for CO_2 capture, transport and storage: Review of available experimental data and theoretical models. Appl Energ. 2011;88:3567-79.

[24] Løvseth SW, Stang HGJ, Austegard A, Westman SF, Span R, Wegge R. Measurements of CO_2-rich Mixture Properties: Status and CCS Needs. Energy Procedia. 2016;86:469-78.

[25] Li H, Yan J. Impacts of equations of state (EOS) and impurities on the volume calculation of CO_2 mixtures in the applications of CO_2 capture and storage (CCS) processes. Appl Energ. 2009;86:2760-70.
[26] Li H, Yan J. Evaluating cubic equations of state for calculation of vapor-liquid equilibrium of CO_2 and CO_2-mixtures for CO_2 capture and storage processes. Appl Energ. 2009;86:826-36.
[27] Peng D-Y, Robinson DB. A new two-constant equation of state. Ind Eng Chem Fundam. 1976;15:59-64.
[28] Soave G. Equilibrium constants from a modified Redlich-Kwong equation of state. Chem Eng Sci. 1972;27:1197-203.
[29] Kariznovi M, Nourozieh H, Abedi J. Phase composition and saturated liquid properties in binary and ternary systems containing carbon dioxide, n-Decane, and n-Tetradecane. J Chem Thermodyn. 2013;57:189-96.
[30] Kariznovi M, Nourozieh H, Abedi J. Measurement and equation of state prediction of vapor–liquid equilibrium and physical properties for the system methane + n-Octadecane. Fluid Phase Equilib. 2012;314:102-6.
[31] Kariznovi M, Nourozieh H, Abedi J. Experimental results and thermodynamic investigation of carbon dioxide solubility in heavy liquid hydrocarbons and corresponding phase properties. Fluid Phase Equilib. 2013;339:105-11.
[32] Nourozieh H, Bayestehparvin B, Kariznovi M, Abedi J. Equilibrium Properties of (Carbon Dioxide + n-Decane + n-Octadecane) Systems: Experiments and Thermodynamic Modeling. J Chem Eng Data. 2013;58:1236-43.
[33] Kandil ME, Al-Saifi NM, Sultan AS. Simulation and measurements of volumetric and phase behavior of carbon dioxide plus higher alkanes at high pressure: CO_2 + n-decane at temperatures (313-410) K and pressures up to 76MPa. IntJ Greenhouse Gas Control. 2016;53:198-206.
[34] Cismondi M, Rodriguez-Reartes SB, Milanesio JM, Zabaloy MS. Phase Equilibria of CO_2+n-Alkane Binary Systems in Wide Ranges of Conditions: Development of Predictive Correlations Based on Cubic Mixing Rules. Ind Eng Chem Res. 2012;51:6232-50.
[35] Péneloux A, Rauzy E, Fréze R. A consistent correction for Redlich-Kwong-Soave volumes. Fluid Phase Equilib. 1982;8:7-23.
[36] White JA. Contribution of Fluctuations to Thermal-Properties of Fluids with Attractive Forces of Limited Range - Theory Compared with P-ρ-T and C_v Data for Argon. Fluid Phase Equilib. 1992;75:53-64.
[37] Llovell F, Vega LF, Seiltgens D, Mejia A, Segura H. An accurate direct technique for parametrizing cubic equations of state - Part III. Application of a crossover treatment. Fluid Phase Equilib. 2008;264:201-10.
[38] Kiselev SB, Friend DG. Cubic crossover equation of state for mixtures. Fluid Phase Equilib. 1999;162:51-82.
[39] Shen AJ, Liu Q, Duan YY, Yang Z. Crossover VTSRK equation of state for selected alkane plus alkane and CO_2 + alkane binary mixtures. Fluid Phase Equilib. 2016;408:180-9.
[40] Lemmon EW. A Generalized Model for the Prediction of the Thermodynamic Properties of Mixtures Including Vapor-Liquid Equilibrium [PhD]. Moscow, ID: University of Idaho; 1996.
[41] Kunz O, Wagner W. The GERG-2008 wide-range equation of state for natural gases and other mixtures: an expansion of GERG-2004. J Chem Eng Data. 2012;57:3032–91.
[42] Span R. Multiparameter Equations of State. Berlin: Springer-Verlag; 2000.
[43] Jaubert J-N, Privat R. Relationship between the binary interaction parameters (k_{ij}) of the Peng-Robinson and those of the Soave-Redlich-Kwong equations of state: Application to the definition of the PR2SRK model. Fluid Phase Equilib. 2010;295:26-37.
[44] Vitu S, Privat R, Jaubert JN, Mutelet F. Predicting the phase equilibria of CO_2+ hydrocarbon systems with the PPR78 model (PR EOS and k_{ij} calculated through a group contribution method). J Supercrit Fluids. 2008;45:1-26.
[45] Jaubert JN, Mutelet F. VLE predictions with the Peng-Robinson equation of state and temperature dependent k_{ij} calculated through a group contribution method. Fluid Phase Equilib. 2004;224:285-304.

[46] Al Ghafri SZ, Maitland GC, Trusler JPM. Experimental and modeling study of the phase behavior of synthetic crude oil + CO_2. Fluid Phase Equilib. 2014;365:20-40.
[47] Dufal S, Papaioannou V, Sadeqzadeh M, Pogiatzis T, Chremos A, Adjiman CS, et al. Prediction of Thermodynamic Properties and Phase Behavior of Fluids and Mixtures with the SAFT-gamma Mie Group-Contribution Equation of State. J Chem Eng Data. 2014;59:3272-88.
[48] Papaioannou V, Lafitte T, Avendano C, Adjiman CS, Jackson G, Mueller EA, et al. Group contribution methodology based on the statistical associating fluid theory for heteronuclear molecules formed from Mie segments. J Chem Phys. 2014;140.
[49] Papaioannou V, Calado F, Lafitte T, Dufal S, Sadeqzadeh M, Jackson G, et al. Application of the SAFT-γ Mie group contribution equation of state to fluids of relevance to the oil and gas industry. Fluid Phase Equilib. 2016;416:104-19.
[50] Dufal S, Lafitte T, Haslam AJ, Galindo A, Clark GNI, Vega C, et al. The A in SAFT: developing the contribution of association to the Helmholtz free energy within a Wertheim TPT1 treatment of generic Mie fluids. Mol Phys. 2015;113:948-84.
[51] Fenghour A, Trusler JPM, Wakeham WA. Densities and bubble points of binary mixtures of carbon dioxide and n-heptane and ternary mixtures of n-butane, n-heptane and n-hexadecane. Fluid Phase Equilib. 2001;185:349-58.
[52] He Y, Lou Z, Ma S, Hu Y. Measuring phase equilibria of carbon dioxide + n-heptane system by stoichiometry. Huadong Ligong Daxue Xuebao. 1994;20:79-84.
[53] Mutelet F, Vitu S, Privat R, Jaubert JN. Solubility of CO_2 in branched alkanes in order to extend the PPR78 model (predictive 1978, Peng-Robinson EOS with temperature-dependent k_{ij} calculated through a group contribution method) to such systems. Fluid Phase Equilib. 2005;238:157-68.
[54] Inomata H, Arai K, Saito S. Measurement of vapor liquid equilibria at elevate temperatures and pressures using a flow type apparatus. Fluid Phase Equilib. 1986;29:225-32.
[55] Al Ghafri SZ, Forte E, Galindo A, Maitland GC, Trusler JM. Experimental and Modeling Study of the Phase Behavior of (Heptane+ Carbon Dioxide+ Water) Mixtures. J Chem Eng Data. 2015.
[56] Kalra H, Kubota H, Robinson DB, Ng H-J. Equilibrium phase properties of the carbon dioxide-n-heptane system. J Chem Eng Data. 1978;23:317-21.
[57] Medina-Bermudez M, Saavedra-Molina LA, Escamilla-Tiburcio W, Galicia-Luna LA, Elizalde-Solis O. (p, ρ, T) Behavior for the Binary Mixtures Carbon Dioxide plus Heptane and Carbon Dioxide plus Tridecane. J Chem Eng Data. 2013;58:1255-64.
[58] Rabe D. Experimental determination of dynamic viscosity and density of binary liquid mixtures of n-heptane with CO_2, CH_4, C_2H_6, C_3H_8 and of toluene with CH_4 and C_3H_8: TU Berlin; 1981.
[59] Efika EC, Hoballah R, Li X, May EF, Nania M, Sanchez-Vicente Y, et al. Saturated phase densities of (CO_2 + H_2O) at temperatures from (293 to 450) K and pressures up to 64 MPa. J Chem Thermodyn. 2016;93:347-59.
[60] Al Ghafri S, Maitland GC, Trusler JPM. Densities of Aqueous $MgCl_2$(aq), $CaCl_2$(aq), KI(aq), NaCl(aq), KCl(aq), $AlCl_3$(aq), and (0.964 NaCl+00136 KCl)(aq) at Temperatures Between (283 and 472) K, Pressures up to 68.5 MPa, and Molalities up to 6 mol.kg^{-1}. J Chem Eng Data. 2012;57:1288-304.
[61] Lin CW, Trusler JPM. Speed of Sound in (Carbon Dioxide + Propane) and Derived Sound Speed of Pure Carbon Dioxide at Temperatures between (248 and 373) K and at Pressures up to 200 MPa. J Chem Eng Data. 2014;59:4099-109.
[62] May EF, Tay WJ, Nania M, Aleji A, Al-Ghafri S, Trusler JPM. Physical apparatus parameters and model for vibrating tube densimeters at pressures to 140 MPa and temperatures to 473 K. Rev Sci Instrum. 2014;85:095111.
[63] May EF, Tay WJ, Nania M, Aleji A, Al-Ghafri S, Trusler JPM. Erratum: "Physical apparatus parameters and model for vibrating tube densimeters at pressures to 140 MPa and temperatures to 473 K" [Rev. Sci. Instrum. 85, 095111, (2014)]. Rev Sci Instrum. 2015;86:049902.

[64] Lemmon EW, Huber ML, McLinden MO. NIST standard reference database 23: Reference fluid thermodynamic and transport properties - REFPROP, Version 9.1. Gaithersburg: National Institute of Standards and Technology 2013.
[65] BIPM I, IFCC, ILAC, ISO, IUPAC, IUPAP and OIML. ISO/IEC Guide 98-3:2008, Uncertainty of measurement - Part 3: Guide to the expression of uncertainty in measurement (GUM:1995). 2008.
[66] Medina-Bermudez M, Saavedra-Molina LA, Escamilla-Tiburcio W, Galicia-Luna LA, Elizalde-Solis O. (p, rho, T) Behavior for the Binary Mixtures Carbon Dioxide plus Heptane and Carbon Dioxide plus Tridecane. J Chem Eng Data. 2013;58:1255-64.
[67] Lay EN. Measurement and Correlation of Bubble Point Pressure in (CO_2 + C_6H_6), (CO_2 + $CH_3C_6H_5$), (CO_2 + C_6H_{14}), and (CO_2 + C_7H_{16}) at Temperatures from (293.15 to 313.15) K. J Chem Eng Data. 2010;55:223-7.
[68] Gurdial GS, Foster NR, Yun SLJ, Tilly KD. Phase-behavior of supercritical fluid entrainer systems. ACS Symp Ser. 1993;514:34-45.
[69] Choi EJ, Yeo SD. Critical properties for carbon dioxide plus n-alkane mixtures using a variable-volume view cell. J Chem Eng Data. 1998;43:714-6.
[70] Sun YJ, Li YF, Zhou JG, Zhu RJ, Tian YL. Experimental determination and calculation of the critical curves for the binary systems of CO_2 containing ketone, alkane, ester and alcohol, respectively. Fluid Phase Equilib. 2011;307:72-7.
[71] Juntarachat N, Bello S, Privat R, Jaubert JN. Validation of a new apparatus using the dynamic method for determining the critical properties of binary mixtures containing CO_2 and a n-alkane. Fluid Phase Equilib. 2012;325:66-70.
[72] van Konynenburg PH, Scott RL. Critical lines and phase-equilibria in binary van der Waals mixtures. Philos Trans R Soc London, Ser A. 1980;298:495-540.
[73] Heidemann RA, Khalil AM. The calculation of critical-points. AlChE J. 1980;26:769-79.
[74] Kalra H, Kubota H, Robinson DB, Ng HJ. Equilibrium phase properties of carbon dioxide normal-heptane system. J Chem Eng Data. 1978;23:317-21.
[75] Binney JJ, Dowrick NJ, Fisher AJ, Newman MEJ. The theory of critical phenomena: an introduction to the renormalization group. Oxford: Clarendon press; 1992.
[76] Aspen Technology. Aspen Properties. v8.4 ed2013.
[77] PSE Ltd. gPROMS V.4.2.0. 2014. http://www.psenterprise.com.

Supplementary Materials

Thermodynamics of Carbon Dioxide-Hydrocarbon Systems

Yolanda Sanchez-Vicente[1], Weparn J Tay[1], Saif Z Al Ghafri[1,2], J P Martin Trusler[1]

[1]Qatar Carbonates and Carbon Storage Research Centre (QCCSRC), Department of Chemical Engineering, Imperial College London, South Kensington Campus, London SW7 2AZ, United Kingdom

[2]Centre for Energy, School of Mechanical & Chemical Engineering, The University of Western Australia, Crawley, WA 6009, Australia,

Contents

List of Tables

List of Figures

1. Reproducibility of the saturated phase densities

The reproducibility of the saturated phase densities was tested by re-measuring the dataset at 323 K on different days. The results are shown in Figure S1. On the basis of these experiments, we estimated that the reproducibility is ±1 kg·m $^{-3}$.

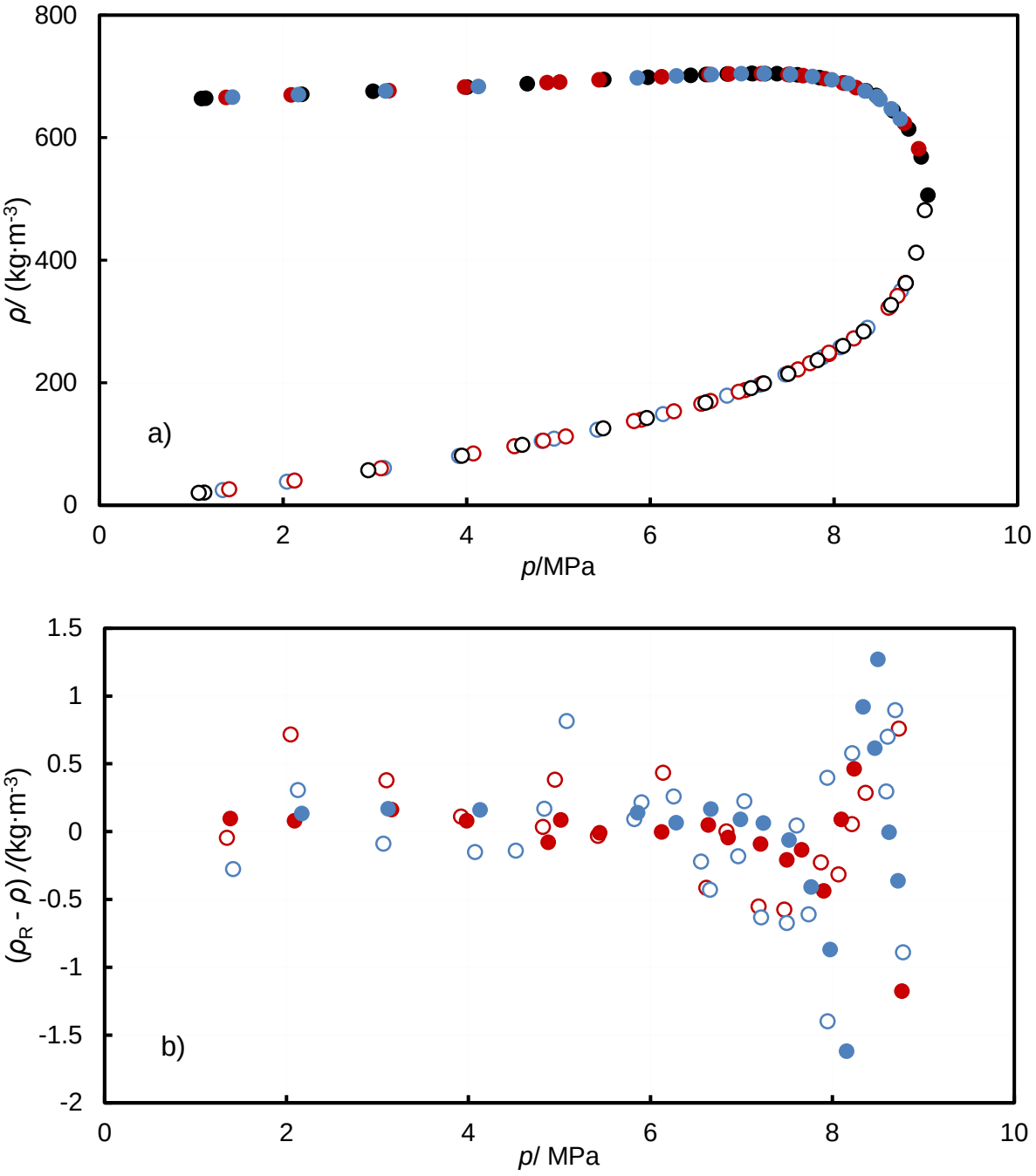

Figure S1: Saturated phase densities for CO2 + n-heptane mixture at 323 K measured on different days: ●, 19-May-2015, ●, 14-Jul-2015 and ●, 21-Jul-2015. b) Differences between the saturated phase densities measured on 19-May-2015, ρ_R, and the saturated phase densities measured on: ● 14-Jul-2015 or ● 21-Jul-2015. Empty symbols are dew-point densities and full symbols bubble-point densities.

2. Comparison with literature data

2.1 Compressed-fluid densities

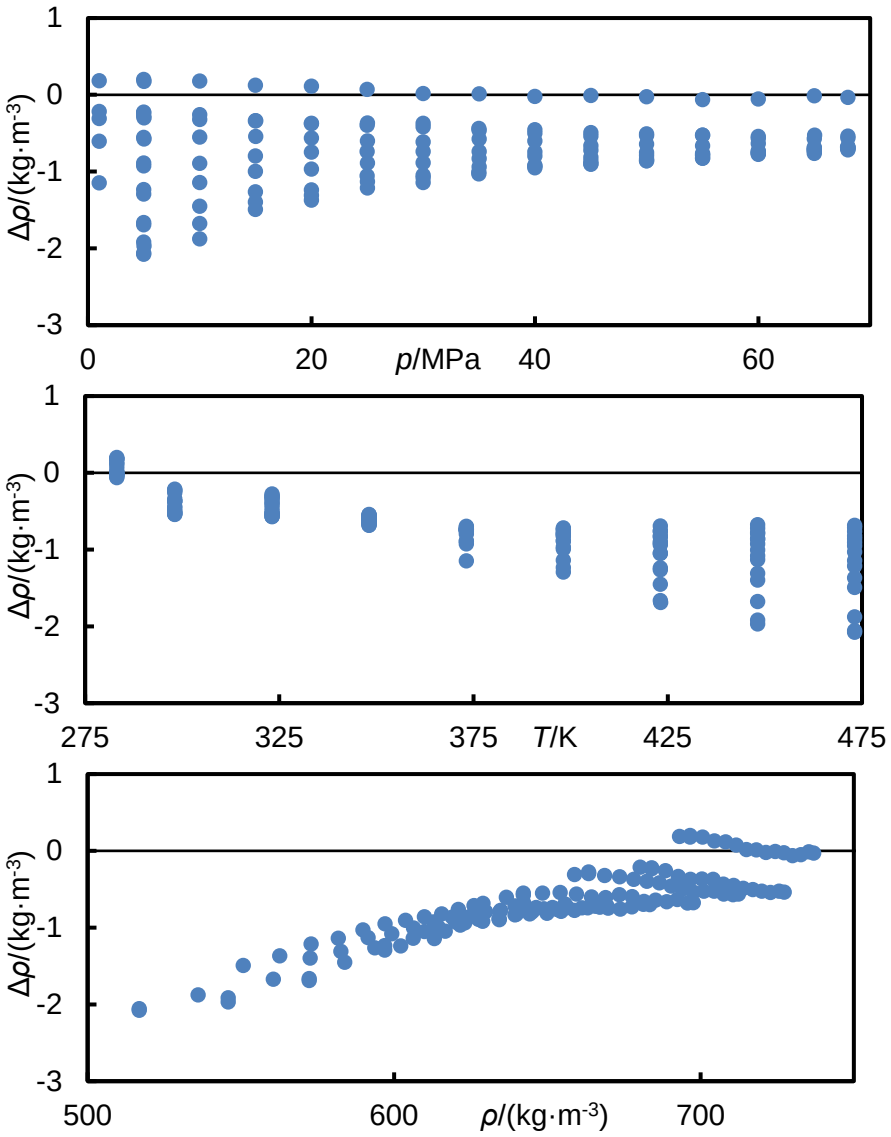

Figure S2: Deviations $\Delta\rho = \rho(\text{exp}) - \rho(\text{EoS})$ between experimental densities ρ(exp) of pure heptane and values ρ(EoS) calculated from the equation of state of Span and Wagner [1] plotted as functions of pressure p, temperature T and density ρ.

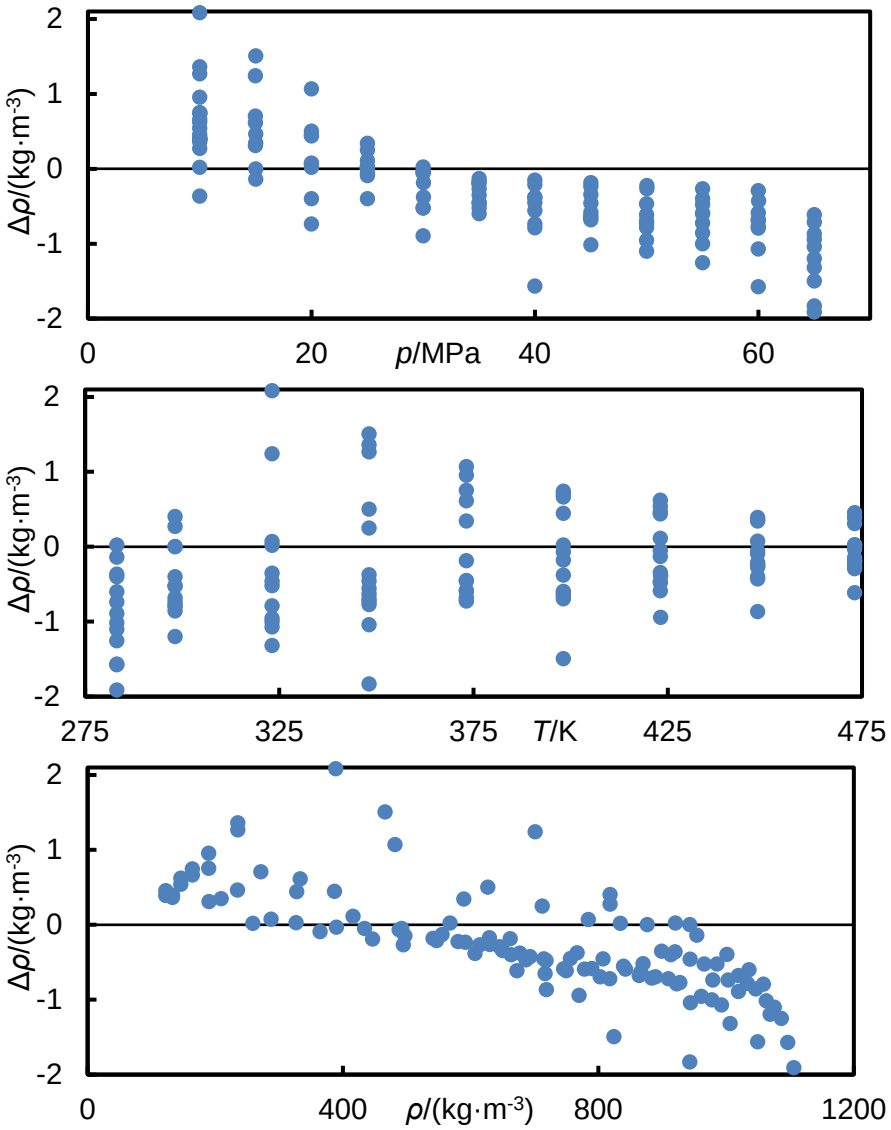

Figure S3: Deviations $\Delta\rho = \rho(\text{exp}) - \rho(\text{EoS})$ between experimental densities ρ(exp) of pure CO_2 and values ρ(EoS) calculated from the equation of state of Span and Wagner [2] plotted as functions of pressure p, temperature T and density ρ.

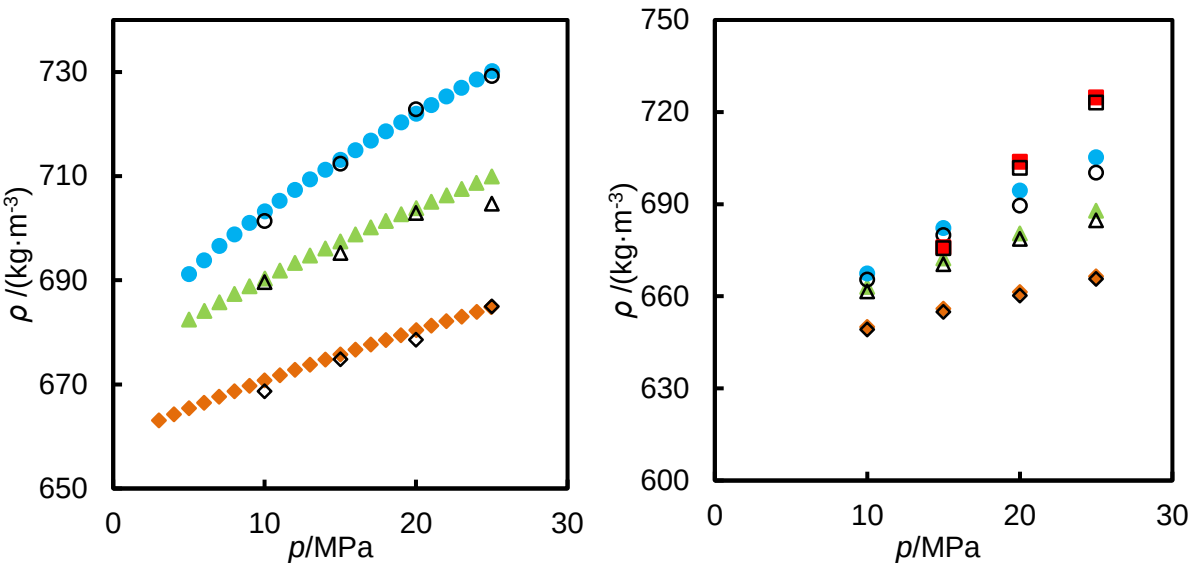

Figure S4: Comparison of compressed liquid densities at a) 323 K and b) 348 K between our work and literature data. Unfilled symbols represent data interpolated from our measurements and filled symbols represent the work by Medina-Bermudez et al [3] at CO_2 mole fractions of: ◆, 0.02, ▲, 0.31, ●, 0.51, ■, 0.75.

2.2 Saturated-phase densities

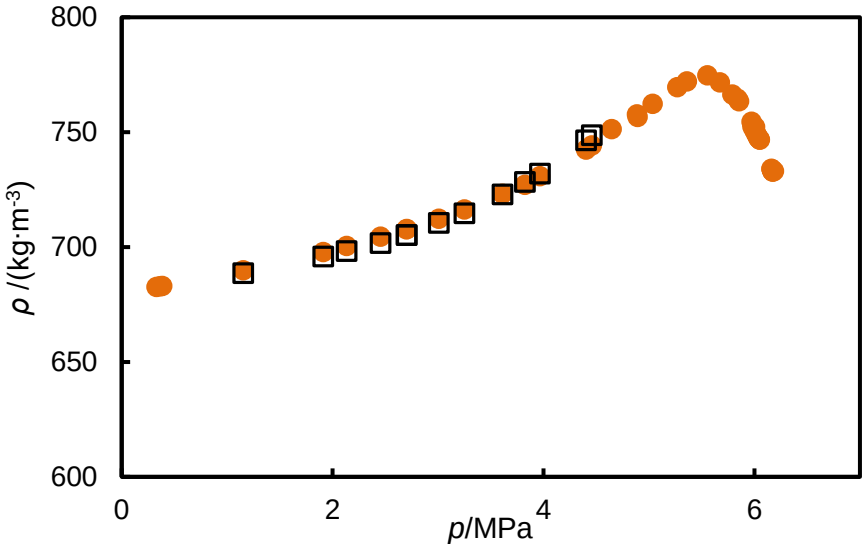

Figure S5: Experimental saturated densities for the CO_2 + n-heptane system as a function of pressure at T = 298 K in this work (●) and interpolated densities from Rabe's data (□)[4].

3. Experimental data and derived properties

3.1 Compressed-fluid densities and derived compressibilities and expansivities

Table S1: Experimental compressed-fluid densities ρ for the (CO_2 + n-heptane) system at temperatures T and pressures p, where x denotes the mole fraction of CO_2 and $u(\rho)$ denotes the standard uncertainty of ρ.

T / K	p / MPa	ρ / (kg·m^{-3})	$u(\rho)$ /(kg·m^{-3})	T / K	p / MPa	ρ / kgm^{-3}	$u(\rho)$ /(kg·m^{-3})
			x = 0.0000				
283.15	1.01	693.19	0.33	348.15	35.01	673.53	0.33
283.16	5.00	696.64	0.33	348.15	40.01	677.67	0.33
283.16	10.01	700.72	0.33	348.15	45.00	681.57	0.33
283.16	15.01	704.55	0.33	348.15	50.00	685.37	0.33
283.16	20.01	708.23	0.33	348.15	55.00	688.97	0.33
283.16	25.01	711.70	0.33	348.15	60.01	692.47	0.33
283.16	30.02	715.03	0.33	348.15	65.02	695.77	0.33
283.16	35.01	718.25	0.33	348.15	68.00	697.70	0.33
283.16	40.00	721.33	0.33	373.15	1.00	613.15	0.34
283.16	45.01	724.35	0.33	373.15	5.01	620.08	0.34
283.16	50.01	727.23	0.33	373.15	10.00	627.62	0.34
283.16	55.01	730.00	0.33	373.15	15.00	634.48	0.34
283.16	60.00	732.72	0.33	373.15	20.01	640.70	0.34
283.16	65.01	735.39	0.33	373.15	25.00	646.38	0.34
283.16	68.01	736.91	0.33	373.15	30.01	651.67	0.33
298.14	1.01	680.29	0.33	373.15	35.01	656.62	0.33
298.14	5.01	684.08	0.33	373.15	40.02	661.28	0.33
298.14	10.01	688.54	0.33	373.15	45.01	665.69	0.33
298.14	15.02	692.71	0.33	373.15	50.02	669.85	0.33
298.14	20.01	696.67	0.33	373.15	55.02	673.82	0.33
298.14	25.02	700.48	0.33	373.15	60.01	677.64	0.33
298.14	30.01	704.10	0.33	373.15	65.01	681.31	0.33
298.14	35.00	707.51	0.33	373.15	68.01	683.43	0.33
298.14	40.00	710.83	0.33	398.15	5.01	596.93	0.34
298.14	45.01	713.99	0.33	398.15	10.00	606.22	0.34
298.14	50.00	717.05	0.33	398.15	15.01	614.40	0.34
298.14	55.01	720.02	0.33	398.15	20.00	621.60	0.34
298.14	60.00	722.88	0.33	398.16	25.02	628.23	0.34
298.14	65.03	725.69	0.33	398.15	30.00	634.22	0.34
298.14	68.02	727.30	0.33	398.16	35.03	639.86	0.33
323.16	1.01	658.94	0.34	398.16	40.01	645.08	0.33
323.15	5.00	663.50	0.34	398.15	45.01	649.95	0.33
323.15	10.03	668.76	0.33	398.16	50.01	654.57	0.33
323.15	15.00	673.63	0.33	398.15	55.01	658.95	0.33
323.15	20.01	678.21	0.33	398.15	60.01	663.14	0.33
323.15	25.01	682.53	0.33	398.15	65.02	667.13	0.33
323.15	30.00	686.61	0.33	398.16	68.01	669.43	0.33
323.15	35.02	690.49	0.33	423.16	5.01	572.32	0.35
323.15	40.00	694.17	0.33	423.15	10.00	583.92	0.35
323.15	45.01	697.70	0.33	423.15	15.01	593.74	0.34
323.15	50.01	701.13	0.33	423.15	20.01	602.20	0.34
323.15	55.00	704.42	0.33	423.15	25.01	609.90	0.34
323.15	60.01	707.55	0.33	423.15	30.01	616.72	0.34
323.15	65.00	710.58	0.33	423.15	35.02	623.11	0.34
323.15	68.01	712.38	0.33	423.15	40.01	628.92	0.33
348.15	1.02	636.71	0.34	423.15	45.01	634.35	0.33
348.15	5.02	642.21	0.34	423.15	50.01	639.48	0.33
348.15	10.01	648.47	0.34	423.15	55.00	644.27	0.33
348.15	15.02	654.24	0.34	423.15	60.00	648.86	0.33

T / K	p / MPa	ρ / (kg·m^{-3})	$u(\rho)$ /(kg·m^{-3})	T / K	p / MPa	ρ / kgm^{-3}	$u(\rho)$ /(kg·m^{-3})
348.15	20.01	659.52	0.33	423.15	65.01	653.17	0.33
348.15	25.01	664.45	0.33	423.15	68.02	655.74	0.33
348.15	30.00	669.09	0.33	473.15	5.01	516.85	0.38
448.16	5.02	545.93	0.36	473.15	10.00	536.05	0.36
448.16	10.01	560.67	0.35	473.15	15.01	550.84	0.35
448.16	15.01	572.63	0.35	473.15	20.01	562.72	0.34
448.16	20.00	582.62	0.34	473.15	25.02	572.94	0.34
448.16	25.02	591.51	0.34	473.15	30.00	581.82	0.34
448.16	30.00	599.30	0.34	473.15	35.00	589.84	0.34
448.16	35.00	606.42	0.34	473.15	40.01	597.10	0.34
448.16	40.00	612.95	0.33	473.15	45.01	603.74	0.33
448.16	45.01	619.01	0.33	473.15	50.01	609.89	0.33
448.16	50.01	624.58	0.33	473.15	55.01	615.62	0.33
448.16	55.01	629.87	0.33	473.15	60.00	621.01	0.33
448.16	60.01	634.82	0.33	473.15	65.01	626.11	0.33
448.16	65.00	639.52	0.33	473.15	68.01	629.03	0.33
448.16	68.01	642.27	0.33				
			x = 0.2053				
283.15	10.01	717.20	0.33	373.15	45.00	678.94	0.33
283.15	15.01	721.73	0.33	373.16	50.00	683.93	0.33
283.15	20.00	726.01	0.33	373.16	55.01	688.58	0.33
283.16	25.00	730.09	0.33	373.16	60.00	692.99	0.33
283.15	30.00	733.97	0.33	373.15	65.01	697.25	0.33
283.15	35.00	737.65	0.33	373.15	68.01	699.75	0.33
283.15	40.01	741.22	0.33	398.16	10.00	605.54	0.34
283.16	45.00	744.65	0.33	398.15	15.01	616.62	0.34
283.15	50.01	747.92	0.33	398.15	20.01	626.01	0.34
283.15	55.01	751.09	0.33	398.16	25.00	634.43	0.34
283.16	60.01	754.16	0.33	398.16	30.01	641.92	0.33
283.16	65.02	757.13	0.33	398.15	35.01	648.79	0.33
283.16	68.01	759.01	0.33	398.16	40.01	655.11	0.33
298.16	10.01	703.68	0.33	398.15	45.01	661.00	0.33
298.16	15.00	708.79	0.33	398.15	50.01	666.50	0.33
298.16	20.00	713.50	0.33	398.15	55.01	671.66	0.33
298.16	25.00	717.97	0.33	398.15	60.00	676.62	0.33
298.16	30.00	722.18	0.33	398.15	65.01	681.24	0.33
298.16	35.00	726.19	0.33	398.15	68.01	684.02	0.33
298.16	40.02	730.05	0.33	423.16	10.00	577.56	0.35
298.16	45.01	733.72	0.33	423.15	15.01	591.51	0.35
298.16	50.00	737.23	0.33	423.15	20.00	602.91	0.34
298.16	55.01	740.59	0.33	423.15	25.00	612.82	0.34
298.16	60.01	743.90	0.33	423.15	30.01	621.57	0.34
298.16	65.01	747.06	0.33	423.15	35.00	629.41	0.33
298.16	68.00	748.97	0.33	423.15	40.00	636.56	0.33
323.16	10.01	680.60	0.33	423.15	45.01	643.13	0.33
323.15	15.02	686.66	0.33	423.15	50.00	649.22	0.33
323.16	20.01	692.18	0.33	423.15	55.01	654.97	0.33
323.15	25.01	697.40	0.33	423.15	60.00	660.34	0.33
323.15	30.01	702.28	0.33	423.15	65.00	665.41	0.33
323.15	35.01	706.85	0.33	423.15	68.02	668.41	0.33
323.15	40.01	711.18	0.33	448.16	10.02	547.50	0.37
323.15	45.00	715.36	0.33	448.15	15.01	565.29	0.35
323.15	50.02	719.28	0.33	448.16	20.00	579.20	0.35
323.15	55.00	723.07	0.33	448.15	25.00	590.96	0.34
323.15	60.01	726.69	0.33	448.16	30.01	601.00	0.34
323.15	65.00	730.17	0.33	448.15	35.01	610.02	0.34

T / K	p / MPa	ρ / (kg·m^{-3})	$u(\rho)$ /(kg·m^{-3})	T / K	p / MPa	ρ / kgm^{-3}	$u(\rho)$ /(kg·m^{-3})
323.15	68.01	732.32	0.33	448.16	40.01	618.04	0.33
348.15	10.00	656.67	0.34	448.15	45.01	625.38	0.33
348.15	15.01	664.02	0.33	448.16	50.01	632.15	0.33
348.15	20.01	670.58	0.33	448.16	55.00	638.43	0.33
348.15	25.02	676.69	0.33	448.16	60.01	644.28	0.33
348.15	30.00	682.27	0.33	448.16	65.01	649.84	0.33
348.15	35.00	687.50	0.33	448.16	68.00	653.01	0.33
348.15	40.01	692.43	0.33	473.15	10.01	514.54	0.39
348.15	45.01	697.07	0.33	473.15	15.01	537.86	0.36
348.15	50.00	701.51	0.33	473.15	20.00	554.82	0.35
348.15	55.01	705.70	0.33	473.15	25.00	568.74	0.35
348.15	60.00	709.70	0.33	473.15	30.01	580.37	0.34
348.15	65.02	713.59	0.33	473.15	35.00	590.53	0.34
348.15	68.00	715.92	0.33	473.15	40.00	599.59	0.34
373.16	10.00	631.77	0.34	473.15	45.01	607.79	0.33
373.15	15.02	640.72	0.34	473.15	50.01	615.22	0.33
373.16	20.01	648.56	0.34	473.15	55.01	622.13	0.33
373.15	25.01	655.66	0.33	473.15	60.00	628.51	0.33
373.16	30.01	662.18	0.33	473.15	65.01	634.50	0.33
373.15	35.01	668.16	0.33	473.15	68.01	638.08	0.33
373.16	40.00	673.74	0.33				
			x = 0.3989				
283.15	10.00	738.68	0.33	373.15	45.01	695.38	0.33
283.15	15.01	744.36	0.33	373.15	50.01	701.46	0.33
283.16	20.01	749.59	0.33	373.15	55.00	707.15	0.33
283.16	25.01	754.57	0.33	373.15	60.01	712.53	0.33
283.16	30.01	759.25	0.33	373.15	65.00	717.63	0.33
283.16	35.01	763.73	0.33	373.15	68.01	720.62	0.33
283.16	40.01	767.90	0.33	398.15	10.00	596.61	0.35
283.15	45.01	771.98	0.33	398.15	15.00	614.05	0.34
283.16	50.01	775.85	0.33	398.15	20.01	627.71	0.34
283.16	55.00	779.58	0.33	398.15	25.00	639.44	0.34
283.16	60.00	783.20	0.33	398.15	30.01	649.51	0.33
283.16	65.01	786.67	0.33	398.15	35.01	659.00	0.33
283.16	68.01	788.74	0.33	398.15	40.01	666.64	0.33
298.15	10.00	722.79	0.33	398.15	45.02	674.09	0.33
298.15	15.01	729.25	0.33	398.15	50.00	680.91	0.33
298.15	20.01	735.11	0.33	398.15	55.01	687.33	0.33
298.15	25.01	740.67	0.33	398.15	60.00	693.27	0.33
298.15	30.00	745.83	0.33	398.15	65.01	698.96	0.33
298.15	35.01	750.74	0.33	398.15	68.01	702.18	0.33
298.15	40.01	755.31	0.33	423.15	10.00	556.99	0.36
298.15	45.01	759.72	0.33	423.15	15.01	581.00	0.35
298.15	50.01	763.92	0.33	423.15	20.01	598.43	0.34
298.15	55.02	767.93	0.33	423.15	25.01	612.68	0.34
298.15	60.01	771.79	0.33	423.15	30.01	624.62	0.34
298.15	65.00	775.50	0.33	423.15	35.00	635.11	0.33
298.15	68.01	777.66	0.33	423.15	40.01	644.39	0.33
323.15	10.00	694.35	0.33	423.15	45.02	652.86	0.33
323.15	15.00	702.35	0.33	423.15	50.00	660.55	0.33
323.15	20.00	709.45	0.33	423.15	55.01	667.65	0.33
323.15	25.00	716.06	0.33	423.15	60.00	674.23	0.33
323.15	30.00	722.13	0.33	423.15	65.00	680.41	0.33
323.15	35.00	727.85	0.33	423.15	68.00	684.00	0.33
323.15	40.01	733.17	0.33	448.15	10.00	511.21	0.37
323.15	45.01	738.19	0.33	448.15	15.00	545.61	0.36

T / K	p / MPa	ρ / (kg·m^{-3})	$u(\rho)$ /(kg·m^{-3})	T / K	p / MPa	ρ / kgm^{-3}	$u(\rho)$ /(kg·m^{-3})
323.15	50.01	742.96	0.33	448.15	20.01	567.98	0.35
323.15	55.01	747.48	0.33	448.15	25.01	585.49	0.34
323.15	60.00	751.81	0.33	448.16	30.01	599.56	0.34
323.15	65.01	755.93	0.33	448.15	35.01	611.70	0.34
323.15	68.01	758.33	0.33	448.16	40.00	622.27	0.33
348.16	10.00	664.24	0.33	448.15	45.01	631.83	0.33
348.15	15.01	674.44	0.33	448.15	50.01	640.37	0.33
348.15	20.01	683.12	0.33	448.15	55.00	648.25	0.33
348.15	25.01	691.11	0.33	448.15	60.01	655.54	0.33
348.15	30.01	698.22	0.33	448.15	65.01	662.31	0.33
348.15	35.01	704.88	0.33	448.15	68.00	666.20	0.33
348.15	40.00	711.00	0.33	473.15	10.01	458.14	0.40
348.15	45.01	716.77	0.33	473.15	15.00	508.00	0.37
348.15	50.02	722.15	0.33	473.16	20.00	536.53	0.35
348.15	55.01	727.23	0.33	473.15	25.00	557.82	0.35
348.15	60.01	732.01	0.33	473.15	30.00	574.36	0.34
348.15	65.00	736.65	0.33	473.15	35.01	588.38	0.34
348.15	68.01	739.32	0.33	473.15	40.01	600.35	0.34
373.15	10.00	631.96	0.34	473.15	45.00	610.94	0.33
373.15	15.01	645.07	0.34	473.15	50.02	620.48	0.33
373.15	20.01	655.90	0.33	473.15	55.01	629.16	0.33
373.15	25.00	665.54	0.33	473.15	60.00	637.12	0.33
373.15	30.01	674.02	0.33	473.15	65.00	644.50	0.33
373.15	35.00	681.76	0.33	473.15	68.01	648.79	0.33
373.15	40.01	688.82	0.33				
				x = 0.6037			
283.16	10.02	771.71	0.33	373.15	35.01	698.27	0.33
283.16	15.01	779.70	0.33	373.15	40.01	708.38	0.33
283.16	20.01	786.84	0.33	373.15	45.00	717.70	0.33
283.16	25.01	793.83	0.33	373.15	50.01	726.08	0.33
283.16	30.00	799.82	0.33	373.15	55.02	733.88	0.33
283.16	35.01	805.91	0.33	373.15	60.01	741.09	0.33
283.16	40.00	811.29	0.33	373.16	65.01	747.86	0.33
283.16	45.01	816.72	0.33	373.15	68.00	751.74	0.33
283.16	50.01	821.50	0.33	398.16	15.00	591.88	0.34
283.16	55.01	826.43	0.33	398.16	20.01	617.66	0.34
283.16	60.01	830.80	0.33	398.16	25.01	637.30	0.34
283.16	65.00	835.18	0.33	398.15	30.00	653.40	0.33
283.16	68.01	837.90	0.33	398.15	35.01	667.33	0.33
298.16	10.00	749.37	0.33	398.15	40.01	679.36	0.33
298.16	15.01	758.88	0.33	398.16	45.01	690.17	0.33
298.16	20.01	767.29	0.33	398.16	50.01	699.97	0.33
298.16	25.01	775.16	0.33	398.15	55.01	708.93	0.33
298.16	30.00	782.12	0.33	398.16	60.00	717.12	0.33
298.16	35.00	788.74	0.33	398.15	65.00	724.72	0.33
298.16	40.01	794.80	0.33	398.15	68.01	729.16	0.33
298.16	45.01	800.66	0.33	423.15	15.01	536.49	0.35
298.16	50.00	806.02	0.33	423.16	20.01	573.98	0.34
298.16	55.00	811.24	0.33	423.16	25.01	600.03	0.34
298.16	60.01	816.14	0.33	423.16	30.01	619.93	0.34
298.16	65.01	820.85	0.33	423.16	35.01	636.42	0.33
298.16	68.01	823.57	0.33	423.15	40.01	650.30	0.33
323.15	10.00	709.06	0.33	423.15	45.02	662.83	0.33
323.15	15.01	722.07	0.33	423.16	50.00	673.62	0.33
323.15	20.00	732.65	0.33	423.15	55.00	683.84	0.33
323.15	25.01	742.54	0.33	423.16	60.01	692.84	0.33

T / K	p / MPa	ρ / (kg·m^{-3})	$u(\rho)$ /(kg·m^{-3})	T / K	p / MPa	ρ / kgm^{-3}	$u(\rho)$ /(kg·m^{-3})
323.15	30.00	751.00	0.33	423.16	65.02	701.36	0.33
323.15	35.00	759.00	0.33	423.16	68.01	706.16	0.33
323.15	40.01	766.22	0.33	448.15	15.01	477.35	0.00
323.15	45.02	773.08	0.33	448.15	20.01	529.65	0.35
323.15	50.01	779.30	0.33	448.15	25.01	562.29	0.34
323.15	55.01	785.32	0.33	448.15	30.01	586.36	0.34
323.15	60.01	790.89	0.33	448.15	35.01	605.75	0.34
323.15	65.02	796.21	0.33	448.16	40.01	621.84	0.33
323.15	68.01	799.30	0.33	448.15	45.01	635.91	0.33
348.15	10.01	663.75	0.33	448.16	50.00	648.17	0.33
348.15	15.00	681.92	0.33	448.15	55.02	659.42	0.33
348.15	20.00	696.22	0.33	448.15	60.01	669.46	0.33
348.15	25.01	708.65	0.33	448.15	65.01	678.78	0.33
348.15	30.00	719.21	0.33	448.15	68.01	684.17	0.33
348.15	35.01	728.84	0.33	473.15	15.00	421.61	0.37
348.15	40.00	737.38	0.33	473.15	20.01	486.09	0.35
348.15	45.00	745.39	0.33	473.15	25.01	524.79	0.35
348.15	50.01	752.59	0.33	473.15	30.01	553.34	0.34
348.15	55.01	759.46	0.33	473.15	35.01	575.31	0.34
348.15	60.00	765.83	0.33	473.15	40.00	593.62	0.34
348.15	65.01	771.85	0.33	473.15	45.02	609.36	0.33
348.15	68.01	775.32	0.33	473.15	50.00	623.06	0.33
373.15	10.01	610.44	0.34	473.15	55.01	635.47	0.33
373.15	15.02	638.28	0.34	473.15	60.01	646.54	0.33
373.15	20.01	657.56	0.33	473.15	65.01	656.80	0.33
373.15	25.01	673.57	0.33	473.15	68.01	662.44	0.33
373.15	30.01	686.70	0.33				
			x = 0.8001				
283.16	10.02	823.37	0.34	373.16	40.01	734.45	0.35
283.15	15.00	836.52	0.34	373.15	45.01	749.78	0.34
283.16	20.00	847.31	0.34	373.16	50.01	762.71	0.34
283.16	25.01	857.89	0.33	373.15	55.00	775.01	0.34
283.16	30.00	866.87	0.33	373.15	60.01	785.73	0.33
283.16	35.01	875.59	0.33	373.15	65.01	795.86	0.33
283.16	40.01	883.25	0.33	373.15	68.01	801.53	0.33
283.16	45.01	890.86	0.33	398.15	15.00	485.04	0.65
283.16	50.01	897.57	0.33	398.15	20.00	565.87	0.49
283.16	55.01	904.27	0.33	398.15	25.01	612.72	0.42
283.16	60.01	910.17	0.33	398.16	30.01	644.79	0.39
283.16	65.00	916.06	0.33	398.15	35.01	671.03	0.37
283.16	68.01	919.40	0.33	398.16	40.00	691.40	0.36
298.16	10.01	787.40	0.35	398.15	45.01	709.88	0.35
298.15	15.01	805.05	0.35	398.15	50.01	725.11	0.34
298.16	20.01	818.49	0.34	398.15	55.00	739.42	0.34
298.15	25.00	831.29	0.34	398.15	60.01	751.68	0.34
298.16	30.00	841.99	0.33	398.15	65.01	763.20	0.33
298.15	35.01	852.33	0.33	398.15	68.00	769.86	0.33
298.16	40.00	860.97	0.33	423.15	15.01	405.23	0.66
298.15	45.01	869.76	0.33	423.16	20.01	500.26	0.53
298.16	50.01	877.25	0.33	423.15	25.01	556.15	0.45
298.15	55.01	884.73	0.33	423.16	30.00	595.07	0.41
298.16	60.00	891.36	0.33	423.15	35.01	626.55	0.38
298.16	65.01	897.94	0.34	423.15	40.00	650.30	0.37
298.16	68.01	901.66	0.34	423.15	45.01	671.89	0.36
323.15	10.01	714.71	0.40	423.15	50.00	689.19	0.35
323.15	15.01	743.80	0.37	423.15	55.01	705.53	0.34

T / K	p / MPa	ρ / (kg·m^{-3})	$u(\rho)$ /(kg·m^{-3})	T / K	p / MPa	ρ / kgm^{-3}	$u(\rho)$ /(kg·m^{-3})
323.15	20.01	763.84	0.35	423.16	60.00	719.20	0.34
323.15	25.01	781.32	0.35	423.15	65.00	732.11	0.34
323.16	30.00	795.12	0.34	423.15	68.02	739.30	0.34
323.15	35.00	808.42	0.34	448.15	15.01	345.50	0.64
323.15	40.00	819.39	0.33	448.15	20.01	442.28	0.55
323.15	45.01	829.96	0.33	448.15	25.00	503.19	0.48
323.15	50.00	839.04	0.33	448.15	30.00	548.42	0.43
323.15	55.01	847.82	0.33	448.15	35.01	583.15	0.40
323.15	60.01	855.85	0.33	448.15	40.01	610.78	0.38
323.15	65.00	863.33	0.34	448.15	45.01	634.57	0.36
348.15	15.01	671.20	0.42	448.16	50.01	654.29	0.36
348.16	20.00	703.32	0.38	448.15	55.00	672.19	0.35
348.15	25.00	728.14	0.36	448.15	60.01	687.55	0.34
348.16	30.01	746.27	0.35	448.16	65.00	701.56	0.34
348.15	35.01	763.24	0.34	448.16	68.02	709.71	0.34
348.16	40.01	776.79	0.34	473.15	15.01	301.93	0.61
348.15	45.01	789.62	0.34	473.16	20.01	393.82	0.60
348.15	50.01	800.66	0.33	473.15	30.01	505.33	0.47
348.15	55.01	811.26	0.33	473.15	35.02	542.77	0.43
348.15	60.01	820.42	0.33	473.15	40.01	573.06	0.40
348.15	65.01	829.23	0.33	473.15	45.00	599.00	0.38
348.15	68.00	834.35	0.33	473.16	50.01	620.62	0.37
373.15	15.01	584.27	0.53	473.15	55.01	640.02	0.36
373.16	20.01	638.35	0.43	473.15	60.01	656.80	0.35
373.15	25.01	671.56	0.39	473.15	65.00	672.05	0.35
373.16	30.00	695.82	0.37	473.15	68.01	680.33	0.35
373.15	35.02	717.21	0.36				
			x = 1.0000				
283.15	10.01	920.13	0.52	373.15	40.01	756.29	0.48
283.15	15.01	954.10	0.49	373.15	45.02	789.89	0.47
283.15	20.00	979.44	0.48	373.15	50.01	818.07	0.46
283.15	25.01	1001.30	0.47	373.15	55.01	842.73	0.45
283.15	30.02	1019.31	0.46	373.15	60.00	864.24	0.45
283.15	35.02	1035.90	0.46	373.16	65.01	883.60	0.44
283.15	40.01	1049.44	0.46	398.15	10.03	164.19	0.65
283.15	45.01	1063.28	0.45	398.15	15.01	271.55	0.68
283.15	50.00	1075.40	0.45	398.15	20.02	386.59	0.67
283.15	55.00	1086.55	0.45	398.15	25.01	487.98	0.62
283.15	60.00	1096.83	0.45	398.15	30.00	567.81	0.57
283.15	65.01	1106.39	0.45	398.15	35.02	629.20	0.52
298.16	10.03	818.47	0.63	398.15	40.00	677.26	0.50
298.15	15.01	876.55	0.53	398.15	45.00	716.53	0.48
298.16	20.00	913.82	0.49	398.15	50.01	749.77	0.46
298.15	25.03	943.12	0.47	398.15	55.01	778.27	0.46
298.16	30.01	965.99	0.46	398.15	60.00	803.03	0.45
298.16	35.01	986.09	0.46	398.15	65.00	824.37	0.45
298.16	40.00	1003.46	0.45	423.15	10.02	146.37	0.61
298.16	45.03	1019.32	0.45	423.15	15.02	234.66	0.63
298.16	50.00	1033.41	0.45	423.15	20.02	327.81	0.63
298.16	55.01	1046.44	0.45	423.15	25.01	415.82	0.60
298.16	60.01	1058.51	0.45	423.15	30.01	492.12	0.56
298.16	65.01	1069.30	0.45	423.15	35.01	555.19	0.53
323.15	10.02	388.56	1.48	423.15	40.01	606.76	0.50
323.15	15.00	701.06	0.72	423.15	45.02	650.15	0.48
323.15	20.00	784.40	0.56	423.15	50.00	686.47	0.47
323.15	25.00	834.25	0.51	423.15	55.00	718.06	0.46

T / K	p / MPa	ρ / (kg·m^{-3})	$u(\rho)$ /(kg·m^{-3})	T / K	p / MPa	ρ / kgm^{-3}	$u(\rho)$ /(kg·m^{-3})
323.15	30.00	869.92	0.48	423.15	60.00	745.62	0.45
323.15	35.01	898.94	0.47	423.15	65.01	769.86	0.45
323.15	40.01	922.57	0.46	448.15	10.00	132.91	0.59
323.15	45.01	943.67	0.46	448.15	15.01	209.12	0.60
323.15	50.00	961.51	0.45	448.15	20.00	287.68	0.59
323.15	55.02	977.96	0.45	448.15	25.02	364.36	0.58
323.15	60.00	992.80	0.45	448.15	30.01	434.08	0.55
323.15	65.00	1006.28	0.45	448.15	35.01	494.67	0.53
348.15	10.02	235.50	0.85	448.15	40.00	546.83	0.50
348.15	15.03	466.20	0.93	448.15	45.02	591.58	0.49
348.15	20.01	626.94	0.68	448.15	50.02	629.98	0.47
348.15	25.02	712.10	0.57	448.15	55.01	663.32	0.46
348.15	30.02	766.65	0.51	448.15	60.02	692.95	0.45
348.15	35.01	807.15	0.49	448.15	65.01	718.86	0.45
348.15	40.01	839.39	0.47	473.15	10.01	122.67	0.57
348.15	45.03	866.41	0.46	473.15	15.01	190.08	0.57
348.15	50.01	889.42	0.45	473.15	20.00	258.90	0.57
348.15	55.00	909.77	0.45	473.15	25.01	326.62	0.56
348.15	60.00	927.93	0.45	473.15	30.01	389.60	0.54
348.15	65.01	943.40	0.44	473.15	35.00	446.35	0.52
373.15	10.01	189.61	0.71	473.15	40.01	496.97	0.50
373.15	15.00	333.02	0.78	473.14	45.01	541.26	0.49
373.15	20.00	481.64	0.72	473.14	50.02	580.33	0.47
373.15	25.02	589.15	0.62	473.14	55.00	614.62	0.46
373.15	30.02	661.93	0.55	473.14	60.01	645.35	0.45
373.15	35.01	714.85	0.51	473.15	65.01	672.58	0.45

Standard uncertainties in temperature and pressure $u(T)$ = 0.02 K and $u(p)$ = 0.02 MPa.

Table S2: Isothermal compressibility κ_T for the (CO_2 + n-heptane) system obtained from the experimental densities by means of numerical differentiation at temperatures T and pressures p, where x denotes the mole fraction of CO_2.

T/K	p/MPa	κ_T/GPa^{-1}					
		x = 0.0	x = 0.2	x = 0.4	x = 0.6	x = 0.8	x = 1.0
283.16	15.00	1.07	1.22	1.47	1.95	2.87	6.25
	20.00	1.01	1.15	1.36	1.80	2.52	4.83
	25.00	0.95	1.09	1.28	1.64	2.28	3.98
	30.00	0.92	1.03	1.21	1.51	2.04	3.39
	35.00	0.88	0.98	1.13	1.42	1.87	2.92
	40.00	0.85	0.94	1.07	1.33	1.73	2.61
	45.00	0.81	0.90	1.03	1.25	1.61	2.45
	50.00	0.78	0.86	0.98	1.18	1.49	2.17
	55.00	0.75	0.83	0.94	1.13	1.39	1.97
	60.00	0.74	0.80	0.90	1.05	1.30	1.81
	64.00	0.71	0.80	0.88	1.06	1.26	
298.15	15.00	1.17	1.39	1.69	2.36	3.87	11.1
	20.00	1.12	1.29	1.55	2.12	3.21	7.31
	25.00	1.06	1.21	1.45	1.91	2.83	5.55
	30.00	1.00	1.14	1.35	1.74	2.50	4.46
	35.00	0.95	1.08	1.26	1.61	2.23	3.81
	40.00	0.91	1.03	1.19	1.50	2.02	3.31
	45.00	0.87	0.98	1.13	1.40	1.87	2.94
	50.00	0.84	0.93	1.07	1.31	1.71	2.63
	55.00	0.81	0.90	1.02	1.25	1.60	2.40
	60.00	0.78	0.87	0.98	1.18	1.48	2.16
	64.00	0.76	0.85	0.95	1.13	1.44	

T/K	p/MPa	κ_T/GPa^{-1}					
		x = 0.0	x = 0.2	x = 0.4	x = 0.6	x = 0.8	x = 1.0
323.15	15.00	1.41	1.69	2.15	3.27	6.65	70.4
	20.00	1.31	1.55	1.93	2.80	4.92	17.4
	25.00	1.23	1.45	1.77	2.47	4.02	10.4
	30.00	1.16	1.35	1.63	2.19	3.41	7.46
	35.00	1.10	1.26	1.52	2.01	3.01	5.87
	40.00	1.04	1.20	1.41	1.84	2.63	4.86
	45.00	1.00	1.13	1.33	1.69	2.37	4.14
	50.00	0.96	1.07	1.25	1.57	2.13	3.57
	55.00	0.91	1.03	1.18	1.48	1.98	3.20
	60.00	0.87	0.98	1.12	1.38	1.81	2.86
	64.00	0.85	0.96	1.08	1.32	1.72	
348.15	15.00	1.69	2.09	2.80	4.78		98.0
	20.00	1.55	1.89	2.44	3.84	8.15	42.4
	25.00	1.44	1.73	2.19	3.25	5.93	20.1
	30.00	1.36	1.59	1.97	2.81	4.71	12.5
	35.00	1.27	1.48	1.81	2.50	4.01	9.07
	40.00	1.19	1.38	1.67	2.25	3.40	7.07
	45.00	1.13	1.30	1.55	2.04	3.03	5.79
	50.00	1.08	1.23	1.45	1.87	2.70	4.90
	55.00	1.03	1.16	1.36	1.75	2.44	4.24
	60.00	0.98	1.11	1.29	1.62	2.19	3.63
	64.00	0.94	1.09	1.24	1.54	2.11	
373.15	15.00	2.06	2.62	3.72	7.44		93.3
	20.00	1.86	2.31	3.13	5.39	13.9	56.9
	25.00	1.70	2.08	2.72	4.34	8.63	31.7
	30.00	1.57	1.89	2.41	3.60	6.57	19.4
	35.00	1.46	1.73	2.17	3.11	5.40	13.3
	40.00	1.37	1.60	1.98	2.75	4.44	9.97
	45.00	1.29	1.50	1.82	2.47	3.77	7.85
	50.00	1.21	1.41	1.68	2.23	3.31	6.48
	55.00	1.16	1.32	1.57	2.05	2.97	5.50
	60.00	1.11	1.25	1.47	1.89	2.65	4.74
	64.00	1.06	1.21	1.41	1.79	2.49	
398.15	15.00	2.51	3.32	5.08			85.7
	20.00	2.22	2.85	4.05	7.39	23.3	58.6
	25.00	2.01	2.51	3.41	5.63	13.1	38.5
	30.00	1.83	2.24	3.01	4.60	9.09	25.4
	35.00	1.70	2.03	2.60	3.90	6.98	17.6
	40.00	1.57	1.86	2.26	3.37	5.63	13.0
	45.00	1.46	1.72	2.12	2.99	4.76	10.2
	50.00	1.38	1.60	1.95	2.68	4.08	8.26
	55.00	1.30	1.51	1.80	2.42	3.60	6.87
	60.00	1.23	1.42	1.68	2.21	3.16	5.76
	64.00	1.18	1.36	1.60	2.08	2.99	
423.15	15.00	3.08	4.30	7.17			80.6
	20.00	2.69	3.54	5.31	11.19	31.7	57.3
	25.00	2.38	3.05	4.28	7.70	17.4	40. 7
	30.00	2.14	2.67	3.60	5.89	11.9	28.9
	35.00	1.96	2.38	3.12	4.79	8.87	20.9
	40.00	1.79	2.16	2.75	4.06	6.98	15.8
	45.00	1.67	1.97	2.48	3.52	5.81	12.4
	50.00	1.55	1.82	2.24	3.12	4.89	9.95
	55.00	1.46	1.70	2.05	2.81	4.26	8.27
	60.00	1.37	1.58	1.89	2.53	3.70	6.96
	64.00	1.32	1.52	1.80	2.38	3.44	
448.15	15.00	3.84	5.64	10.5			77.2
	20.00	3.24	4.44	7.05		37.6	55.5
	25.00	2.82	3.69	5.41	10.2	21.5	41.1

T/K	p/MPa	κ_T/GPa^{-1}					
		x = 0.0	x = 0.2	x = 0.4	x = 0.6	x = 0.8	x = 1.0
	30.00	2.49	3.17	4.38	7.44	14.7	30.6
	35.00	2.25	2.79	3.72	5.87	10.8	23.1
	40.00	2.05	2.49	3.23	4.86	8.46	17.9
	45.00	1.88	2.26	2.87	4.15	6.88	14.1
	50.00	1.74	2.07	2.57	3.63	5.76	11.5
	55.00	1.63	1.90	2.34	3.23	4.96	9.53
	60.00	1.52	1.77	2.14	2.90	4.28	8.04
	64.00	1.46	1.68	2.02	2.72	3.96	
473.15	15.00	4.85	7.54	15.8			74.8
	20.00	3.93	5.59	9.36	21.9	41.3	54.1
	25.00	3.34	4.50	6.81	13.0	25.0	40.9
	30.00	2.91	3.76	5.33	9.19	17.3	31.3
	35.00	2.59	3.26	4.42	7.03	12.6	24.3
	40.00	2.33	2.88	3.77	5.75	9.87	19.3
	45.00	2.12	2.57	3.29	4.84	7.97	15.5
	50.00	1.95	2.33	2.94	4.20	6.62	12.7
	55.00	1.81	2.14	2.65	3.70	5.67	10.6
	60.00	1.69	1.97	2.41	3.30	4.88	9.00
	64.00	1.60	1.89	2.27	3.04	4.40	

Table S3: Isobaric expansivity α_p for the (CO_2 + n-heptane) system obtained from the experimental densities by means of numerical differentiation at temperatures T and pressures p, where x denotes the mole fraction of CO_2.

p/MPa	T/K	$10^3\ \alpha_p$/K^{-1}					
		x = 0.0	x = 0.2	x = 0.4	x = 0.6	x = 0.8	x = 1.0
10.00	303.15	11.67	13.09	15.47	21.17	35.39	215.5
	323.15	11.99	13.83	16.89	24.27	44.83	249.2
	348.15	12.70	14.87	18.83	29.95		143.5
	373.15	13.47	16.23	21.48			72.14
	398.15	14.43	17.93	25.26			51.77
	423.15	15.62	20.15	30.89			42.27
	448.15	17.11	23.14	39.07			35.33
15.00	303.15	11.22	12.45	14.52	19.20	29.37	77.04
	323.15	11.43	13.05	15.63	21.39	36.37	126.3
	348.15	11.98	13.85	17.01	24.67	48.28	148.9
	373.15	12.57	14.81	18.76	28.32	64.96	108.1
	398.15	13.27	15.98	20.92	34.75	73.18	70.01
	423.15	14.08	17.38	23.63		67.84	52.25
	448.15	15.00	19.02	26.85		58.85	42.14
20.00	303.15	10.83	11.93	13.76	17.84	25.93	55.52
	323.15	10.96	12.41	14.67	19.44	30.33	75.37
	348.15	11.38	13.02	15.70	21.63	35.89	97.54
	373.15	11.84	13.75	16.92	23.94	43.49	96.70
	398.15	12.39	14.60	18.34	27.18	48.75	76.95
	423.15	12.95	15.54	20.00	30.75	49.28	59.10
	448.15	13.56	16.62	21.83	33.24	47.85	47.20
25.00	303.15	10.47	11.45	13.10	16.70	23.38	45.63
	323.15	10.56	11.84	13.85	17.94	26.50	56.20
	348.15	10.88	12.34	14.63	19.50	30.27	69.57
	373.15	11.21	12.90	15.54	21.22	34.52	75.59
	398.15	11.62	13.52	16.55	23.12	37.71	69.69
	423.15	12.05	14.19	17.63	25.04	39.39	58.43
	448.15	12.50	14.93	18.76	26.80	39.54	48.29
30.00	303.15	10.14	11.04	12.53	15.75	21.60	39.62
	323.15	10.20	11.37	13.19	16.77	24.14	46.23

p/MPa	T/K	$10^3\ \alpha_p/K^{-1}$					
		x = 0.0	x = 0.2	x = 0.4	x = 0.6	x = 0.8	x = 1.0
	348.15	10.45	11.76	13.79	17.90	26.68	54.65
	373.15	10.70	12.19	14.46	19.19	29.23	60.05
	398.15	11.02	12.66	15.22	20.46	31.28	59.29
	423.15	11.32	13.17	16.00	21.65	32.38	53.71
	448.15	11.65	13.72	16.78	22.73	32.69	46.72
35.00	303.15	9.86	10.66	12.03	14.99	19.95	35.45
	323.15	9.84	10.95	12.61	15.80	22.08	40.06
	348.15	10.06	11.26	13.08	16.68	23.94	45.83
	373.15	10.25	11.59	13.46	17.64	25.75	49.81
	398.15	10.48	11.95	14.18	18.55	27.03	50.55
	423.15	10.74	12.32	14.89	19.36	28.07	48.11
	448.15	10.97	12.75	15.28	20.19	28.71	43.64
40.00	303.15	9.60	10.34	11.57	14.29	18.76	32.21
	323.15	9.55	10.58	12.09	15.00	20.58	35.71
	348.15	9.71	10.81	12.48	15.70	21.89	39.75
	373.15	9.86	11.08	12.88	16.39	23.29	42.92
	398.15	10.03	11.35	13.33	17.11	24.34	44.06
	423.15	10.22	11.65	13.78	17.69	24.79	42.78
	448.15	10.38	11.97	14.16	18.24	25.29	39.92
45.00	303.15	9.37	10.03	11.19	13.73	17.70	29.83
	323.15	9.29	10.25	11.64	14.31	19.34	32.51
	348.15	9.39	10.45	11.95	14.87	20.32	35.58
	373.15	9.50	10.63	12.28	15.39	21.29	37.99
	398.15	9.64	10.84	12.62	15.91	21.94	38.94
	423.15	9.75	11.08	12.95	16.38	22.43	38.32
	448.15	9.89	11.31	13.27	16.82	22.97	36.67
50.00	303.15	9.14	9.76	10.83	13.19	16.86	27.99
	323.15	9.04	9.93	11.25	13.72	18.27	30.02
	348.15	9.13	10.08	11.49	14.15	19.08	32.31
	373.15	9.19	10.24	11.76	14.50	19.82	34.16
	398.15	9.28	10.42	12.02	15.00	20.27	35.08
	423.15	9.38	10.58	12.28	15.38	20.55	34.82
	448.15	9.48	10.76	12.52	15.61	20.96	33.60
55.00	303.15	8.92	9.51	10.51	12.76	16.12	26.32
	323.15	8.81	9.65	10.89	13.19	17.34	28.00
	348.15	8.88	9.77	11.09	13.55	17.96	29.76
	373.15	8.91	9.89	11.28	13.77	18.54	31.22
	398.15	8.97	10.01	11.49	14.13	18.78	32.02
	423.15	9.03	10.15	11.71	14.48	19.06	31.96
	448.15	9.10	10.29	11.88	14.67	19.49	31.12
60.00	303.15	8.74	9.28	10.23	12.31	15.39	24.91
	323.15	8.59	9.41	10.58	12.73	16.59	26.34
	348.15	8.64	9.50	10.73	13.01	17.10	27.74
	373.15	8.66	9.55	10.88	13.14	17.50	28.91
	398.15	8.68	9.65	11.05	13.46	17.69	29.53
	423.15	8.73	9.79	11.19	13.76	17.83	29.49
	448.15	8.77	9.88	11.32	13.83	18.15	28.89
65.00	303.15	8.58	9.07	9.96	11.95	14.82	23.71
	323.15	8.42	9.17	10.28	12.31	15.92	25.06
	348.15	8.41	9.23	10.40	12.53	16.28	26.00
	373.15	8.41	9.28	10.50	12.60	16.59	26.97
	398.15	8.44	9.35	10.65	12.84	16.70	27.56
	423.15	8.45	9.44	10.77	13.10	16.84	27.39
	448.15	8.46	9.51	10.85	13.13	17.12	27.02

3.2 Parameters of the Redlich-Kister correlation for the excess molar volume

Redlich-Kister equation is given in the following form:

$$V_m^E = x(1-x)\sum_{i=1}^{3} A_i (2x-1)^{i-1} \quad \text{(S1)}$$

where V_m^E and x are the excess molar volume and mole fraction of CO_2, respectively. The parameters A_i are given in Table S4.

Table S4. Parameters of the Redlich-Kister correlation for the excess molar volume of CO_2 + n-heptane.

T / K	p / MPa	A_1/(cm^3·mol^{-1})	A_2/(cm^3·mol^{-1})	A_3/(cm^3·mol^{-1})	Δ_{AAD}/(cm^3·mol^{-1})
283.15	10	1.308	0.511	0.002	0.009
283.15	15	2.896	1.852	1.124	0.001
283.15	20	3.822	2.692	2.006	0.008
283.15	25	4.295	2.864	2.161	0.015
283.15	30	4.679	3.185	2.296	0.012
283.15	35	4.842	3.141	2.457	0.016
283.15	40	5.020	3.280	2.460	0.019
283.15	45	5.071	3.166	2.469	0.022
283.15	50	5.153	3.246	2.505	0.019
283.15	55	5.127	3.141	2.492	0.024
283.15	60	5.156	3.230	2.612	0.022
283.15	65	5.151	3.164	2.641	0.022
283.15	68	5.074	3.222	2.620	0.030
298.15	10	-6.207	-5.441	-4.222	0.071
298.15	15	-1.259	-1.082	-1.416	0.054
298.15	20	0.998	0.943	-0.113	0.026
298.15	25	2.189	1.658	0.392	0.022
298.15	30	2.968	2.244	0.893	0.018
298.15	35	3.434	2.398	0.803	0.020
298.15	40	3.787	2.699	1.086	0.013
298.15	45	3.983	2.647	0.920	0.014
298.15	50	4.143	2.807	1.159	0.013
298.15	55	4.243	2.746	1.124	0.013
298.15	60	4.299	2.843	1.226	0.009
298.15	65	4.349	2.792	1.194	0.009
298.15	68	4.366	2.842	1.088	0.007
323.15	10	-120.016	-139.015	-105.302	2.025
323.15	15	-24.916	-12.523	2.311	1.083
323.15	20	-15.479	1.041	17.962	1.138
323.15	25	-12.195	5.736	23.820	1.224
323.15	30	-10.626	8.618	27.845	1.305
323.15	35	-8.590	8.844	26.308	1.221
323.15	40	-6.613	8.675	23.970	1.080
323.15	45	-0.770	4.459	9.153	0.412
323.15	50	4.402	0.750	-3.758	0.186
323.15	55	9.759	-3.488	-17.947	0.829
323.15	60	15.577	-8.145	-33.670	1.537
323.15	65	22.110	-13.525	-51.553	2.346
323.15	68	25.992	-16.709	-62.433	2.830
348.15	15	-72.515	-73.086	-49.176	0.972
348.15	20	-25.969	-25.459	-22.870	0.206
348.15	25	-12.781	-11.111	-10.026	0.106
348.15	30	-6.804	-4.885	-4.139	0.053

T / K	p / MPa	A_1/(cm^3·mol^{-1})	A_2/(cm^3·mol^{-1})	A_3/(cm^3·mol^{-1})	Δ_{AAD}/(cm^3·mol^{-1})
348.15	35	-3.508	-2.397	-2.454	0.047
348.15	40	-1.468	-0.578	-0.911	0.032
348.15	45	-0.171	0.278	-0.437	0.030
348.15	50	0.807	1.004	0.038	0.026
348.15	55	1.480	1.292	0.070	0.026
348.15	60	2.001	1.638	0.492	0.019
348.15	65	2.354	1.895	0.520	0.018
348.15	68	2.536	2.021	0.324	0.017
373.15	15	-134.720	-127.663	-77.117	1.482
373.15	20	-56.994	-58.088	-52.288	0.440
373.15	25	-28.902	-26.290	-22.332	0.199
373.15	30	-16.450	-13.068	-10.311	0.098
373.15	35	-9.907	-7.448	-6.250	0.076
373.15	40	-6.002	-4.094	-3.762	0.060
373.15	45	-3.545	-2.315	-2.420	0.052
373.15	50	-1.856	-0.848	-1.347	0.038
373.15	55	-0.648	-0.153	-1.054	0.035
373.15	60	0.233	0.472	-0.434	0.031
373.15	65	0.911	0.858	-0.275	0.028
373.15	68	1.206	1.108	-0.177	0.027
398.15	15	-177.287	-154.953	-93.632	0.213
398.15	20	-88.901	-81.617	-61.646	0.388
398.15	25	-48.370	-42.457	-33.325	0.262
398.15	30	-28.634	-23.125	-17.725	0.158
398.15	35	-18.241	-13.813	-10.496	0.143
398.15	40	-11.817	-8.370	-6.393	0.078
398.15	45	-7.862	-5.464	-4.704	0.067
398.15	50	-5.217	-3.324	-2.812	0.042
398.15	55	-3.370	-2.192	-2.151	0.039
398.15	60	-1.991	-1.131	-1.418	0.024
398.15	65	-0.989	-0.521	-0.961	0.024
398.15	68	-0.516	-0.260	-1.092	0.017
423.15	15	-205.338	-136.027	-39.008	0.315
423.15	20	-112.926	-91.209	-59.557	0.349
423.15	25	-66.373	-54.244	-38.916	0.286
423.15	30	-41.275	-32.438	-23.817	0.191
423.15	35	-26.890	-21.096	-16.707	0.162
423.15	40	-18.210	-13.446	-10.722	0.115
423.15	45	-12.689	-9.564	-8.453	0.102
423.15	50	-8.853	-6.395	-5.890	0.085
423.15	55	-6.256	-4.765	-5.042	0.071
423.15	60	-4.267	-3.235	-3.741	0.059
423.15	65	-2.856	-2.333	-3.136	0.049
423.15	68	-2.150	-1.873	-2.905	0.046
448.15	15	-218.671	-102.419	10.563	0.442
448.15	20	-129.150	-88.156	-45.700	0.251
448.15	25	-80.553	-58.524	-36.224	0.256
448.15	30	-52.355	-39.116	-27.038	0.222
448.15	35	-35.426	-26.488	-19.604	0.177
448.15	40	-24.674	-18.290	-14.034	0.140
448.15	45	-17.655	-13.328	-10.965	0.126
448.15	50	-12.801	-9.585	-8.377	0.103
448.15	55	-9.389	-7.379	-6.988	0.090
448.15	60	-6.885	-5.492	-5.454	0.078
448.15	65	-5.003	-4.177	-4.523	0.064
448.15	68	-4.128	-3.773	-4.227	0.060

T / K	p / MPa	A_1/(cm^3·mol^{-1})	A_2/(cm^3·mol^{-1})	A_3/(cm^3·mol^{-1})	Δ_{AAD}/(cm^3·mol^{-1})
473.15	15	-217.946	-64.691	34.999	0.002
473.15	20	-137.906	-77.491	-30.062	0.210
473.15	25	-90.191	-57.095	-30.043	0.234
473.15	30	-61.059	-42.091	-26.857	0.223
473.15	35	-42.565	-30.105	-20.862	0.207
473.15	40	-30.463	-21.788	-15.935	0.168
473.15	45	-22.272	-16.404	-13.170	0.147
473.15	50	-16.559	-12.304	-10.204	0.125
473.15	55	-12.498	-9.655	-8.575	0.106
473.15	60	-9.459	-7.504	-6.857	0.090
473.15	65	-7.197	-6.018	-5.612	0.073
473.15	68	-6.104	-4.986	-5.103	0.067

3.4 Saturated-phase densities

Table S5. Experimental saturated phase densities for the (CO_2 + n-heptane) system measured at temperatures, T and pressures p; $u(\rho)$ denotes the combined standard uncertainty of each density measurement.[a]

T/ K	p/ MPa	ρ/ (kg·m^{-3})	$u_c(\rho)$/(kg·m^{-3})	T/ K	p/ MPa	ρ/ (kg·m^{-3})	$u_c(\rho)$/(kg·m^{-3})
		Liquid Phase				Vapour Phase	
298.0	0.33	682.8	0.5	297.8	0.34	8.2	0.5
298.0	0.36	682.9	0.5	297.8	1.12	24.2	0.5
298.0	0.39	683.2	0.5	297.8	1.87	39.5	0.6
298.0	1.15	690.0	0.3	297.8	2.66	58.3	0.6
298.0	1.91	697.9	0.4	297.8	2.95	67.0	0.7
298.0	2.13	700.5	0.5	297.8	3.19	73.8	0.7
298.0	2.46	704.5	0.6	297.8	3.19	73.8	0.7
298.0	2.70	707.8	0.7	297.8	3.77	90.2	0.8
298.0	2.70	707.9	0.7	297.8	3.90	95.5	0.8
298.0	3.01	712.4	0.8	297.8	4.35	110.4	1.0
298.0	3.25	716.4	0.9	297.8	4.35	110.4	1.0
298.0	3.61	723.3	0.9	297.8	4.35	110.4	1.0
298.0	3.82	727.1	1.0	297.8	4.39	113.1	1.0
298.0	3.97	730.9	1.0	297.8	4.84	130.5	1.1
298.0	4.40	742.4	1.0	297.8	4.85	130.9	1.1
298.0	4.46	744.3	1.0	297.8	5.00	138.1	1.2
298.0	4.65	751.4	1.1	297.8	5.00	138.1	1.2
298.0	4.89	757.8	1.0	297.8	5.23	149.7	1.4
298.0	4.89	756.6	0.8	297.8	5.32	154.9	1.4
298.0	5.04	762.4	0.8	297.8	5.52	166.3	1.6
298.0	5.27	769.6	0.6	297.8	5.63	174.1	1.8
298.0	5.36	772.2	0.6	297.8	5.78	184.3	2.0
298.0	5.55	774.8	0.4	297.8	5.81	187.1	2.0
298.0	5.67	771.7	0.6	297.7	5.94	199.4	2.3
298.0	5.79	766.5	1.0	297.7	5.95	200.0	2.3
298.0	5.84	764.6	1.3	297.7	5.96	200.7	2.3
298.0	5.85	763.6	1.2	297.7	5.96	201.0	2.3
297.9	5.97	754.6	1.7	297.7	5.96	201.0	2.3
297.9	5.98	753.5	1.7	297.8	5.97	200.2	2.4
297.9	5.98	752.4	1.8	297.8	5.97	200.2	2.4
297.9	6.00	751.1	1.8	297.8	5.97	200.8	2.4
298.0	6.00	751.6	1.8	297.8	5.97	200.4	2.4
298.0	6.01	752.3	1.9	297.7	5.98	202.7	2.4
297.9	6.01	749.8	1.9	297.7	5.99	203.6	2.4
297.9	6.02	748.8	2.0	297.7	6.00	205.0	2.5
297.9	6.03	747.9	2.0	297.7	6.00	205.0	2.5
297.9	6.04	747.4	2.0	297.7	6.01	205.2	2.5
297.9	6.05	747.0	2.1	297.7	6.01	206.1	2.5
297.9	6.05	746.8	2.1	297.7	6.02	206.4	2.5
298.0	6.16	734.1	2.9	297.7	6.05	209.5	2.6
298.0	6.16	734.0	3.0	297.8	6.11	213.0	2.8
298.0	6.17	733.3	3.0	297.7	6.11	214.6	2.8
298.0	6.17	733.3	3.0	297.7	6.12	214.9	2.8
298.0	6.17	733.1	3.0	297.7	6.12	214.9	2.8
298.0	6.17	733.1	3.0	297.7	6.12	215.6	2.9
298.0	6.17	732.8	3.0	297.8	6.12	214.6	2.9
297.9	6.19	733.2	3.2	297.8	6.12	214.6	2.9
				297.7	6.13	216.3	2.9
				297.8	6.13	215.6	2.9
				297.8	6.15	216.7	3.0
				297.8	6.15	217.9	3.0

T/ K	p/ MPa	ρ/ (kg·m^{-3}) Liquid Phase	$u_c(\rho)$/(kg·m^{-3})	T/ K	p/ MPa	ρ/ (kg·m^{-3}) Vapour Phase	$u_c(\rho)$/(kg·m^{-3})
				297.7	6.16	219.5	3.0
322.7	1.11	664.2	0.2	322.7	1.08	20.2	0.4
322.7	1.16	664.4	0.2	322.7	1.14	20.7	0.4
322.7	2.20	670.7	0.3	322.7	2.93	57.1	0.5
322.7	2.98	675.7	0.3	322.7	3.95	81.2	0.6
322.7	4.00	682.9	0.3	322.7	4.60	98.6	0.7
322.7	4.66	687.9	0.4	322.7	5.49	125.4	0.9
322.7	5.49	694.7	0.4	322.7	5.96	142.4	1.0
322.7	5.97	698.6	0.4	322.7	6.60	167.5	1.1
322.7	6.44	701.9	0.4	322.7	7.10	191.4	1.4
322.6	6.61	703.0	0.4	322.7	7.24	198.9	1.4
322.7	6.84	704.1	0.4	322.7	7.50	214.7	1.6
322.6	7.10	704.7	0.4	322.7	7.82	237.0	1.9
322.7	7.11	704.7	0.4	322.7	8.10	260.3	2.4
322.7	7.25	704.5	0.4	322.7	8.32	283.7	2.9
322.6	7.38	704.3	0.4	322.7	8.62	326.9	4.6
322.7	7.52	702.9	0.4	322.7	8.78	362.7	7.4
322.6	7.60	702.5	0.5	322.7	8.90	412.3	21
322.7	7.84	697.9	0.6	322.7	8.99	481.5	21
322.7	8.12	688.9	1.0				
322.7	8.35	676.5	1.6				
322.7	8.46	669.1	2.0				
322.7	8.65	644.0	3.4				
322.7	8.81	614.1	7.5				
322.7	8.93	563.6	(b)				
322.7	8.95	568.8	(b)				
322.7	9.02	506.3	(b)				
347.8	1.32	640.0	0.2	347.8	1.28	22.7	0.4
347.8	2.06	642.6	0.2	347.8	2.03	35.7	0.4
347.8	3.47	647.5	0.3	347.8	3.43	62.5	0.5
347.8	4.00	649.4	0.3	347.8	3.96	73.5	0.5
347.9	5.58	654.5	0.3	347.9	5.58	111.0	0.7
347.9	5.96	655.6	0.3	347.8	5.94	120.5	0.7
347.8	6.30	656.5	0.3	347.8	6.28	129.8	0.7
347.9	6.61	657.2	0.3	347.8	6.59	138.7	0.8
347.8	6.88	657.8	0.3	347.8	6.87	146.9	0.8
347.8	7.14	658.2	0.3	347.8	7.12	155.0	0.8
347.8	7.37	658.5	0.3	347.8	7.35	162.6	0.9
347.8	7.62	658.6	0.3	347.8	7.60	170.9	0.9
347.8	7.86	658.6	0.3	347.8	7.84	179.3	1.0
347.8	8.08	658.5	0.3	347.8	8.06	187.6	1.0
347.8	8.29	658.2	0.3	347.8	8.26	195.5	1.0
347.8	8.47	657.7	0.3	347.8	8.45	203.3	1.1
347.8	8.66	657.1	0.3	347.8	8.63	211.1	1.1
347.8	8.82	656.3	0.3	347.8	8.80	218.7	1.2
347.8	8.98	655.4	0.3	347.8	8.96	226.1	1.2
347.8	9.12	654.3	0.4	347.8	9.10	233.1	1.3
347.8	9.26	653.1	0.4	347.8	9.24	240.3	1.3
347.8	9.40	651.6	0.4	347.7	9.37	247.4	1.4
347.8	9.52	650.1	0.4	347.7	9.49	254.2	1.5
347.8	9.63	648.5	0.5	347.7	9.60	260.7	1.5
347.8	9.74	646.7	0.5	347.8	9.72	267.9	1.6
347.8	9.84	644.7	0.5	347.8	9.82	274.6	1.7
347.8	9.94	642.8	0.6	347.8	9.91	280.9	1.8
347.8	10.02	640.7	0.6	347.8	10.00	287.1	1.8

T/ K	p/ MPa	ρ/ (kg·m^{-3})	$u_c(\rho)$/(kg·m^{-3})	T/ K	p/ MPa	ρ/ (kg·m^{-3})	$u_c(\rho)$/(kg·m^{-3})
		Liquid Phase				Vapour Phase	
347.8	10.10	638.6	0.7	347.8	10.08	293.0	1.9
347.8	10.16	636.3	0.7	347.8	10.14	297.9	2.0
347.8	10.26	632.9	0.8	347.8	10.24	305.7	2.1
347.8	10.36	629.5	0.9	347.8	10.34	314.1	2.3
347.8	10.45	625.7	1.0	347.8	10.43	322.1	2.4
347.8	10.53	621.7	1.1	347.8	10.51	330.0	2.6
347.8	10.68	613.0	1.4	347.8	10.58	338.2	2.8
347.8	10.73	607.9	1.6	347.8	10.71	353.8	3.3
347.8	10.80	603.1	1.9	347.8	10.78	363.4	3.7
347.9	10.84	603.0	2.1	347.9	10.81	372.6	3.9
347.8	10.87	597.5	2.3	347.8	10.90	380.7	4.7
347.9	10.93	595.0	2.8	347.8	11.00	400.8	6.5
347.9	11.02	578.1	4.4	347.8	11.08	419.3	10.9
347.9	11.11	495.3	11	347.8	11.08	423.9	11.1
373.0	1.15	614.0	0.5	372.9	1.12	19.7	0.3
373.0	1.96	615.5	0.5	372.9	1.92	32.7	0.4
373.0	4.21	619.3	0.5	372.9	4.16	72.7	0.5
373.0	5.06	620.5	0.5	372.9	5.02	89.8	0.5
373.0	5.79	621.0	0.5	372.9	5.77	105.7	0.6
373.0	6.56	621.3	0.5	372.9	6.55	123.4	0.6
373.0	7.26	621.2	0.6	372.9	7.26	141.0	0.7
373.0	7.93	620.6	0.6	372.9	7.90	158.3	0.7
373.0	8.55	619.3	0.6	372.9	8.54	176.7	0.8
373.0	9.17	617.4	0.6	372.9	9.15	196.0	0.9
372.9	9.72	614.5	0.7	372.8	9.70	215.4	0.9
372.9	10.24	610.8	0.7	372.8	10.21	235.1	1.0
372.9	10.70	605.8	0.7	372.9	10.35	240.7	1.1
373.0	10.76	604.6	0.7	372.8	10.67	255.1	1.2
372.9	11.13	599.6	0.8	372.9	10.74	258.1	1.2
373.0	11.13	598.9	0.8	372.8	11.09	275.8	1.3
373.0	11.49	591.7	0.9	372.9	11.10	276.4	1.3
372.9	11.52	591.4	0.9	372.9	11.46	296.4	1.5
372.9	11.87	581.3	1.0	372.8	11.48	297.9	1.5
373.0	12.13	572.3	1.3	372.9	11.80	318.8	1.8
372.9	12.18	568.5	1.4	372.8	11.83	321.3	1.8
373.0	12.22	567.0	1.5	372.9	12.10	343.6	2.3
373.0	12.30	561.8	1.7	372.8	12.15	347.1	2.4
373.0	12.39	555.7	2.1	372.9	12.19	352.1	2.5
373.0	12.48	547.9	2.7	372.9	12.28	361.0	2.8
373.0	12.56	536.3	4.1	372.9	12.36	370.7	3.2
373.0	12.61	527.4	6.1	372.9	12.53	397.3	5.2
373.0	12.69	463.4	39	372.9	12.58	409.3	7.0
				372.9	12.66	430.4	41
423.3	1.78	559.3	0.5	423.0	1.75	32.5	0.3
423.3	3.22	558.2	0.5	423.1	3.19	55.0	0.4
423.3	4.45	556.8	0.5	423.1	4.43	75.6	0.4
423.3	5.74	554.3	0.5	423.1	5.72	99.0	0.5
423.3	6.03	553.5	0.5	423.1	6.05	105.3	0.5
423.3	7.50	548.9	0.6	423.0	7.49	134.6	0.6
423.3	8.89	542.0	0.6	423.0	10.10	200.0	0.9
423.3	10.13	532.1	0.7	423.0	10.27	205.3	0.9
423.3	10.31	530.4	0.7	423.0	10.76	221.2	1.0
423.3	10.79	524.0	0.8	423.0	11.60	252.7	1.2
423.2	11.65	510.6	0.8	423.0	12.51	300.7	2.0
423.3	12.55	482.1	1.1	423.0	12.71	319.4	2.3

T/ K	p/ MPa	ρ/ (kg·m^{-3})	$u_c(\rho)$/(kg·m^{-3})	T/ K	p/ MPa	ρ/ (kg·m^{-3})	$u_c(\rho)$/(kg·m^{-3})
		Liquid Phase				Vapour Phase	
423.3	12.73	473.6	1.4	423.0	12.75	322.1	2.4
423.3	12.80	465.1	1.6	423.0	12.80	328.2	2.6
423.3	12.81	464.3	1.6	423.0	12.86	336.9	2.8
423.3	12.83	461.7	1.7	423.1	13.12	373.8	5.1
423.2	12.85	461.0	1.7	423.0	13.20	396.7	6.0
423.3	12.89	456.6	1.9	448.1	2.16	41.9	0.4
423.3	12.94	449.4	2.2	448.1	3.10	56.6	0.4
423.2	13.05	434.6	3.8	448.2	3.94	70.4	0.4
423.3	13.08	429.3	5.2	448.2	5.15	91.4	0.5
423.3	13.14	416.7	5.3	448.1	5.63	100.4	0.5
423.3	13.20	406.4	5.3	448.1	6.54	118.1	0.5
448.4	1.28	527.5	0.2	448.1	7.36	135.2	0.6
448.4	2.18	526.3	0.3	448.1	8.17	153.8	0.6
448.4	3.11	524.2	0.3	448.1	8.98	174.2	0.7
448.4	3.96	522.2	0.3	448.1	9.76	196.8	0.8
448.4	5.17	518.3	0.3	448.0	10.51	222.4	0.9
448.4	5.62	516.3	0.3	448.1	11.09	248.3	1.2
448.4	6.55	512.0	0.4	448.1	11.24	255.4	1.4
448.4	7.38	507.4	0.4	448.1	11.34	261.4	1.5
448.4	8.20	501.7	0.4	448.1	11.50	271.5	1.7
448.4	9.01	494.3	0.5	448.1	11.65	283.9	2.1
448.3	9.80	484.7	0.5	448.1	11.80	304.1	3.0
448.3	10.55	471.8	0.7	448.1	11.92	329.9	5.7
448.4	11.13	456.6	0.9	448.1	11.97	316.3	11.3
448.4	11.22	452.9	1.0				
448.3	11.28	451.3	1.1				
448.4	11.38	445.6	1.2				
448.4	11.53	438.5	1.4				
448.4	11.68	428.1	1.8				
448.4	11.83	415.7	2.8				
448.3	11.96	380.5	9.6				
448.4	11.98	354.3	20.4				

(a) Standard uncertainties in temperature and pressure are $u(T)$ = 0.2 K and $u(p)$ = 0.05 MPa

(b) A combined standard uncertainty of density is not given for these data close to the critical point

3.5 Vapour-liquid equilibrium data

Table S6. Experimental VLE data for the (CO_2 + n-heptane) system at temperatures T, and mole fraction x of CO_2, where p denotes bubble- or dew-pressure, $u(X)$, denote the standard uncertainty of property X.

T/K	$u(T)$/K	p/MPa	$u(p)$/MPa	x	$u(x)$	Status
298.15	0.1	0.231	0.1	0.0240	0.00010	Bubble
298.15	0.1	1.020	0.1	0.1290	0.00047	Bubble
298.15	0.1	1.974	0.1	0.2654	0.00082	Bubble
298.15	0.1	2.918	0.1	0.3783	0.00099	Bubble
298.15	0.1	3.650	0.1	0.4739	0.00105	Bubble
298.15	0.1	3.910	0.1	0.5269	0.00105	Bubble
298.15	0.1	4.280	0.1	0.5854	0.00102	Bubble
298.15	0.1	4.760	0.1	0.6794	0.00091	Bubble
298.15	0.1	4.920	0.1	0.7283	0.00083	Bubble
298.15	0.1	5.210	0.1	0.7964	0.00068	Bubble
298.15	0.1	5.410	0.1	0.8367	0.00057	Bubble
298.15	0.1	5.680	0.1	0.9145	0.00033	Bubble
298.15	0.1	6.020	0.1	0.9650	0.00014	Bubble
298.15	0.1	6.254	0.1	0.9895	0.00004	Bubble
323.15	0.1	0.351	0.2	0.0325	0.00013	Bubble
323.15	0.1	1.330	0.2	0.1288	0.00047	Bubble
323.15	0.1	3.080	0.2	0.2894	0.00086	Bubble
323.15	0.1	4.180	0.2	0.3982	0.00101	Bubble
323.15	0.1	5.080	0.2	0.4738	0.00105	Bubble
323.15	0.1	5.590	0.2	0.5268	0.00105	Bubble
323.15	0.1	6.980	0.2	0.6754	0.00092	Bubble
323.15	0.1	7.330	0.2	0.7255	0.00084	Bubble
323.15	0.1	7.490	0.2	0.7438	0.00080	Bubble
323.15	0.1	8.020	0.2	0.8308	0.00059	Bubble
323.15	0.1	8.060	0.2	0.8358	0.00058	Bubble
323.15	0.1	8.350	0.2	0.8769	0.00045	Bubble
323.15	0.1	8.520	0.2	0.9018	0.00037	Bubble
323.15	0.1	8.610	0.2	0.9137	0.00033	Bubble
323.15	0.1	8.565	0.3	0.9612	0.00016	Dew
323.15	0.1	8.050	0.3	0.9776	0.00009	Dew
323.15	0.1	6.760	0.3	0.9856	0.00006	Dew
373.15	0.2	0.521	0.1	0.0240	0.00010	Bubble
373.15	0.2	2.150	0.1	0.1283	0.00047	Bubble
373.15	0.2	3.540	0.1	0.2154	0.00071	Bubble
373.15	0.2	4.660	0.1	0.2882	0.00086	Bubble
373.15	0.2	6.237	0.1	0.3848	0.00099	Bubble
373.15	0.2	7.750	0.1	0.4718	0.00105	Bubble
373.15	0.2	8.620	0.1	0.5256	0.00105	Bubble
373.15	0.2	9.820	0.1	0.6003	0.00101	Bubble
373.15	0.2	11.050	0.1	0.6748	0.00092	Bubble
373.15	0.2	11.530	0.1	0.7105	0.00086	Bubble
373.15	0.2	11.720	0.1	0.7251	0.00084	Bubble
373.15	0.2	12.300	0.1	0.7775	0.00073	Bubble
373.15	0.2	12.650	0.1	0.8316	0.00059	Bubble
373.15	0.2	12.650	0.15	0.8704	0.00047	Dew
373.15	0.2	12.020	0.15	0.9054	0.00036	Dew
373.15	0.2	11.250	0.15	0.9303	0.00027	Dew
373.15	0.2	9.627	0.15	0.9443	0.00022	Dew
423.15	0.5	0.375	0.1	0.0000	0.00000	Bubble
423.15	0.5	1.276	0.1	0.0473	0.00019	Bubble
423.15	0.5	2.860	0.1	0.1327	0.00048	Bubble
423.15	0.5	5.780	0.1	0.2725	0.00083	Bubble

T/K	$u(T)$/K	p/MPa	$u(p)$/MPa	x	$u(x)$	Status
423.15	0.5	8.250	0.1	0.3907	0.00100	Bubble
423.15	0.5	10.860	0.1	0.5263	0.00105	Bubble
423.15	0.5	12.150	0.1	0.5986	0.00101	Bubble
423.15	0.5	12.650	0.1	0.6417	0.00097	Bubble
423.15	0.5	13.020	0.1	0.6661	0.00093	Bubble
423.15	0.5	13.110	0.1	0.6746	0.00092	Bubble
423.15	0.5	13.150	0.1	0.6786	0.00092	Bubble
423.15	0.5	13.120	0.1	0.7251	0.00084	Bubble
423.15	0.5	13.070	0.15	0.7451	0.00080	(a)
423.15	0.5	12.720	0.15	0.7835	0.00071	Dew
423.15	0.5	12.480	0.15	0.7980	0.00068	Dew
423.15	0.5	11.010	0.3	0.8326	0.00059	Dew
423.15	0.5	9.570	0.15	0.8621	0.00050	Dew

(a) designation uncertain; treated as a dew point for the purpose of estimating the critical point.

The critical points were estimated by fitting the near-critical data to the following scaling equation

$$x = x_c + \left(\lambda_1 + \varepsilon\frac{\lambda_2}{2}\right)(p_c - p) + \varepsilon\frac{\mu}{2}(p_c - p)^{\beta}, \qquad \text{(S2)}$$

where β = 0.325, ε = 1 for bubble points or -1 for dew points, x_c is the critical composition, p_c is the critical pressure, and λ_1, λ_2 and μ are adjustable parameters. The results are given in Table S7 and are plotted in Fig. S6.

Table S7: Critical pressure, temperature and composition and their standard uncertainties for (CO_2 + n-heptane).

T_c/K	$u(T_c)$/K	p_c/MPa	$u(p_c)$/MPa	x_c	$u(x_c)$
323.15	0.1	8.8	0.2	0.951	0.004
373.15	0.2	12.7	0.2	0.849	0.004
423.15	0.5	13.2	0.2	0.725	0.018

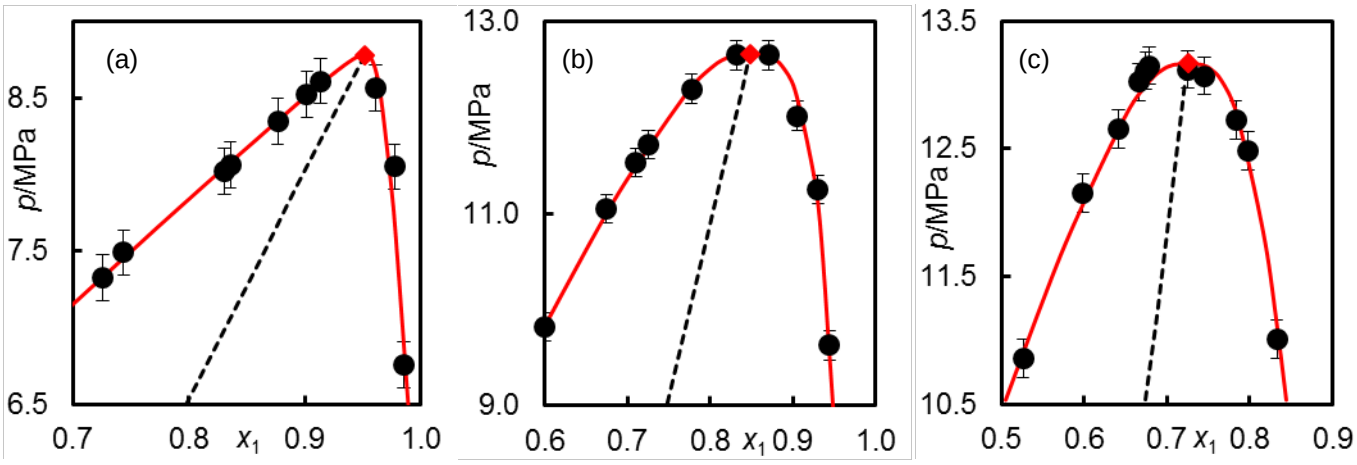

Figure S6: Critical point estimation for the CO_2 + n-heptane system at (a) T = 323 K, (b) T = 373 K, and (c) T = 423 K: ●, experimental VLE data; ——, equation (S1); - - - -, rectilinear diameter, ◆, calculated critical point.

4. Empirical correlations

4.1 Compressed liquid densities

Experimental compressed liquid densities were fitted to the following empirical equation:

$$p = A\rho + B\frac{(\rho - \rho_r)^{\delta}}{\delta} \qquad \text{(S3)}$$

The correlation describes the pressure as a function of density at each temperature and composition. The critical exponent δ = 4.82. The parameters A, B and ρ_r are reported in Table S.6. Deviations between the calculated values and experimental compressed-fluid densities are shown in Figure S7.

Table S8: Parameters A, B and ρ_r in equation 1 for compressed liquid densities and the values of the average absolute deviation, Δ_{AAD}, and average absolute relative deviation, Δ_{AARD} for (CO_2 + n-heptane) system.

x_1	0.2053	0.3989	0.6037	0.8001
		T = 283.15 K		
A/[MPa·(kg·m^{-3})$^{-1}$]	-1.0207·10^{-1}	-7.7170·10^{-2}	-4.9340·10^{-2}	-2.4100·10^{-2}
B/[MPa·(kg·m^{-3})$^{-\delta}$]	2.5434·10^{-10}	1.9186·10^{-10}	1.1760·10^{-10}	5.8171·10^{-11}
ρ_r/(kg·m^{-3})	3.7785·10^{2}	3.9471·10^{2}	4.1630·10^{2}	4.5082·10^{2}
Δ_{AAD}/MPa	0.040	0.030	0.081	0.065
Δ_{AARD}	0.12%	0.11%	0.24%	0.23%
		T = 298.15 K		
A/[MPa·(kg·m^{-3})$^{-1}$]	-8.6050·10^{-2}	-6.2840·10^{-2}	-3.6210·10^{-2}	-1.2920·10^{-2}
B/[MPa·(kg·m^{-3})$^{-\delta}$]	2.7086·10^{-10}	2.0124·10^{-10}	1.2445·10^{-10}	5.6148·10^{-11}
ρ_r/(kg·m^{-3})	3.8004·10^{2}	3.9537·10^{2}	4.1649·10^{2}	4.4153·10^{2}
Δ_{AAD}/MPa	0.036	0.024	0.026	0.080
Δ_{AARD}	0.14%	0.10%	0.10%	0.31%
		T = 323.15 K		
A/[MPa·(kg·m^{-3})$^{-1}$]	-6.8370·10^{-2}	-4.6060·10^{-2}	-2.1310·10^{-2}	6.521410^{-4}
B/[MPa·(kg·m^{-3})$^{-\delta}$]	2.5652·10^{-10}	1.9048·10^{-10}	1.1381·10^{-10}	4.9106·10^{-11}
ρ_r/(kg·m^{-3})	3.6797·10^{2}	3.8172·10^{2}	3.9647·10^{2}	4.1063·10^{2}
Δ_{AAD}/MPa	0.035	0.014	0.039	0.21
Δ_{AARD}	0.12%	0.07%	0.18%	1.72%
		T = 348.15 K		
A/[MPa·(kg·m^{-3})$^{-1}$]	-5.2360·10^{-2}	-3.1170·10^{-2}	-7.8800·10^{-3}	1.1890·10^{-2}
B/[MPa·(kg·m^{-3})$^{-\delta}$]	2.4456·10^{-10}	1.8045·10^{-10}	1.0505·10^{-10}	4.0108·10^{-11}
ρ_r/(kg·m^{-3})	3.5644·10^{2}	3.6800·10^{2}	3.7724·10^{2}	3.7214·10^{2}
Δ_{AAD}/MPa	0.042	0.028	0.033	0.081
Δ_{AARD}	0.15%	0.12%	0.15%	0.31%
		T = 373.15 K		
A/[MPa·(kg·m^{-3})$^{-1}$]	-3.8050·10^{-2}	-1.8630·10^{-2}	3.4200·10^{-3}	2.1030·10^{-2}
B/[MPa·(kg·m^{-3})$^{-\delta}$]	2.3284·10^{-10}	1.6500·10^{-10}	9.3788·10^{-11}	3.0960·10^{-11}
ρ_r/(kg·m^{-3})	3.4471·10^{2}	3.5098·10^{2}	3.5456·10^{2}	3.2667·10^{2}
Δ_{AAD}/MPa	0.029	0.024	0.043	0.056
Δ_{AARD}	0.11%	0.10%	0.20%	0.20%
		T = 398.15 K		
A/[MPa·(kg·m^{-3})$^{-1}$]	-2.6370·10^{-2}	-7.1000·10^{-3}	1.0040·10^{-2}	2.9490·10^{-2}
B/[MPa·(kg·m^{-3})$^{-\delta}$]	2.0924·10^{-10}	1.5419·10^{-10}	6.4579·10^{-11}	2.3813·10^{-11}
ρ_r/(kg·m^{-3})	3.2808·10^{2}	3.3571·10^{2}	3.0672·10^{2}	2.8075·10^{2}
Δ_{AAD}/MPa	0.040	0.054	0.032	0.056
Δ_{AARD}	0.16%	0.16%	0.15%	0.16%
		T = 423.15 K		
A/[MPa·(kg·m^{-3})$^{-1}$]	-1.5200·10^{-2}	2.0900·10^{-3}	1.9860·10^{-2}	3.6420·10^{-2}

x_1	0.2053	0.3989	0.6037	0.8001
B/[MPa·(kg·m^{-3})$^{-δ}$]	$1.9517 \cdot 10^{-10}$	$1.3367 \cdot 10^{-10}$	$6.0736 \cdot 10^{-11}$	$1.8017 \cdot 10^{-11}$
ρ_r/(kg·m^{-3})	$3.1442 \cdot 10^{2}$	$3.1366 \cdot 10^{2}$	$2.8853 \cdot 10^{2}$	$2.3169 \cdot 10^{2}$
Δ_{AAD}/MPa	0.030	0.026	0.038	0.063
Δ_{AARD}	0.12%	0.12%	0.13%	0.18%
		T = 448.15 K		
A/[MPa·(kg·m^{-3})$^{-1}$]	$-5.6000 \cdot 10^{-3}$	$1.0340 \cdot 10^{-2}$	$2.7130 \cdot 10^{-2}$	$4.2930 \cdot 10^{-2}$
B/[MPa·(kg·m^{-3})$^{-δ}$]	$1.7790 \cdot 10^{-10}$	$1.1579 \cdot 10^{-10}$	$5.0274 \cdot 10^{-11}$	$1. \cdot 10^{-11}$
ρ_r/(kg·m^{-3})	$2.9863 \cdot 10^{2}$	$2.9138 \cdot 10^{2}$	$2.5762 \cdot 10^{2}$	$1.8472 \cdot 10^{2}$
Δ_{AAD}/MPa	0.025	0.025	0.023	0.059
Δ_{AARD}	0.10%	0.11%	0.07%	0.21%
		T = 473.15 K		
A/[MPa·(kg·m^{-3})$^{-1}$]	$2.4400 \cdot 10^{-3}$	$1.7340 \cdot 10^{-2}$	$3.3140 \cdot 10^{-2}$	$4.9240 \cdot 10^{-2}$
B/[MPa·(kg·m^{-3})$^{-δ}$]	$1.5502 \cdot 10^{-10}$	$9.7141 \cdot 10^{-11}$	$3.9744 \cdot 10^{-11}$	$1.1739 \cdot 10^{-11}$
ρ_r/(kg·m^{-3})	$2.7903 \cdot 10^{2}$	$2.6596 \cdot 10^{2}$	$2.2129 \cdot 10^{2}$	$1.4545 \cdot 10^{2}$
Δ_{AAD}/MPa	0.031	0.022	0.015	0.069
Δ_{AARD}	0.12%	0.08%	0.05%	0.26%

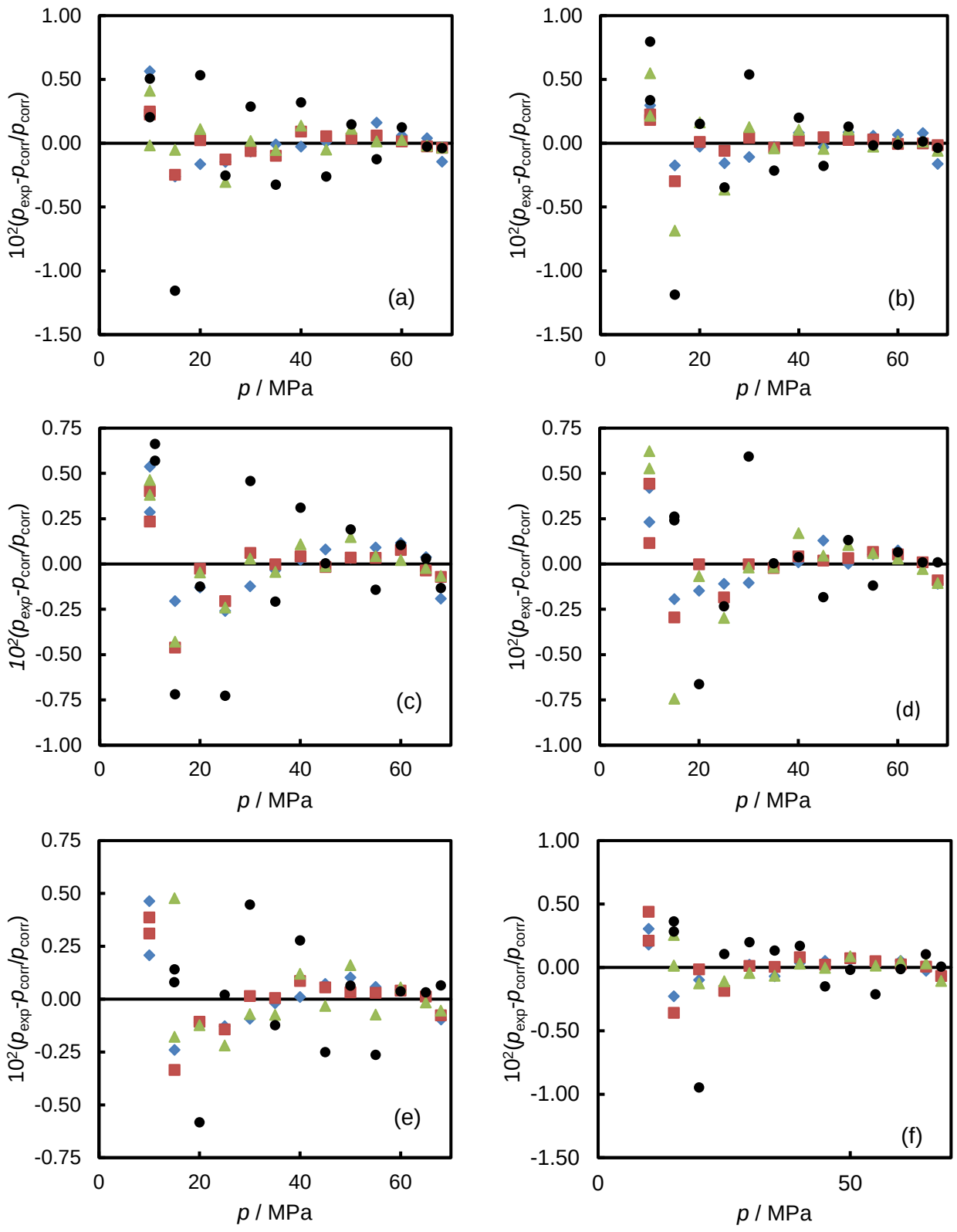

Figure S7: Relative deviations of the experimental pressure from those calculated with equation S3 at (a) T = 298 K, (b) T = 323 K, (c) T = 348 K, (d) T = 373 K, (e) T = 423 K and (f) T = 448 K. Symbols denote different mole fraction of CO_2 in the binary mixture: ▲, 0.2; ■, 0.4; ● , 0.6; ◆, 0.8.

4.2 Saturated phase density

The experimental saturated-phase densities were correlated at each temperature as follows:

$$\left.\begin{aligned}\rho_{\mathrm{L}}-\rho_{\mathrm{V}} &= \sum_{i=1}^{2\text{ or }3} A_i\left(p_{\mathrm{c}}-p\right)^i + C\left(p_{\mathrm{c}}-p\right)^{\beta} \\ \rho_{\mathrm{L}}+\rho_{\mathrm{V}} &= 2\rho_{\mathrm{c}} + \sum_{i=1}^{2\text{ or }3} B_i\left(p_{\mathrm{c}}-p\right)^i + D\left(p_{\mathrm{c}}-p\right)^{\beta}\end{aligned}\right\} \qquad \text{(S4)}$$

where ρ_{L}, ρ_{V} and p are the experimental saturated-liquid densities, saturated-vapour densities, and pressure respectively. The critical exponent β = 0.325. A_i, B_i, C and D are the fitting parameters. p_{c} and ρ_{c} are the critical pressure and density, respectively, and they were also obtained by fitting to the data. To constrain the correlation at p = 0, the (hypothetical) liquid-phase density was set at the values of the density of pure heptane at each temperature and the vapour-phase density was set at zero. Table S9 lists the values of the fitting parameters and the absolute average deviations at each temperature. Deviations of the experimental density from those calculated are also plotted in Figure S8.

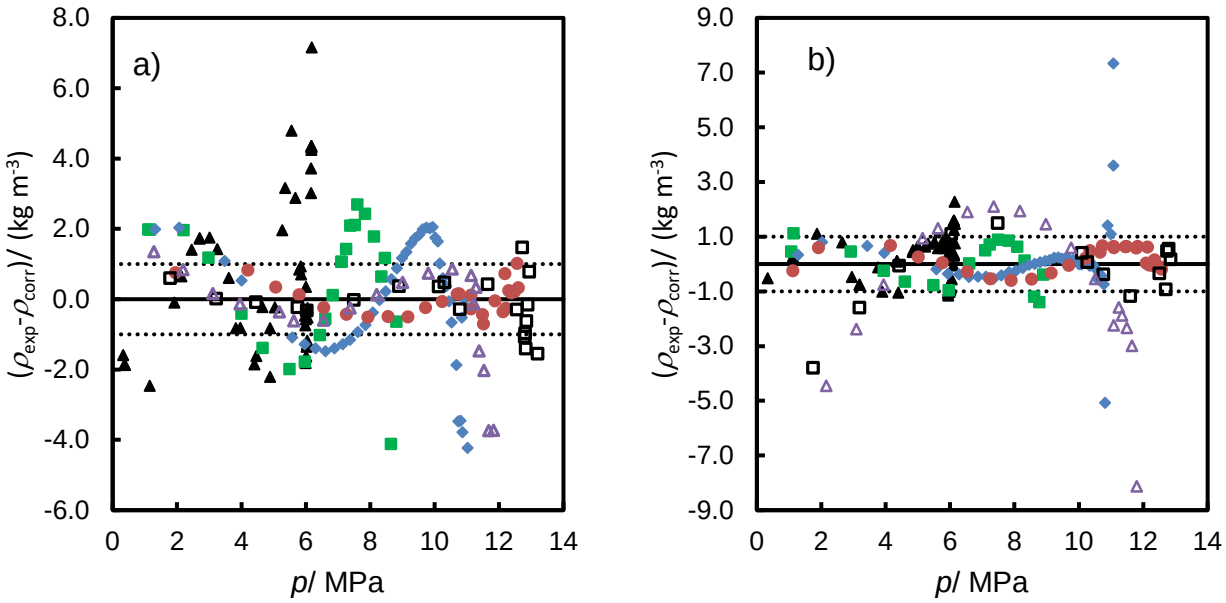

Figure S8. Deviations ($\rho_{exp}-\rho_{corr}$) of experimental saturated phase density of (CO_2 + n-heptane) system from those calculated by equation S4: a) liquid phase and b) vapour phase. Symbols denote different temperatures: ▲, 298 K; ■, 323 K; ◆, 348 K; ●, 373 K; □ 423 K; and △, 448 K. ▪▪▪▪▪▪, ± 1 kg m^{-3}.

Table S9. Parameters A_i, B_i, C and D in equation (S3) for saturated phase densities, where p_c and ρ_c are the critical pressure and critical density. The values of the average absolute deviation, Δ_{AAD}, and average absolute relative deviation, Δ_{AARD} for (CO_2 + n-heptane) system.[a] The subscript L and V denote the liquid and vapour phases.

$\frac{T}{\mathrm{K}}$	$\frac{A_1}{\mathrm{kg\cdot m^{-3}\cdot MPa^{-1}}}$	$\frac{A_2}{\mathrm{kg\cdot m^{-3}\cdot MPa^{-2}}}$	$\frac{A_2}{\mathrm{kg\cdot m^{-3}\cdot MPa^{-3}}}$	$\frac{C}{\mathrm{kg\cdot m^{-3}\cdot MPa^{-\beta}}}$	$\frac{B_1}{\mathrm{kg\cdot m^{-3}\cdot MPa^{-1}}}$	$\frac{B_2}{\mathrm{kg\cdot m^{-3}\cdot MPa^{-2}}}$	$\frac{B_3}{\mathrm{kg\cdot m^{-3}\cdot MPa^{-3}}}$	$\frac{D}{\mathrm{kg\cdot m^{-3}\cdot MPa^{-\beta}}}$
298	-269.88	32.500	-1.7719	841.88	-318.27	40.806	-2.3912	554.322
323	-58.677	1.6263	$3.5440\cdot10^{-2}$	504.05	-72.099	4.706	-0.1.5096	25.698
348	-1.1383	-2.0166	0.11090	340.21	-34.291	1.195	$-2.1210\cdot10^{-2}$	-57.695
373	9.5424	-1.6009	$6.5400\cdot10^{-2}$	269.23	-34.829	1.466	$-4.1250\cdot10^{-2}$	-23.746
423	2.3227	$-6.3300\cdot10^{-3}$	-	229.78	-14.072	$-3.6300\cdot10^{-2}$	-	-29.836
448	3.3504	$2.2890\cdot10^{-2}$	-	215.43	-11.149	-0.21032	-	-18.277

$\frac{T}{\mathrm{K}}$	$\frac{2\rho_c}{\mathrm{kg\cdot m^{-3}}}$	$\frac{p_c}{\mathrm{MPa}}$	$\frac{\Delta_{AADL}}{\mathrm{kg\cdot m^{-3}}}$	Δ_{AARDL}	$\frac{\Delta_{AADV}}{\mathrm{kg\cdot m^{-3}}}$	Δ_{AARDV}
298	662.91	6.52	1.9	0.2	0.8	0.6
323	981.46	8.93	1.5	0.2	1.1	0.8
348	1024.83	11.15	1.4	0.2	0.7	0.3
373	955.49	12.67	0.4	0.1	0.4	0.3
423	815.83	13.00	0.5	0.7	0.9	1.3
448	731.33	11.99	1.0	0.4	2.2	1.8
All			1.1	0.5	1.0	0.8

[a] Data close to critical points were not used in the calculation of Δ_{AAD} and Δ_{AARD}

5. Bubble pressures and bubble compositions obtained from density data

Table S10. Bubble pressures, p_b for the (CO_2 + n-heptane) system at temperatures T and CO_2 mole fractions x: (a) determined from the intersection between the compressed liquid densities and the saturated phase densities; and (b) determined experimentally from the direct observation of VLE. Δp, denote the difference between bubble pressures calculated from the density data and the values obtained from the VLE measurements.

T/K	x	[a]p_b/MPa	[b]p_b/MPa	Δp/MPa
298	0.2053	1.52	1.55	-0.034
	0.3989	3.06	3.08	-0.016
	0.6037	4.28	4.37	-0.09
	0.8001	5.26	5.23	0.032
323	0.2053	1.97	2.16	-0.19
	0.3989	4.06	4.19	-0.13
	0.6037	6.37	6.31	0.06
	0.8001	7.73	7.83	-0.10
348	0.2053	2.62		
	0.3989	5.19		
	0.6037	8.50		
	0.8001	10.49		
373	0.2053	3.35	3.38	-0.03
	0.3989	6.68	6.48	0.20
	0.6037	9.76	9.88	-0.12
	0.8001	12.55	12.45	0.10
423	0.2053	4.41	4.38	0.03
	0.3989	8.16	8.41	-0.25
	0.6037	12.34	12.22	0.12
	0.8001	13.00	12.39	0.6
448	0.2053	4.61		
	0.3989	8.63		
	0.6037	11.78		

6. Modelling

6.1 Peng-Robinson and SAFT-γ Mie

In this work, the predictive capabilities of the Peng Robinson [5] and SAFT-γ Mie models were tested. Table S11 to S13 give the parameter values used. Figure S9 shows deviation plots for compressed-fluid density data from the predictions of SAFT-γ Mie and PPR-78 model along 9 isotherms.

Table S11. Binary interaction parameters for the PPR EOS at different temperatures [5]

T/K	k_{12}
283.15	0.1090
298.15	0.1092
323.15	0.1102
348.15	0.1120
373.15	0.1136
423.15	0.1188
448.15	0.1220
473.15	0.1253

Table S12. Parameters for the groups used in the SAFT-γ Mie equation [6, 7]

	S_k	(ε/k_B)/K	$\sigma/(10^{-10}\text{m})$	λ_r	λ_a
CH_3	0.5725	256.77	4.077	15.050	6.00
CH_2	0.2293	473.39	4.880	19.871	6.00
CO_2	0.8470	207.89	3.050	26.408	5.06

Table S13. Cross interaction energies (ε_{12}/k_B)/K for the groups used in the SAFT-γ Mie equation [6, 7]

	CH_3	CH_2	CO_2
CH_3	256.77		
CH_2	350.77	473.39	
CO_2	205.70	276.45	207.89

6.2 GERG-2008

Calculations were also performed with the GERG-2008 model [8] as implemented in the REFPROP v9.1 software [9]. Figure S10 compared the experimental VLE data, including literature data, with the predictions of GERG-2008, while figure S11 and S12 compare the present saturated-phase and compressed-fluid density data with the same model.

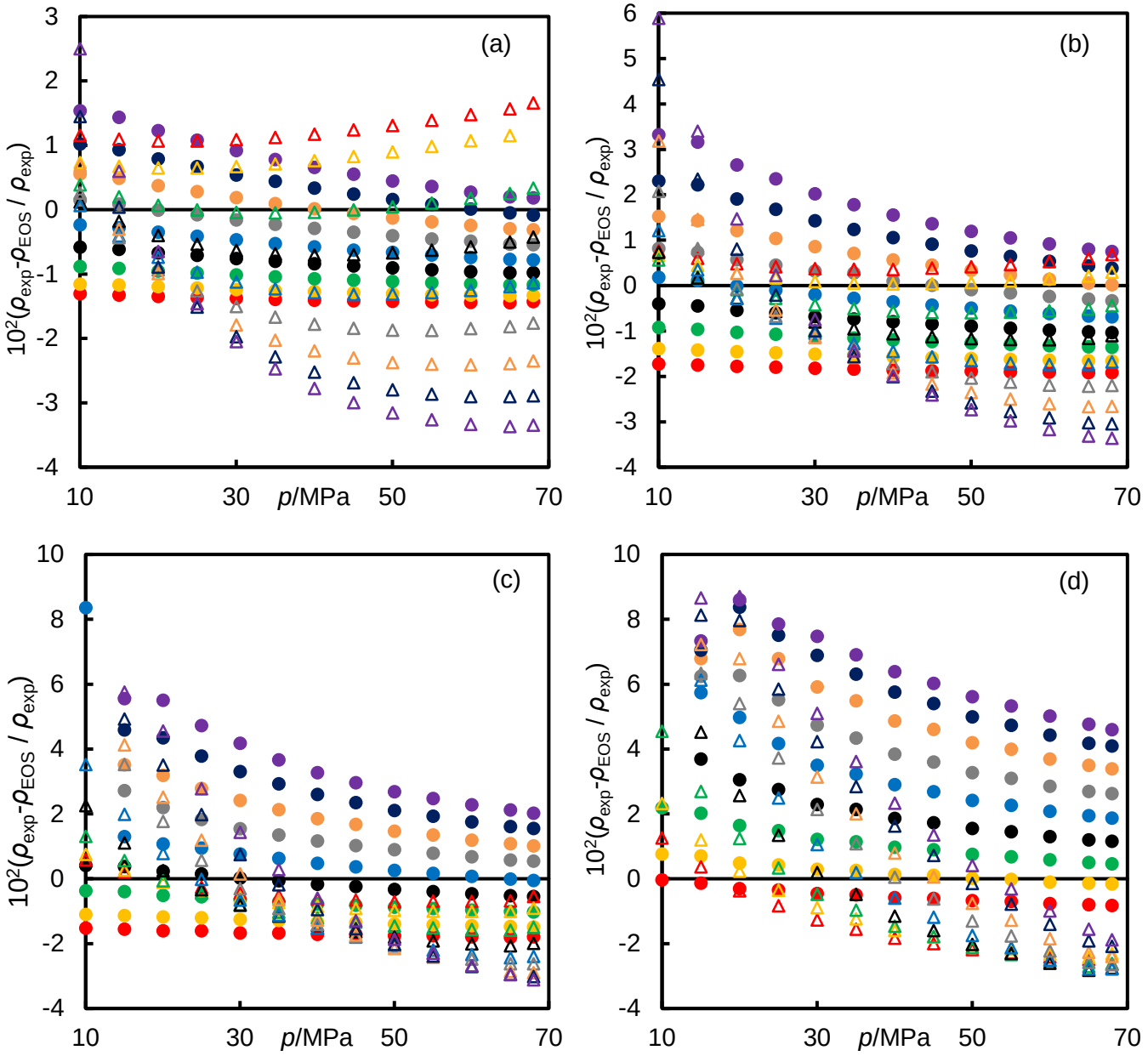

Figure S9: Deviation plots of compressed liquid density experimental data compared with predictions from SAFT-γ Mie and PPR78 EoS along 9 isotherms (●, 283 K, ●, 298 K, ●, 323 K, ●,348 K, ●, 373 K, ●, 398 K, ●, 423 K, ●, 448 K, ●, 473 K) at four mole fractions *x* of CO_2: (a) *x* = 0.2; (b) *x* = 0.4; (c) *x* = 0.6; and (d) *x* = 0.8. Filled symbols represent SAFT-γ Mie and unfilled symbols for PPR78 EoS respectively.

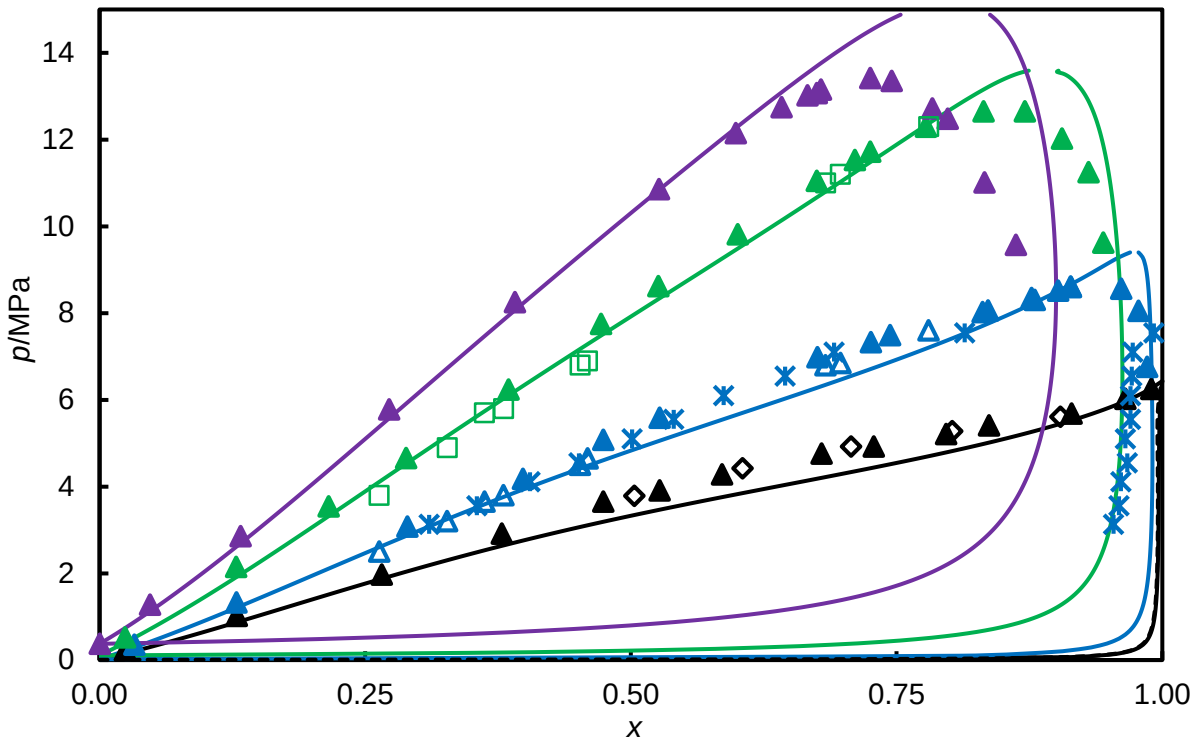

Figure S10. Bubble and dew-point pressures p for (CO_2 + n-heptane) as a function of the mole fraction x of CO_2 at temperatures of 298.15 K (black), 323.15 K (blue), 373.15 K (green), and 423.15.15 K (purple). Filled symbols are from this work and open symbols from the literature: ◇, Lay [10]; ∗, He et al. [11]; △, Mutelet et al. [12]; □, Mutelet et al. [12]. Solid lines are calculated from GERG-2008 [8].

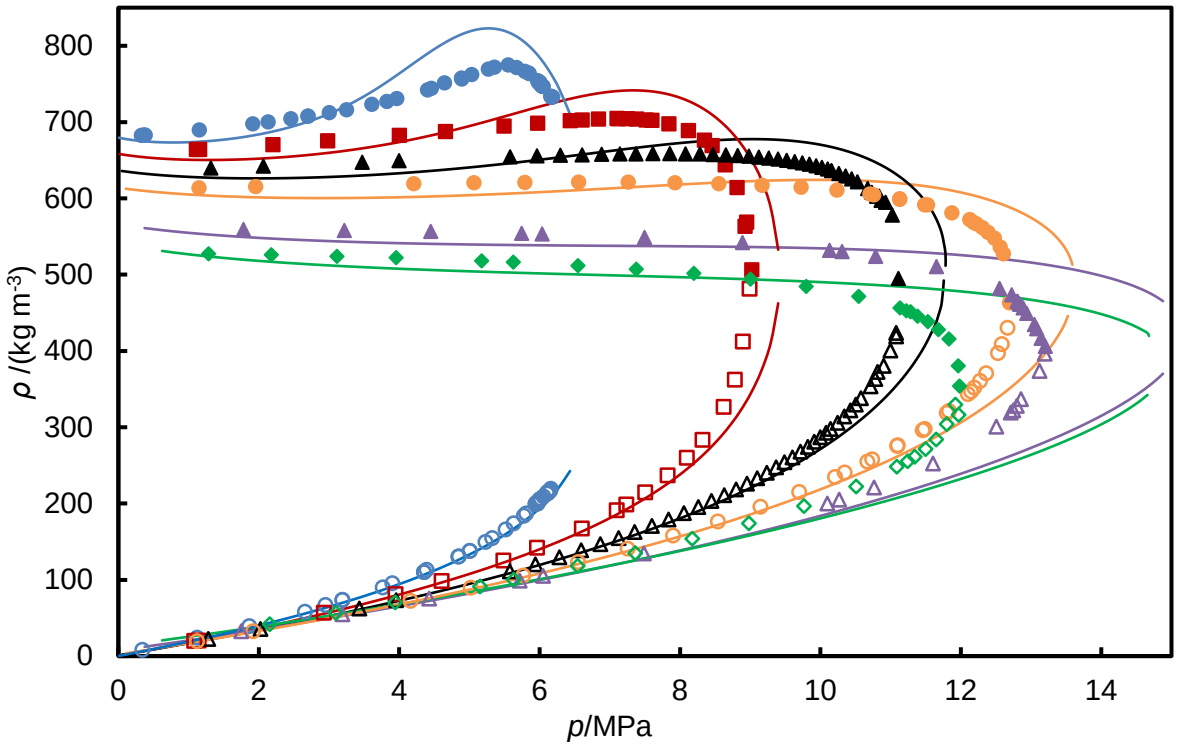

Figure S11. Comparisons between experimental saturated phase densities ρ of CO_2 + n-heptane and predictions from GERG-2008 (solid lines) as a function of pressure p at temperatures of 298 K (blue circles), 323 K (red squares), 348 K (black triangles), 373 K (orange circles), 423 K (purple triangles), and 448 K (green diamonds).

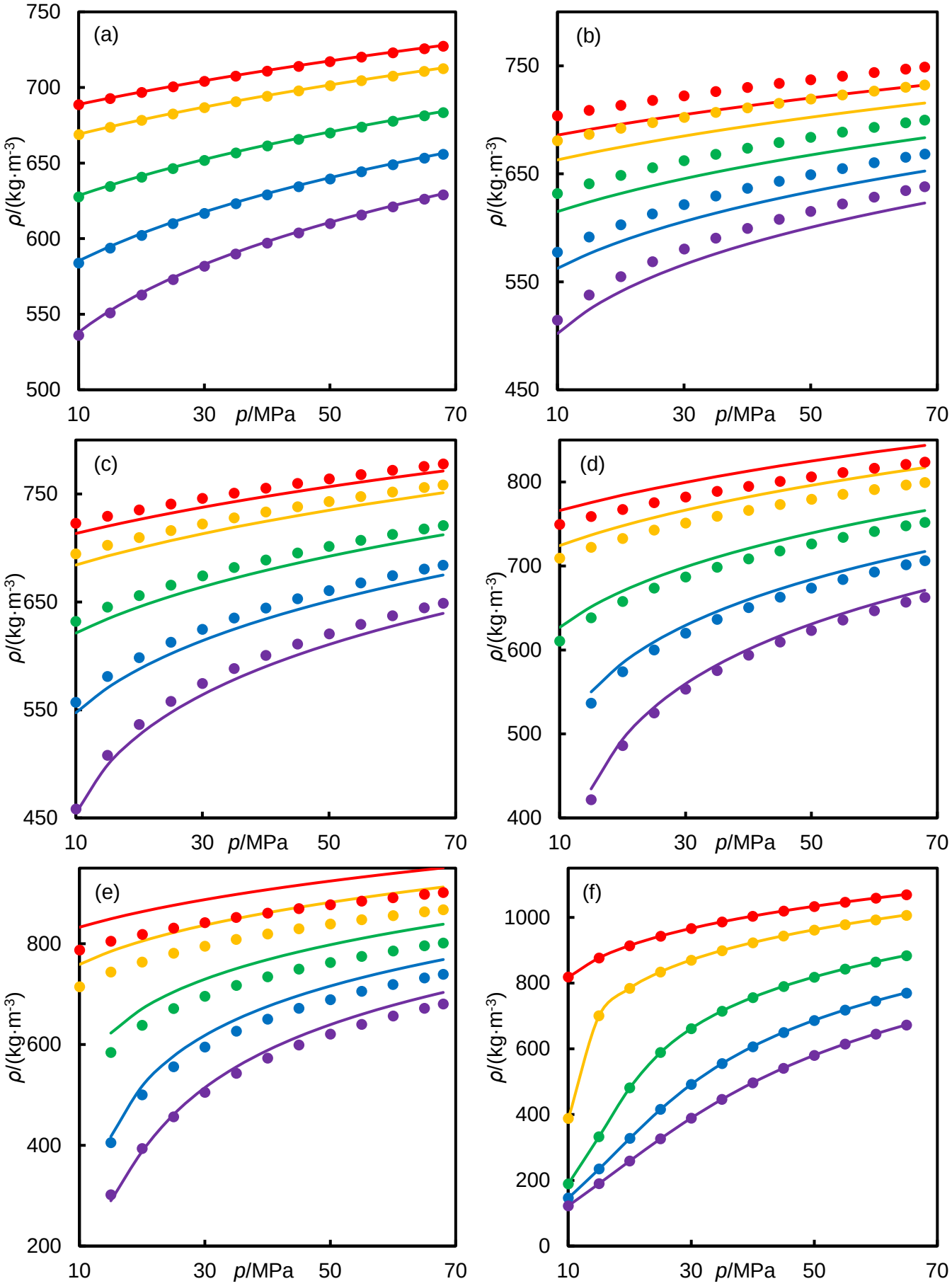

Figure S12. Comparisons between experimental densities ρ of (1 - x) C_7H_{16} + x CO_2 (●) and predictions from GERG-2008 (solid lines) as a function of pressure p at temperatures of 298.15 K (red), 323.15 K (yellow), 373.15 K (green), 423.15 K (blue) and 473.15 K (purple): (a) x = 0.0; (b) x = 0.2; (c) x = 0.4; (d) x = 0.6; (e) x = 0.8; (f) x = 1.0.

References

[1] Span R, Wagner W. Equations of state for technical applications. II. Results for nonpolar fluids. Int J Thermophys. 2003;24:41-109.

[2] Span R, Wagner W. A new equation of state for carbon dioxide covering the fluid region from the triple-point temperature to 1100 K at pressures up to 800 MPa. J Phys Chem Ref Data. 1996;25:1509-96.

[3] Medina-Bermudez M, Saavedra-Molina LA, Escamilla-Tiburcio W, Galicia-Luna LA, Elizalde-Solis O. (p, rho, T) Behavior for the Binary Mixtures Carbon Dioxide plus Heptane and Carbon Dioxide plus Tridecane. J Chem Eng Data. 2013;58:1255-64.

[4] Rabe D. Experimental determination of dynamic viscosity and density of binary liquid mixtures of n-heptane with CO_2, CH_4, C_2H_6, C_3H_8 and of toluene with CH_4 and C_3H_8: TU Berlin; 1981.

[5] Jaubert JN, Mutelet F. VLE predictions with the Peng-Robinson equation of state and temperature dependent k(ij) calculated through a group contribution method. Fluid Phase Equilib. 2004;224:285-304.

[6] Papaioannou V, Lafitte T, Avendano C, Adjiman CS, Jackson G, Mueller EA, et al. Group contribution methodology based on the statistical associating fluid theory for heteronuclear molecules formed from Mie segments. J Chem Phys. 2014;140.

[7] Papaioannou V, Calado F, Lafitte T, Dufal S, Sadeqzadeh M, Jackson G, et al. Application of the SAFT-γ Mie group contribution equation of state to fluids of relevance to the oil and gas industry. Fluid Phase Equilib. 2016;416:104-19.

[8] Kunz O, Wagner W. The GERG-2008 wide-range equation of state for natural gases and other mixtures: an expansion of GERG-2004. J Chem Eng Data. 2012;57:3032–91.

[9] Lemmon EW, Huber ML, McLinden MO. NIST standard reference database 23: Reference fluid thermodynamic and transport properties - REFPROP, Version 9.1. Gaithersburg: National Institute of Standards and Technology 2013.

[10] Lay EN. Measurement and Correlation of Bubble Point Pressure in (CO_2 + C_6H_6), (CO_2 + $CH_3C_6H_5$), (CO_2 + C_6H_{14}), and (CO_2 + C_7H_{16}) at Temperatures from (293.15 to 313.15) K. J Chem Eng Data. 2010;55:223-7.

[11] He Y, Lou Z, Ma S, Hu Y. Measuring phase equilibria of carbon dioxide + n-heptane system by stoichiometry. Huadong Ligong Daxue Xuebao. 1994;20:79-84.

[12] Mutelet F, Vitu S, Privat R, Jaubert JN. Solubility of CO_2 in branched alkanes in order to extend the PPR78 model (predictive 1978, Peng-Robinson EOS with temperature-dependent k_{ij} calculated through a group contribution method) to such systems. Fluid Phase Equilib. 2005;238:157-68.